

Optoelectronic Characterization of Thin-Film Solar Cells by Electroreflectance and Luminescence Spectroscopy

Zur Erlangung des akademischen Grades eines
DOKTORS DER NATURWISSENSCHAFTEN
von der Fakultät für Physik
des Karlsruher Instituts für Technologie (KIT)

genehmigte

DISSERTATION

von

Dipl.-Phys. Christoph Daniel Krämmer
aus Karlsruhe

Tag der mündlichen Prüfung : 26.06.2015
Referent : Prof. Dr. H. Kalt
Korreferent : Priv.-Doz. Dr. M. Hetterich

Prüfungskommission:

Prof. Dr. H. Kalt
Priv.-Doz. Dr. M. Hetterich
Prof. Dr. A. Shnirman
Priv.-Doz. Dr. S. Gieseke
Prof. Dr. T. Müller



Karlsruhe Institute of Technology (KIT)
Institute of Applied Physics
Wolfgang-Gaede-Straße 1
76131 Karlsruhe
Germany
AG Kalt: <http://www.aph.kit.edu/kalt>

Christoph Daniel Krämmmer
christoph.kraemmer@kit.edu christoph.kraemmer@gmail.com

This work has been supported financially by the Karlsruhe School of Optics and Photonics as well as the Carl-Zeiss-Foundation.



<http://www.ksop.de>



<http://www.carl-zeiss-stiftung.de>

Contents

| | | |
|----------|---|-----------|
| 1 | Introduction | 1 |
| 2 | Chalcogenide Absorber Materials for Thin-Film Photovoltaics | 5 |
| 2.1 | Properties of Chalcogenide Absorber Layers | 5 |
| 2.1.1 | Crystal Structure | 7 |
| 2.1.2 | Band Structure and Optical Properties | 9 |
| 2.1.3 | Important Defects and Secondary Phases | 13 |
| 2.2 | Chalcogenide Absorber Thin-Film Solar Cells | 17 |
| 2.2.1 | Thin-Film Solar Cell Structure | 17 |
| 2.2.2 | Fabrication of Thin-Film Absorber Layers | 19 |
| 2.3 | Summary and Relevance for this Work | 21 |
| 3 | Experimental Techniques | 23 |
| 3.1 | Modulation Spectroscopy | 24 |
| 3.1.1 | Optical Properties of Semiconductors | 24 |
| 3.1.2 | Main Idea of Modulation Spectroscopy | 25 |
| 3.1.3 | Physical Mechanism and Lineshape Considerations | 26 |
| 3.1.4 | Evaluation of Electroreflectance Spectra | 32 |
| 3.1.5 | Electroreflectance Setup | 34 |
| 3.2 | Photoluminescence Spectroscopy | 37 |
| 3.2.1 | Application of Photoluminescence Spectroscopy in this Work | 37 |
| 3.2.2 | Photoluminescence Spectroscopy Setup | 37 |
| 3.3 | Photoluminescence Excitation Spectroscopy | 39 |
| 3.3.1 | Physical Mechanism of Photoluminescence Excitation Spectroscopy | 39 |
| 3.3.2 | Photoluminescence Excitation Spectroscopy Setup | 40 |
| 3.4 | Summary | 41 |
| 4 | Electroreflectance on Thin-Film Solar Cells | 43 |
| 4.1 | Deviations from Ideal Measurement Conditions | 44 |
| 4.2 | One-Dimensional Simulation of Electroreflectance Spectra | 45 |

| | | |
|----------|---|-----------|
| 4.3 | Influence of the Electric Field on Electroreflectance Spectra | 47 |
| 4.3.1 | The Electric Field in the Space-Charge Region | 48 |
| 4.3.2 | Electroreflectance with a Strong & Spatially Inhomogeneous Perturbation | 51 |
| 4.4 | Interference Effects in Electroreflectance Spectra | 53 |
| 4.4.1 | Influence of the ZnO Window Layer | 54 |
| 4.4.2 | Influence of the Mo Back Contact | 55 |
| 4.5 | Experiment and Simulation: Determination of the Band Gap of Cu(In,Ga)Se ₂ | 57 |
| 4.6 | Electroreflectance on Thin-Film Solar Cells in Literature | 59 |
| 4.7 | Summary | 61 |
| 5 | Electromodulated Diffuse Reflectance | 63 |
| 5.1 | Layer Morphology of Thin-Film Solar Cells | 64 |
| 5.2 | Simulation of Modulated Diffuse Reflectance from a Rough Surface | 65 |
| 5.3 | Electroreflectance Measurements in Diffuse Reflection | 67 |
| 5.4 | Gallium-Content-Dependent Band Gap of CIGS | 70 |
| 5.5 | Inhomogeneous Broadening in Electroreflectance | 72 |
| 5.5.1 | Inhomogeneous Broadening in the Low-Field Limit | 73 |
| 5.5.2 | Experimental Evidence of Inhomogeneous Broadening | 76 |
| 5.6 | Summary | 77 |
| 6 | Optical Transitions in Cu₂ZnSn(S,Se)₄ | 79 |
| 6.1 | Comparison of Different Methods of Band Gap Determination in Thin-Film Solar Cells | 79 |
| 6.2 | Review of Radiative Recombination Mechanisms in Cu ₂ ZnSn(S,Se) ₄ | 82 |
| 6.2.1 | Defect-Related Recombination | 82 |
| 6.2.2 | Band-Related Recombination | 85 |
| 6.3 | Anomalous Thermal Dependence of the Band Gap of Cu ₂ ZnSn(S,Se) ₄ | 86 |
| 6.4 | Identification of Contributions to Radiative Recombination | 90 |
| 6.4.1 | Excitation Power-Dependent Photoluminescence | 90 |
| 6.4.2 | Comparison of Photoluminescence to Photoluminescence Excitation Spectra | 94 |
| 6.4.3 | Temperature-Dependent Photoluminescence | 96 |
| 6.5 | Summary | 97 |
| 7 | Assessment of the Role of Cu–Zn Disorder in Cu₂ZnSn(S,Se)₄ | 99 |
| 7.1 | Efficiency Limitations of Cu ₂ ZnSn(S,Se) ₄ Solar Cells | 100 |
| 7.2 | Controlling Cu–Zn Disorder in the Cu ₂ ZnSn(S,Se) ₄ Unit Cell | 101 |
| 7.2.1 | Cu–Zn Disorder Kinetics – The Vineyard Model | 102 |
| 7.2.2 | The Order–Disorder Transition in Literature | 106 |

| | | |
|----------|---|------------|
| 7.2.3 | Post-Annealing of Solar Cells | 107 |
| 7.3 | Order–Disorder Related Band Gap Changes | 108 |
| 7.3.1 | Detection of Reversible Band Gap Changes Using Electroreflectance | 108 |
| 7.3.2 | Determination of the Critical Temperature of the Order–Disorder Transition | 110 |
| 7.3.3 | Temporal Evolution of the Band Gap During Post-Annealing Experiments | 112 |
| 7.4 | Impact of Cu–Zn Disorder on Solar Cell Performance | 114 |
| 7.5 | Assessment of the Order–Disorder Transition in $\text{Cu}_2\text{ZnSn}(\text{S},\text{Se})_4$ | 116 |
| 7.6 | Summary | 118 |
| 8 | Conclusions and Outlook | 119 |
| A | Optical and Electronic Components of the Setups | 123 |
| B | Correction of PL and PLE Spectra | 127 |
| B.1 | Correction of Photoluminescence Spectra | 127 |
| B.2 | Correction of Photoluminescence Excitation Spectra | 127 |
| C | Samples Investigated In This Work | 129 |
| | List of Publications | 133 |
| | References | 139 |
| | Closing Words | 157 |

Genius is one percent inspiration and
ninety-nine percent perspiration

Thomas Edison

Chapter 1

Introduction

In March 2011, mankind witnessed the core meltdown of the nuclear power plant in Fukushima. In the course of this event thousands of people lost their homes permanently due to radioactive contamination [1]. Once again after the incident of Chernobyl in 1986 this demonstrated that nuclear energy is not the solution for a sustainable electricity production to satisfy the increasing demand in future years [2] – especially if the financial profit of an operating company appears in the equations. A long-lasting role of fossil fuels in the energy supply for humans is ruled out due to their contribution to global warming and their limited availability in the future.

After the events of Fukushima, the German government increased the efforts to promote the "Energiewende" – a systematic expansion of renewable energies to become independent of nuclear power and, in the long run, of fossil fuels. A core element of renewable energies is photovoltaics (PV) – the conversion of solar energy into electric energy. Nowadays, silicon-based solar cells hold the largest market share of all PV technologies [3]. One of the reasons for this is the long technical experience with the material but also its abundance in earth's crust. Innovative concepts such as zero-energy buildings are an interesting and sustainable concept but rely on affordable PV technology [4].

However, the use of an indirect band gap semiconductor such as silicon brings along several problems, the most important technical one being the need of a thick absorber layer and a high material purity in consequence [5]. These physical reasons together with the prospectives of cheap and large-scale fabrication methods, such as roll-to-roll processes, lead to the field of thin-film solar cells [6]. The most prominent representative of this category of solar cells is $\text{Cu}(\text{In,Ga})\text{Se}_2$ (CIGS). The use of this direct semiconductor allows for a layer thickness of only a few micrometer while achieving a record power conversion efficiency of currently 21.7% [7]. In contrast

to silicon, not all constituting elements of $\text{Cu}(\text{In,Ga})\text{Se}_2$ are earth-abundant and especially indium experienced a strong increase in demand in form of indium-tin oxide in electronics industry in recent years [8,9]. A possible price escalation of the raw materials would have catastrophic consequences for this thin-film technology [10].

These considerations lead to the development of a new absorber material system for thin-film photovoltaics: $\text{Cu}_2\text{ZnSn}(\text{S,Se})_4$ (CZTSSe) or kesterite¹. This material is structurally related to CIGS but only comprises earth-abundant elements as constituents. However, despite the similarities to CIGS fabrication of CZTSSe thin films and solar cells turned out to be very challenging [11]. With only 12.6%, the record power conversion efficiency of kesterite solar cells remains far behind that of CIGS solar cells so far [12]. One of the reasons for that is an insufficient knowledge of basic physical properties of CZTSSe. The first parameter which characterizes a semiconductor material as suitable for PV applications is the band gap [13]. Especially this quantity is subject to a large scatter depending on which publication is taken into account [14]. Furthermore, fundamental studies of recombination processes, which play an important role in the device performance of solar cells, rely on a precise knowledge of the band gap. This underlines the necessity of a detailed optical characterization of the CZTSSe material system and in particular, the band gap.

Modulation spectroscopy techniques such as electromodulated reflectance – or short electroreflectance – have been used for decades and are some of the most reliable and precise tools to determine critical points in the band structure of semiconductors [15]. This measurement principle relies on the modulation of the refractive index of a material which in turn causes a change in the reflectivity or transmittivity of the sample. Furthermore, features due to critical points in the band structure of the semiconductor are pronounced. One possibility to induce the modulation of the dielectric function is the application of an external periodic electric field. With the fundamental band gap being one particularly interesting critical point, modulation spectroscopy is an ideal characterization technique for thin-film solar cell absorber materials such as CZTSSe or CIGS. However, a thin-film solar cell represents a special kind of sample for modulation spectroscopy measurements which exhibits several peculiarities. First, a strong built-in electric field in a solar cell deviates from the typically assumed physical situation in the derivation of standard evaluation methods [15] for modulated reflectance spectra. Furthermore, both the refractive index contrast between of the individual functional layers of a thin-film solar cell as well as their thickness cause thin-film interferences which strongly distort measured lineshapes compared to theoretical expectations.

¹The name "kesterite" actually refers to the crystal structure of the material

The aim of this work was to overcome the above-mentioned challenges for electroreflectance to establish this powerful technique in the characterization of thin-film solar cells. Therefore, both the measurement itself and the analysis were improved in the course of this work and the broad applicability to CIGS and CZTSSe solar cells was ensured. Furthermore, electroreflectance was used to investigate the radiative recombination in CZTSSe and to identify individual contributions to luminescence spectra. To support electroreflectance, photoluminescence (PL) and PL excitation (PLE) measurements were performed additionally. Finally, band gap shifts induced by Cu-Zn cation reordering processes in CZTSSe could be correlated to the resulting band gap of the material. The kinetics of these processes were studied and the results lead to an increase in device efficiency.

Structure of This Work

This thesis is structured in 8 chapters. After this introduction the two investigated thin-film absorber material systems, CIGS and CZTSSe are presented in chapter 2. The focus lies on the crystal structures, band structures and on the most important intrinsic defects in the two materials. Furthermore, the principle structure of a thin-film solar cell is introduced and a short overview on different solar cell concepts is given. For completeness, issues which are related to the fabrication of CZTSSe are discussed briefly.

A central part of this work was the application of modulation spectroscopy to thin-film solar cells. Chapter 3 gives an overview on this measurement technique and presents both the underlying physical mechanism and the experimental setup which was used in this work. Further optical measurement techniques such as photoluminescence and photoluminescence excitation spectroscopy were applied to CZTSSe solar cells as well which is why a brief introduction to these techniques will be given.

As it was already mentioned, thin-film solar cells deviate from samples which are typically investigated by means of modulation spectroscopy. Chapter 4 discusses the peculiarities of this kind of sample with respect to the derivation of standard evaluation techniques which are typically used. For this purpose, both optical and electrical one-dimensional simulations are used to investigate the working principle of electroreflectance in thin-film solar cells. In the course of this chapter the deviations from ideal measurement conditions for electroreflectance will be discussed and the limitations of this technique will be presented. As it turned out, the built-in electric field and thin-film interferences play a major role in the measured electroreflectance signal of a thin-film solar cell and need to be considered if no further precautions are taken in the experiment.

Chapter 5 presents a method to reduce the influence of thin-film interferences on a measured electroreflectance signal significantly. The detection of diffusely reflected light instead of specularly reflected light reduces thin-film interferences not only in the reflectance signal but also in the modulated reflectance signal and yields a measurement signal which can be evaluated precisely. This is shown experimentally and the findings are supported by two-dimensional optical simulations.

After the applicability of electroreflectance to thin-film solar cells is ensured the method is used to identify individual contributions to photoluminescence spectra of CZTSSe solar cells in chapter 6. In addition, photoluminescence excitation spectra are also evaluated and allow for a distinction of defect-related and band-related contributions to luminescence spectra of CZTSSe.

In chapter 7, reversible band gap shifts due to thermally-induced reordering of Cu and Zn atoms in the CZTSSe unit cell are detected using electroreflectance. The kinetics of these phenomena is compared to the predictions of a stochastic model. The experiments were performed on finished CZTSSe solar cells and hence it is possible to give an assessment of the impact of these reordering processes on device performance.

The final chapter summarizes the main results of this work and gives an outlook into future experiments and questions.

Chapter 2

Chalcogenide Absorber Materials for Thin-Film Photovoltaics

The aim of this chapter is to give basic insights into the properties of the two thin-film absorber materials $\text{Cu}(\text{In,Ga})\text{Se}_2$ and $\text{Cu}_2\text{ZnSn}(\text{S,Se})_4$ investigated in this work. Since the majority of the experiments were performed on $\text{Cu}_2\text{ZnSn}(\text{S,Se})_4$ solar cells this material system will be given more attention whereas $\text{Cu}(\text{In,Ga})\text{Se}_2$ will often serve as comparison. Furthermore, the reader will be given a general overview on thin-film solar cell structures and their realization.

For $\text{Cu}_2\text{ZnSn}(\text{S,Se})_4$ absorber layers the fabrication turned out to be more challenging than for $\text{Cu}(\text{In,Ga})\text{Se}_2$ which is why fabrication-related issues will be discussed in more detail.

2.1 Properties of Chalcogenide Absorber Layers

In 1961, Shockley and Queisser published their paper in which they investigated the connection between the absorber band gap E_g of a single p-n junction solar cell and the maximum achievable power conversion efficiency η [13]. Assuming standard AM1.5 irradiation, efficiencies of more than 30 % can be achieved for an absorber band gap interval of 1.0–1.5 eV. It should be noted that within the considerations of Shockley and Queisser detrimental effects such as non-radiative carrier recombination and insufficient carrier collection are not taken into account. The model assumes that solar irradiation with a photon energy below the band gap is not absorbed and carriers generated by photons with a photon energy above the band gap thermalize to the conduction band edge which represents an effective carrier energy loss.

Within the Shockley–Queisser limit silicon exhibits an ideal optical band gap of $E_g = 1.1$ eV but the indirect nature of this transition in momentum space yields a low absorption coefficient [16] compared to direct semiconductors such as, e.g., GaAs [17]. Therefore, it is necessary to use a large absorber thickness in the order of hundreds of micrometers to achieve sufficient optical absorption. In turn, this requires a high material purity to obtain a large diffusion length of the generated carriers for efficient separation and extraction. These are the fundamental disadvantages of silicon from a physical point of view which have led to the development of new solar cell concepts.

The main idea of thin-film photovoltaics is the use of a direct semiconductor as an absorber layer which exhibits a large absorption coefficient. This allows for a thinner absorber loosening the requirements for diffusion length and carrier lifetime. In consequence, the raw material input is lowered and hence production costs as well. It should be noted that this is a very simplified picture and the real situation comprises many further aspects, most of them being of economic nature and thus not subject to this thesis.

The use of III–V semiconductors with a direct band gap such as GaAs and the related $\text{Al}_{1-x}\text{Ga}_x\text{As}$ to build thin-film solar cells with a noticeable efficiency has been known since the 1970s [18]. Up to now, the best solar cells in the world are based on III–V semiconductors and achieve power conversion efficiencies of up to 46% [19]. However, these multi-junction devices are based on epitaxial III–V semiconductor layers and a commercial upscaling of this technology cannot be achieved at a competitive module price.

II–VI semiconductors with a tetrahedral coordination of atoms such as ZnSe or CdS also exhibit a direct band gap which makes them – in principle – suitable candidates for solar cell absorbers. However, the band gap of most of these semiconductors is too large to achieve a single-junction solar cell efficiency comparable to silicon within the Shockley–Queisser limit. A possible exception to this circumstance is the chalcogenide CdTe with a band gap of $E_g = 1.49$ eV [20].

It has to be mentioned that CdTe solar cells have made tremendous progress in recent years and conversion efficiencies of 21% could be achieved by First Solar [21]. The relatively mature technology is probably the one which is closest to the proclaimed "1\$ per Watt" goal which is necessary for thin-film technologies in order to become competitive to conventional silicon photovoltaics [22]. According to recent investigations the toxicity of CdTe is lower than the toxicity of elemental Cd and other concerns, e.g., Cd emission in fires, could be eliminated [23,24]. This progress in CdTe photovoltaics has to be mentioned. However, since CdTe is not the subject of this work it will not be considered any further. The same holds for other pho-

photovoltaic technologies such as dye-sensitized solar cells [25], organic solar cells [26], and organic–anorganic hybrid perovskite solar cells [27].

The chalcogenide compound $\text{Cu}(\text{In,Ga})\text{Se}_2$ is structurally related to the zincblende II–VI semiconductors and also exhibits a direct band gap and therefore a high absorption coefficient [28]. Furthermore, the band gap is tunable by varying the ratio of gallium and indium within the absorber layer. Elaborate fabrication techniques and continuous efforts have led to a current world record power conversion efficiency of 21.7% for $\text{Cu}(\text{In,Ga})\text{Se}_2$ solar cells [7].

A possible price escalation of the raw elements indium and tellurium in $\text{Cu}(\text{In,Ga})\text{Se}_2$ and CdTe solar cells, respectively, could have a severe impact on the development of these two thin-film technologies [10]. In anticipation of such a scenario kesterite $\text{Cu}_2\text{ZnSn}(\text{S,Se})_4$ solar cells have been developed. The main advantages of this material system are the abundance of the constituting elements and the similar physical properties to $\text{Cu}(\text{In,Ga})\text{Se}_2$. Since the scope of this work are solar cells based on $\text{Cu}(\text{In,Ga})\text{Se}_2$ and $\text{Cu}_2\text{ZnSn}(\text{S,Se})_4$, a general overview of the main properties of these two materials will be given in the following.

2.1.1 Crystal Structure

Figure 2.1 shows the evolution of crystal structures¹ for tetrahedrally coordinated semiconductors starting from a II–VI zincblende (sphalerite) semiconductor such as ZnSe (Fig. 2.1(a)). $\text{Cu}(\text{In,Ga})\text{Se}_2$ (CIGS) crystallizes in the chalcopyrite structure (Fig. 2.1(b), space group $I\bar{4}2d$ [30]) like its phase prototype CuFeS_2 . This crystal structure can be obtained if the group-II atoms are replaced alternately by group-I and III atoms. This requires a unit cell which is essentially a superstructure of two sphalerite unit cells and yields a I–III–VI₂ semiconductor. This substitution is sometimes also referred to as Goodman’s substitution [31]. Still, the tetrahedral coordination of atoms is maintained in this transition.

In the case of CIGS, the group-III element can be either indium or gallium. The important influence of Cu on the band structure of CIGS as well as the role of cation or anion exchange will be discussed in subsection 2.1.2. The lattice constants of the parent compounds CuInSe_2 and CuGaSe_2 are summarized in Tab. 2.1. The tetragonal unit cell of pure CuInSe_2 is stretched along the **c**-axis and – for increasing gallium contents – undergoes a transition to a compressed unit cell in the case of CuGaSe_2 . Following Goodman’s substitution once again, the kesterite structure (Fig. 2.1(c), space group $I\bar{4}$) is obtained if one replaces the group-III atoms in the

¹All crystal images in this work were created using *Vesta 3* [29].

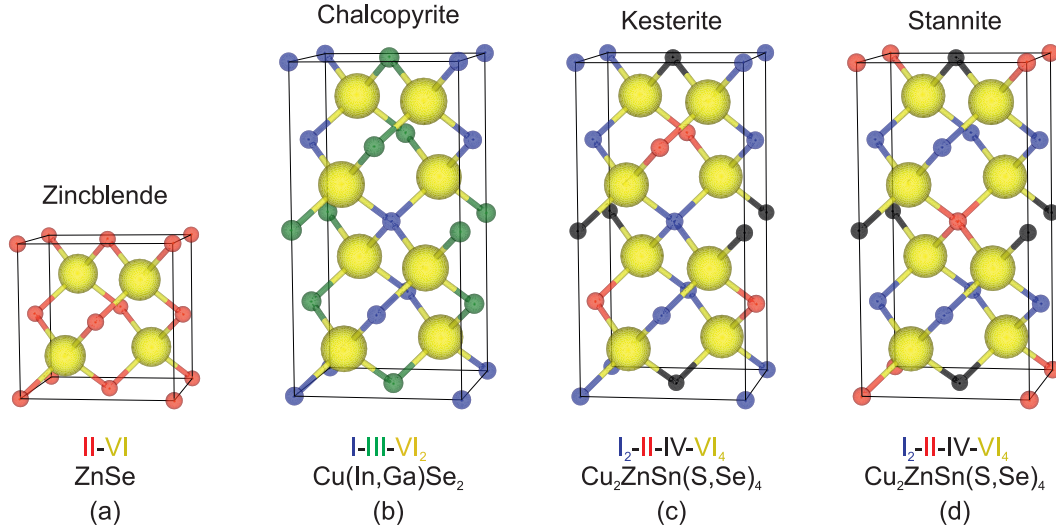


Figure 2.1: Crystal structures and example compounds: Starting from the zincblende structure (a) the chalcopyrite structure (b) is obtained if the group-II element is substituted alternately by a group-I and group-III atom. The kesterite structure (c) is then obtained for an alternating substitution of the group-III element by a group-II and a group-IV element. There are two possible crystal structures for a $\text{I}_2\text{-II-IV-VI}_4$ semiconductor, the second one being the stannite structure (d) with pure group-I layers.

chalcopyrite structure by an alternating pattern of group-II and group-IV atoms. This crystal structure is eponymous to the $\text{Cu}_2\text{ZnSn(S,Se)}_4$ (CZTSSe) material system [32]. The above-mentioned tetragonal distortion of the unit cell is not very pronounced in the CZTSSe material system and the $c/2a$ ratio of the unit cell of both parent compounds is almost 1 as evident from Tab. 2.1.

The similarities of the crystal structures of kesterite and zincblende allow for the fabrication of high-quality epitaxial layers which are of interest for fundamental physical studies [33, 34]. However, kesterite is not the only possible crystal structure for a $\text{I}_2\text{-II-IV-VI}_4$ semiconductor. For the same chemical composition the stannite structure (Fig. 2.1(d), space group $I\bar{4}2m$) exhibits a similar unit cell but with a characteristic atomic arrangement of pure group-I layers [32]².

The question whether $\text{Cu}_2\text{ZnSn(S,Se)}_4$ crystallizes in the kesterite or the stannite structure cannot be answered easily by standard thin-film characterization methods such as X-ray diffraction (XRD) or Raman spectroscopy.

²The stannite structure is derived from the CuAu(001) ordering of a I-III-VI_2 semiconductor [35].

Table 2.1: Lattice constants of the chalcopyrite [36, 37] and kesterite [11] parent compounds. The chalcopyrite unit cell undergoes a transition from a stretched (CuInSe_2) to a compressed (CuGaSe_2) unit cell whereas both kesterite compounds remain almost pseudocubic.

| Compound | a (Å) | c (Å) | c/2a |
|------------------------------|-------|--------|--------|
| CuInSe_2 | 5.782 | 11.720 | 1.013 |
| CuGaSe_2 | 5.596 | 11.000 | 0.983 |
| $\text{Cu}_2\text{ZnSnS}_4$ | 5.419 | 10.854 | 1.0015 |
| $\text{Cu}_2\text{ZnSnSe}_4$ | 5.695 | 11.345 | 0.9960 |

Since XRD is not sensitive to the occupation of the individual lattice sites within the unit cell due to similar structure factors of the constituting atoms it is not possible to distinguish kesterite from stannite. Using polarized Raman spectroscopy it would in principle be possible to discern the difference between these two crystal structures since the irreducible representations for the phonon modes differ for the kesterite and stannite structure [38]. However, this approach cannot be applied to solar cell relevant absorber layers as they are polycrystalline and do not exhibit defined crystal axes.

Density Functional Theory (DFT) studies predicted kesterite to be the ground state and thus the stable phase [39, 40] of $\text{Cu}_2\text{ZnSn}(\text{S}, \text{Se})_4$. These findings could be verified experimentally by Schorr using neutron diffraction [41].

2.1.2 Band Structure and Optical Properties

The band structures of both CIGS and CZTSSe exhibit a close resemblance to the band structure of a zincblende semiconductor such as ZnSe in the energetic region of the fundamental band gap. The reason for this lies in the structural similarity of the crystal structures – both chalcopyrite and kesterite can be derived from the zincblende structure as it was shown in the previous subsection. The main difference, however, is a significantly lower direct band gap when compared to typical II–VI compounds due to the presence of Cu-3d states [30] and a displacement of the anions compared to a crystal structure with an ideal tetrahedral coordination of atoms [42].

For the chalcopyrite compounds the valence band (VB) states arise due to a hybridization of the Cu-3d orbitals and the Se-4p orbitals [42]. The conduction band states are due to a hybridization of Se-s, Se-p and In/Ga-s orbitals [43].

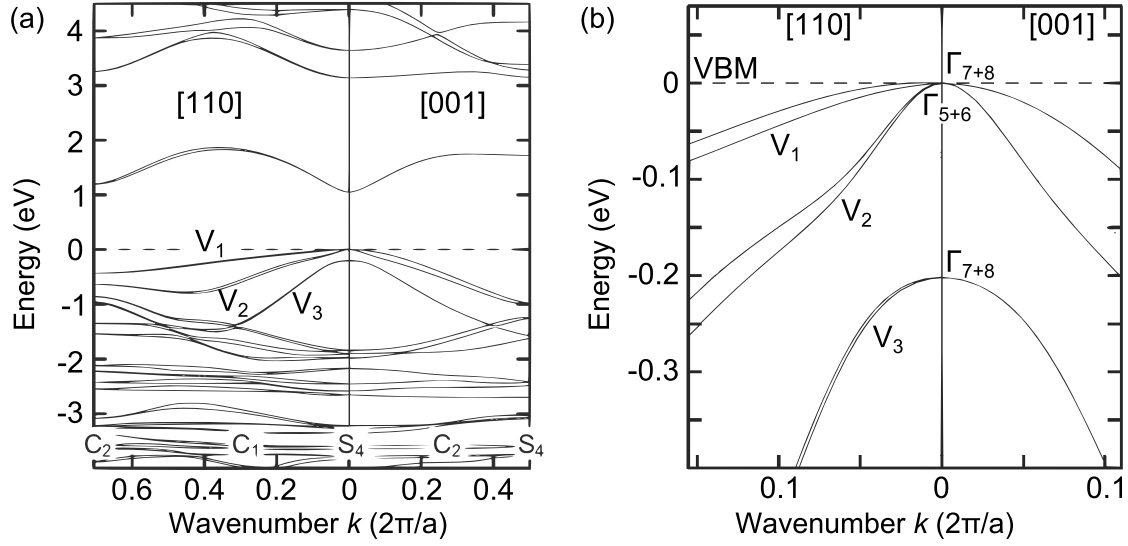


Figure 2.2: (a) Calculated band structure of kesterite $\text{Cu}_2\text{ZnSnSe}_4$ after Persson [45] for the [001] and [110] direction and a more detailed view (b) on the three uppermost valence bands. Both parent compounds $\text{Cu}_2\text{ZnSnS}_4$ (not shown here) and $\text{Cu}_2\text{ZnSnSe}_4$ show a direct band gap at $k = 0$.

At the Γ point the degeneracy of the three uppermost valence bands V_1 , V_2 and V_3 is lifted due to the combination of a crystal-field splitting Δ_{CF} and a spin-orbit splitting Δ_{SO} . The first is induced by the lowered symmetry compared to the zincblende structure which mainly stems from the tetragonal distortion of the unit cell as described in subsection 2.1.1. It is noteworthy that the sign of the crystal-field splitting changes – and consequently the lineup of the two topmost valence bands – when going from the chalcopyrite parent compounds CuInSe_2 to CuGaSe_2 [44]. This can be explained by the fact that the unit cell distortion is changing from an expansion to a compression along the \mathbf{c} -axis when indium is replaced by gallium [30] as it is also evident from Tab. 2.1.

In the kesterite crystal system the band structure is again modified but still resembles that of a zincblende compound. DFT calculations [39, 45, 46] have shown that the valence band states in kesterite arise from the hybridization of Cu-3d and anion p-orbitals and the conduction band (CB) states from the hybridization of anion-p and Sn-5s orbitals.

Additionally to these orbitals, calculations by Chen *et al.* showed that anion-s states also participate in the formation of the conduction band [47]. As it is the case for the chalcopyrites, there are three topmost valence bands the degeneracy of which is lifted by crystal-field and spin-orbit splitting.

Table 2.2: Calculated band gaps for kesterite (KS) and stannite (ST) parent compounds after Persson [45]. ST compounds exhibit a lower band gap than their KS pendant.

| Compound | E_g^{calc} (eV) | Δ_{CF} (meV) |
|---------------------------------|--------------------------|----------------------------|
| KS $\text{Cu}_2\text{ZnSnS}_4$ | 1.56 | -33 |
| ST $\text{Cu}_2\text{ZnSnS}_4$ | 1.42 | 77 |
| KS $\text{Cu}_2\text{ZnSnSe}_4$ | 1.05 | -7 |
| ST $\text{Cu}_2\text{ZnSnSe}_4$ | 0.89 | 70 |

In contrast to CIGS, Δ_{CF} originates mainly from the symmetry reduction as a consequence of the atomic arrangement in the unit cell instead of the tetragonal distortion $c/2a$.

Figure 2.2(a) shows the calculated band structure after Persson for $\text{Cu}_2\text{ZnSnSe}_4$ [45]. For both kesterite parent compounds, $\text{Cu}_2\text{ZnSnS}_4$ and $\text{Cu}_2\text{ZnSnSe}_4$, a direct band gap is found at the Γ point [39, 45, 46]. The same holds for the stannite phases as well, however, the calculated band gaps are slightly lower for the same chemical composition ($\Delta E \approx 150$ meV) [45]. Figure 2.2(b) depicts the valence band structure of $\text{Cu}_2\text{ZnSnSe}_4$ in more detail. The corresponding calculated values for the band gap and crystal-field splitting of the two parent compounds and crystal structures is summarized in Tab. 2.2. Since $\text{Cu}_2\text{ZnSn(S,Se)}_4$ exhibits a direct band gap independently of the two possible crystal structures kesterite or stannite, both materials would be suitable absorbers for thin-film solar cells.

However, problems may arise when both crystal structures are present within the absorber due to the slightly different band gap. This circumstance leads to carrier localization and recombination which in turn would lower the efficiency of the device [48] far below the maximum efficiency which is achievable within the Shockley–Queisser limit [13]. It has to be mentioned that similarly to the zincblende compounds selection rules dictate whether an optical transition from VB to CB is allowed depending on the polarization of the incident light relative to the crystal axis \mathbf{c} . However, selection rules are not applicable to this work since the investigated samples comprise polycrystalline absorber layers without a defined crystal orientation.

An important aspect of both CIGS and CZTSSe is the tunability of the band gap E_g . A very important quantity in CIGS is the gallium content x (or GGI) which is defined as:

$$x = \frac{[\text{Ga}]}{[\text{Ga}] + [\text{In}]}$$

for the material $\text{CuIn}_{1-x}\text{Ga}_x\text{Se}_2$.

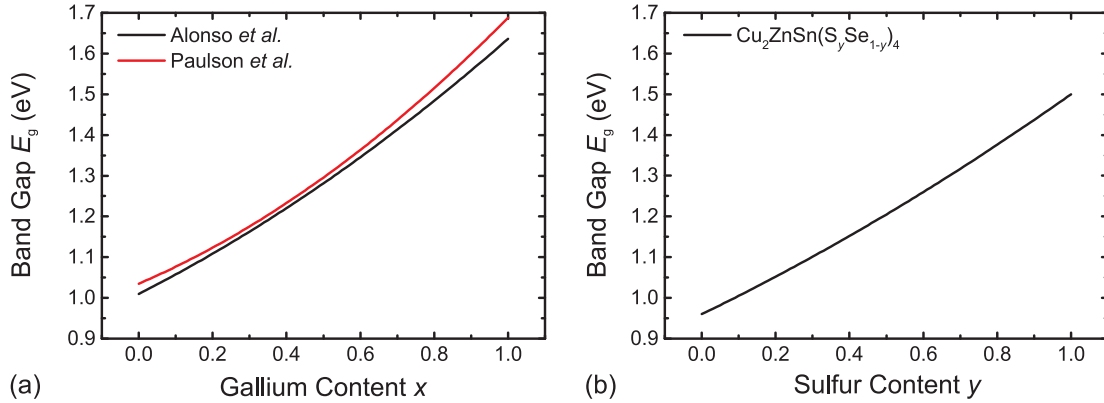


Figure 2.3: (a) Measured parabolic dependence of the fundamental band gap of CIGS on the gallium content x [52, 53]. The dependence shows a clearly parabolic behavior. (b) Calculated dependence of the kesterite band gap on the sulfur content y [40]. The dependence is almost linear and exhibits a very low bowing parameter of $b = 0.1$ eV.

The dependence of the fundamental band gap on the gallium content x is shown in Fig. 2.3(a). E_g can be tuned within a range of 1.0–1.6 eV which is the ideal range of a single-junction solar cell under AM1.5 illumination [13]. Furthermore, it allows for more elaborate solar cell concepts such as band gap gradients [49, 50] and tandem cells [51]. The dependence of the band gap on x is of a parabolic nature and the so-called bowing parameter³ varies slightly depending on the publication one is referring to [52, 53]. A more detailed investigation of this dependence on an atomic scale was performed by Schnohr *et al.* using extended X-ray absorption fine structure spectroscopy [54].

It should be noted that the band gap can also be tuned by varying the chalcogen ratio y which is defined as

$$y = \frac{[\text{S}]}{[\text{S}] + [\text{Se}]}$$

for the material $\text{Cu}(\text{In}_{1-x}\text{Ga}_x)(\text{S}_y\text{Se}_{1-y})_2$ [30, 55]. However, this circumstance will not be given more attention since all CIGS solar cells investigated in this work had pure selenide absorber layers. As will be discussed in the following section, solar-cell-relevant CIGS absorber layers are grown with a clear copper deficiency. Since Cu-3d states are involved in the formation of the VB states this deficiency has an impact on the band gap as well. However, there is no clear picture about this aspect in literature and reported results are not consistent. Chichibu *et al.* reported a lowering of the band gap [56] whereas Han *et al.* reported an increase in band gap

³The bowing parameter is the quadratic coefficient of the dependence of E_g on either x or y .

energy with decreasing copper content [57]. All the factors influencing the band gap make it clear that it is important to have a precise characterization technique for the band gap of an absorber material such as modulation spectroscopy.

In the case of $\text{Cu}_2\text{ZnSn}(\text{S},\text{Se})_4$ the band gap can be adjusted by a variation of the chalcogen ratio y as well. DFT predicts an almost linear dependence of the band gap as shown in Fig. 2.3(b) [40]. Cation substitution can also be applied to adjust the band gap. This can be achieved by either substituting the group-II element [58] or the group-IV element [59]. However, detailed experimental investigations of the band bowing are still sparse. Levenco *et al.* investigated the influence of the chalcogen ratio y on the band gap of $\text{Cu}_2\text{ZnSn}(\text{S},\text{Se})_4$ single crystals [60] but an investigation of the band bowing on application-relevant solar cell absorber layers remains to be done. A possible reason for this missing investigation in literature could be the lack of high-quality kesterite layers for different chalcogen ratios due to the more complicated formation reaction which will be discussed in the next subsection.

Since both $\text{Cu}(\text{In},\text{Ga})\text{Se}_2$ and $\text{Cu}_2\text{ZnSn}(\text{S},\text{Se})_4$ represent disordered systems, the term band gap throughout this work refers to the so-called mobility edge or percolation threshold – the proper term for the energetic position at which delocalized states can form.

2.1.3 Important Defects and Secondary Phases

For both material systems, CIGS as well as CZTSSe, defects play a crucial role in physical key properties of the absorber layer and are thus directly relevant for solar cell performance. The formation of defects within the CIGS material system will only be discussed briefly since the majority of experiments of this work was performed on CZTSSe solar cells. For a more detailed review of defects in CIGS the reader may refer to the book by Scheer and Schock [61].

It has to be strongly emphasized that application-relevant thin-film solar cell absorbers do not exhibit chemical stoichiometry despite the fact that they are usually described as $\text{Cu}(\text{In},\text{Ga})\text{Se}_2$ or $\text{Cu}_2\text{ZnSn}(\text{S},\text{Se})_4$. Usually, $\text{Cu}(\text{In},\text{Ga})\text{Se}_2$ absorber layers are grown Cu-poor in order to avoid the formation of Cu_xSe phases which short-circuit the solar cell due to the conductive nature of these compounds.

DFT calculations for CuInSe_2 have identified the copper vacancy V_{Cu} as the point defect with the lowest formation energy [62]. Concerning defect complexes, the $[V_{\text{Cu}} + \text{In}_{\text{Cu}}]$ defect complex has the lowest formation energy and is favored by the Cu-poor composition of the absorber layers. The individual point defects play an

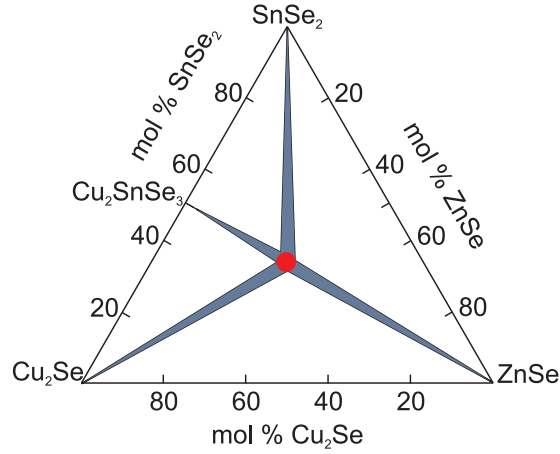
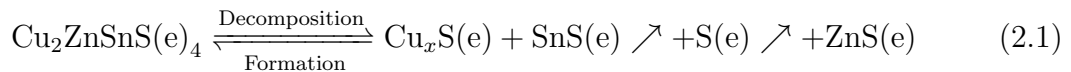


Figure 2.4: Phase diagram after Dudchak [72]. The stoichiometric point (red) is very small and even small deviations lead to the formation of secondary phases besides the kesterite phase. Grey lines indicate compositions at which one single secondary phase is formed.

important role in the doping of the absorber layers. Calculations by Pohl and Albe [63] suggest that the shallowest donor defect is the indium copper antisite In_{Cu} and the shallowest acceptor defect is the copper vacancy V_{Cu} . This assignment of defects to donor and acceptor states is consistent with other reports in literature [64–67] and underlines the role of the copper vacancy as the main defect responsible for the p-type conductivity in $\text{Cu}(\text{In,Ga})\text{Se}_2$ absorber layers.

The situation for $\text{Cu}_2\text{ZnSn}(\text{S,Se})_4$ is more complicated concerning defects and secondary phases due to the more complicated unit cell structure. One key aspect in the discussion of defects and secondary phases in CZTSSe is the decomposition reaction of this compound [68]:



The decomposition and formation of kesterite is an equilibrium reaction and takes place at temperatures of 500–600 °C depending on which parent compound is fabricated and which process is used. The main problem in this reaction is that two of the four products on the right-hand side of eq. 2.1 are volatile at these temperatures and evaporate from the film. This drives the reaction further towards the right-hand side and favors the decomposition of kesterite. In order to prevent tin and chalcogen loss a high partial pressure in the atmosphere surrounding the sample is necessary and is achieved by introducing excess chalcogen (and preferentially also tin) in the form of sulfur/selenium and/or tin sulfide/selenide [69–71]. A pseudo-

ternary phase diagram for $\text{Cu}_2\text{ZnSnSe}_4$ was introduced by Dudchak *et al.* [72] and is shown in Fig. 2.4. Although it is pseudo-ternary the picture can be used as an orientation for the entire kesterite material system within the context relevant to this work. Small deviations from ideal stoichiometry already lead to the formation of different secondary phases, most of which are detrimental to solar cell performance. While $\text{Cu}_x\text{S}(\text{e})$ compounds short-circuit the device, other secondary phases have a band gap in the energetic vicinity of the kesterite band gap leading to band gap fluctuations. These result in a lowering of the open-circuit voltage and the efficiency of the solar cell [48]. Secondary phases with a higher band gap than kesterite lead to current blocking if present abundantly. In the case of $\text{Cu}_2\text{ZnSnSe}_4$ the formation of ZnSe matrices has been shown by atom probe tomography [73] and an electron beam-induced current study [74]. A review of the occurrence and consequences of the individual secondary phases was given by Siebentritt [75].

However, not only secondary phases affect the physical properties of CZTSSe layers. In a quaternary semiconductor the possibilities of defect formation are more numerous than in the respective chalcopyrite or II–VI analog. In the case of $\text{Cu}_2\text{ZnSn}(\text{S},\text{Se})_4$ DFT calculations suggest that the formation of shallow acceptor states is more likely than the formation of shallow donor states which explains the intrinsic p-type nature of conductivity in kesterite compounds [35, 47]. Furthermore, in contrast to CuInSe_2 the Cu_{Zn} antisite is the defect with the lowest formation energy whereas the copper vacancy V_{Cu} has the second lowest formation energy. The energetic position of V_{Cu} is close to the valence band maximum (VBM) whereas the position of Cu_{Zn} is further within the band gap. This alignment of energy levels is detrimental to kesterite solar cells since it lowers the open-circuit voltage via carrier trapping and subsequent bulk recombination. In solar cell fabrication this is circumvented by using Cu-poor and Zn-rich growth conditions in order to enhance the population of shallow V_{Cu} defects relative to Cu_{Zn} defects [35].

By means of DFT it has further been shown that the mixed crystal $\text{Cu}_2\text{ZnSn}(\text{S},\text{Se})_4$ shows similar properties as the parent compounds [76]. A detailed presentation of the defect nature in kesterites would go beyond the scope of this discussion.

However, the existence of defect complexes should be mentioned explicitly at this point. Similar to CIGS the formation of defect pairs is energetically more favorable due to charge neutrality than the formation of the individual defects. A particularly interesting one is the $[\text{Cu}_{\text{Zn}}+\text{Zn}_{\text{Cu}}]$ antisite complex which is responsible for a cation disorder within the Cu–Zn lattice planes of the kesterite unit cell [41]. This defect has been shown to influence the band gap of $\text{Cu}_2\text{ZnSnS}_4$ theoretically [77] and it will be shown experimentally within this work how it is possible to tune the band gap of CZTSSe solar cell absorbers by adjusting the degree of Cu–Zn disorder. The theoretical background and experimental details will be discussed in chapter 7.

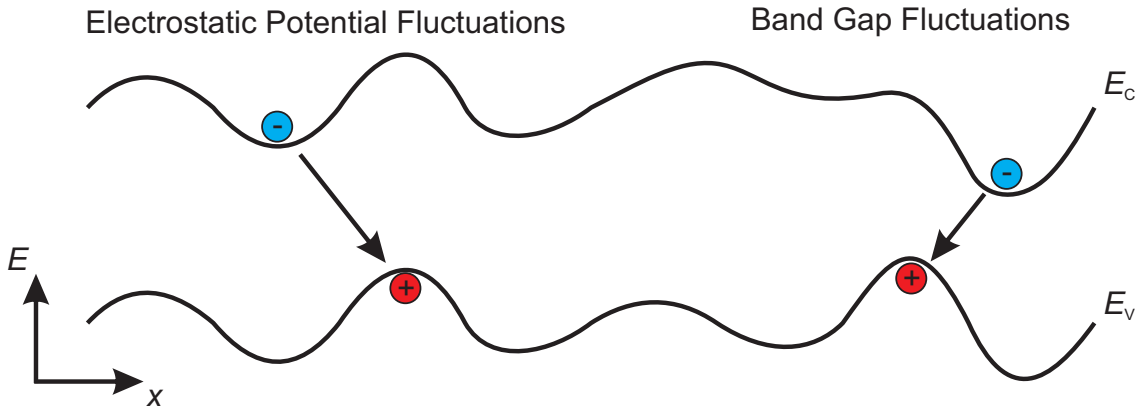


Figure 2.5: Schematic band alignment in the case of electrostatic potential fluctuations (EPF) and band gap fluctuations (BGF). In the case of EPF the band edges fluctuate in parallel whereas for BGF the band gap fluctuates spatially. In both cases transitions can occur at energies below the average band gap.

It has to be mentioned that the defect density in kesterites exceeds the carrier concentration by orders of magnitude [77]. Furthermore, it has been shown that compensation plays a very important role [47]. Charged defects lead to potential fluctuations (that means a fluctuation of both VB and CB in parallel). Such fluctuations have been reported recently to be possibly responsible for the V_{OC} -deficit in kesterite solar cells [78]. The reason for that is an enhanced spatially indirect recombination of localized carriers which is currently still under investigation [79, 80]. In contrast to that, structural disorder such as clustering of defects with a fluctuation length over several hundreds of unit cells leads to fluctuations of the band gap itself (CB and VB do not fluctuate in parallel). This causes similar effects such as carrier localization and modified recombination of carriers which would also be detrimental to solar cell performance as discussed by Rau and Werner [81]. A schematic comparison of the two situations is shown in Fig. 2.5. These effects have been investigated within this work by means of photoluminescence and photoluminescence excitation measurements and the results as well as a more detailed background will be presented in chapter 6.

2.2 Chalcogenide Absorber Thin-Film Solar Cells

The aim of this section is to provide a basic overview on chalcogenide thin-film solar cells. In the first part, the working principle of the solar cell structure is presented and the different concepts of the functional parts are summarized. The discussion of the individual layers is based on the book "Chalcogenide Photovoltaics" by Scheer and Schock [61]. Further references are added when necessary. In the second part example fabrication procedures of CIGS and CZTSSe absorber layers are presented with a focus on the routes which are employed to fabricate the solar cells which were investigated in this work.

2.2.1 Thin-Film Solar Cell Structure

Figure 2.6(a) shows the functional layers of a thin-film solar cell including typical thicknesses of the individual layers where necessary. In terms of substrate and back contact material two main concepts are distinguishable. Most thin-film solar cells are fabricated on molybdenum-coated soda lime glass (Mo-SLG) in which Mo serves as the back contact. This choice is due to comparatively low cost and a high melting point of Mo. The metal back contact is usually deposited onto the glass substrate via sputtering or electron beam evaporation. Furthermore, soda lime glass (SLG) has the advantage that it can act as a sodium source for a later CIGS layer which has been proven to be beneficial for the solar cell performance [82]. In the case of CZTSSe the role of sodium is still under investigation [83]. A particularly interesting alternative to Mo-SLG are polymer films which allow for flexible solar cells with comparably high efficiencies [84].

An important benefit of Mo in CIGS solar cells is the formation of MoSe_2 at the metal back contact during film formation. It could be shown that a thin layer of MoSe_2 assists in the formation of an ohmic back contact. In CZTSSe thicker molybdenum chalcogenide layers are observed and the effect of MoS(e)_2 is reported to be rather detrimental to solar cell performance [85]. The formation of this interfacial layer can be prevented by, e.g., the use of a TiN diffusion barrier [86].

The absorber layer either consists of a CIGS or a CZTSSe layer with a thickness in the range of 1–3 μm . The absorber layer will be given more attention in the next subsection which is why it will not be discussed at this point.

Since both CIGS and CZTSSe show intrinsic p-type conductivity and extrinsic doping is very challenging, it is not feasible to form a p–n homojunction as it is the case in silicon solar cells. This is why in most cases a thin layer of n-CdS ($E_g \approx 2.4 \text{ eV}$) is used to form a p–n heterojunction.

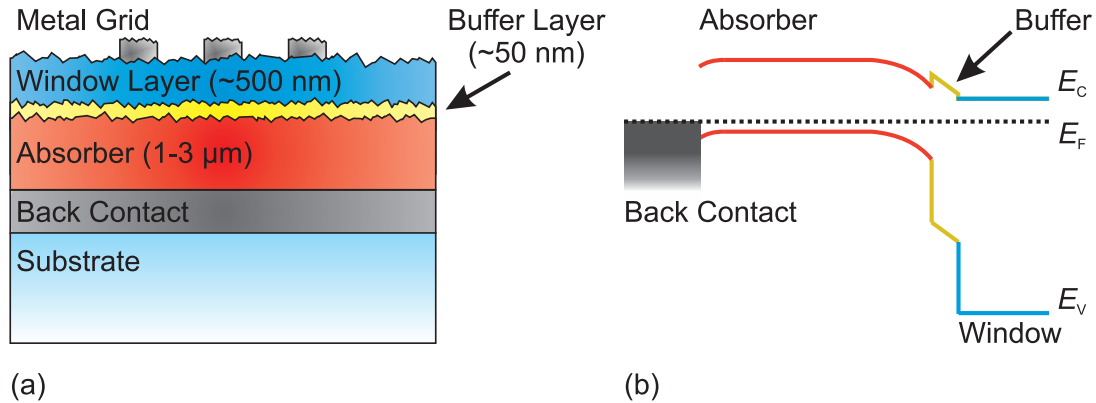


Figure 2.6: (a) Principle thin-film solar cell structure with typical thicknesses of the functional layers. (b) Band alignment within the different functional layers. Light is incident from the right-hand side of the figure.

The layer is deposited using chemical bath deposition (CBD) since this yields higher efficiencies than evaporated CdS buffer layers. The reason for that is believed to be superior interface properties of CBD-CdS layers [87]. Furthermore, in CIGS, the formation of a so-called ordered vacancy complex turned out to be beneficial for the junction formation [88]. However, an increasing effort is made to remove CdS from the solar cell by using different buffer materials such as In_2S_3 , $\text{Zn}(\text{O},\text{S})$ or even organic layers [89–92]. An important aspect of the buffer layer is the conduction band alignment relative to the absorber layer. It is desirable to have a spike-like arrangement with the conduction band of the buffer layer slightly above the CB of the absorber. A cliff-like CB alignment enhances interface recombination and is detrimental to solar cell performance. The CB alignment of different buffer layers with both CIGS and CZTSSe absorbers as well as the interface properties are still subject to current investigations [76, 93–98].

The window layer has to fulfil two main requirements. Since it is the uppermost layer it has to be transparent over a large spectral range which is why large band gap semiconductors such as sputtered ZnO or indium tin oxide (ITO) [99] are commonly used. In addition to a high transparency, a high conductivity is necessary for a sufficient carrier extraction from the buffer layer towards the metal electrodes which is why the window layer is additionally n-type doped.

Metal grids are introduced in order to guarantee an optimum carrier extraction and are usually made of an Al:Ni alloy.

The resulting band structure is shown in Fig. 2.6(b). Light is incident from the right-hand side of the structure.

So far, most CZTSSe solar cells were designed by simply replacing the absorber in a CIGS solar cell by a CZTSSe layer leaving the remaining parts of the device unaltered. All samples investigated within this work had a standard layer sequence as described in the list below. All of the samples which were investigated in the course of this work were either fabricated at the Zentrum für Sonnenenergie- und Wasserstoff-Forschung Baden-Württemberg (ZSW), the University of Luxemburg (Uni Lux) or the University of Uppsala (Uni Upp). The layer sequences of the devices were:

- **Chalcopyrite solar cells:**
SLG/Mo/Cu(In,Ga)Se₂ /CdS/i-ZnO/ZnO:Al/Al:Ni grid
- **Kesterite solar cells (ZSW):**
SLG/Mo/Cu₂ZnSn(S,Se)₄ /CdS/i-ZnO/ZnO:Al
- **Kesterite solar cells (Uni Lux):**
SLG/Mo/Cu₂ZnSnSe₄ /CdS/i-ZnO/ZnO:Al/Al:Ni grid
- **Kesterite solar cells (Uni Upp):**
SLG/Mo/Cu₂ZnSnS₄ /CdS/i-ZnO/ZnO:Al/Al:Ni grid

In case further information about the cells is necessary, it will be given in the respective section.

2.2.2 Fabrication of Thin-Film Absorber Layers

In this subsection a short overview on the common fabrication techniques of chalcogenide absorber layers will be given. Two basic principles of fabrication can be distinguished:

- One step chalcogenide formation at high temperatures with all elements present
- Chalcogenization of precursors with a low amount of or without sulfur or selenium

Furthermore, precursor layer preparation can be classified as either vacuum- or non-vacuum-based, the latter involving solution- or nanoparticle-based approaches.

Cu(In,Ga)Se₂ Absorber Layers

The most successful approach to fabricate CIGS absorber layers is coevaporation of elements in a vacuum system [7]. During deposition metal fluxes are varied relative to the chalcogen flux in order to yield the desired composition in terms of copper content, band gap, etc. The substrate is typically kept at temperatures between 300–500 °C depending on the stage of the process in order to facilitate the formation reaction. A more detailed insight into the fabrication will not be given at this point since it is not providing any more relevant information to this work and, furthermore, many of the fabrication procedures are confidential. In contrast to vacuum-based approaches, ink-based approaches for the fabrication of CIGS layers still lack in final device efficiency. However, the perspective of a printable solar cell makes this preparation method a very interesting approach [100,101].

Cu₂ZnSn(S,Se)₄ Absorber Layers

Since kesterites are a younger material system in photovoltaics and the layer preparation turned out to be very challenging, the fabrication methods are still various. Only two main preparation methods will be discussed in more detail as they were used to fabricate the kesterite solar cells which were mainly investigated in this work. Other approaches will only be mentioned and the reader will be referred to literature.

An important difference to CIGS is that the world record efficiency of $\eta = 12.6\%$ for CZTSSe was achieved using a solution-based approach developed at IBM [12]. However, it remains questionable whether this preparation will make it into a commercial production of solar cells since the use of the toxic and explosive solvent hydrazine is necessary.

A more application-relevant approach is the one which is used at ZSW [102]. Copper acetate, zinc chloride and tin chloride are dissolved in dimethyl sulfoxide (DMSO). Furthermore thiourea is added as a sulfur donor. This results in an ink which is doctor-bladed onto a Mo-SLG substrate. This precursor layer is then annealed in a selenium atmosphere and finally yields a Cu₂ZnSn(S,Se)₄ layer which is then processed further into a solar cell with a standard layer sequence. The procedure is based on an approach by Ki and Hillhouse [69] and has been developed further. Recently, efficiencies of up to 11.1% could be achieved by Collord *et al.* by further improvements of this procedure using doping agents [103].

Noticeable efficiencies of 9.15% using coevaporation were achieved by Repins *et al.* [71]. The challenge of this fabrication method lies in a sufficient chalcogen partial

pressure to prevent kesterite decomposition as described in eq. 2.1 at temperatures as high as 500 °C. Within this work solar cells based on coevaporated $\text{Cu}_2\text{ZnSnSe}_4$ layers were investigated. The absorbers have been fabricated using a modified fabrication procedure based on the Repins process [104]. Recently, the efficiency of solar cells based coevaporated absorbers could be improved further up to 11.6% [105].

Generally, most of the reported fabrication procedures are still two-step approaches which only differ in the fabrication of the precursor layer. The latter can be formed by various techniques such as nanoparticle inks [106], sputtering of metallic precursors [107, 108] or binary layers [109] or chemical bath deposition [110]. What is common to all techniques is a subsequent high-temperature annealing step in a chalcogen atmosphere.

2.3 Summary and Relevance for this Work

In summary, it can be stated that – from a physical point of view – both materials, CIGS and CZTSSe, are good alternatives to the well-established silicon. However, it is not correct to speak of a single material "CIGS" or "CZTSSe", respectively. Both represent entire material systems and the physical properties strongly depend on both the composition and the fabrication method. This is mainly due to the fact that there are more degrees of freedom in terms of defects and secondary phases as there are in silicon. In the case of CIGS properties such as the band bowing or even the band gap itself differ from publication to publication, mainly because there is not one defined reference sample.

Ever since $\text{Cu}_2\text{ZnSn}(\text{S},\text{Se})_4$ gained more attention as an absorber material there has been a discussion about the band gap of the material [14]. The discrepancies on the band gap were mainly due to different measurement methods which were applied. However, this emphasizes the necessity of a proper measurement technique for the band gap of a thin-film solar cell absorber – ideally in an entire cell.

It has to be easy, precise, reproducible and should not rely on device parameters such as diode characteristics. The standard determination technique in the solar cell community is the extrapolation of the low-energy slope of the external quantum efficiency (EQE) of a solar cell [111]. Although this might yield a good approximation of the band gap in high-quality solar cell absorbers such as Si, GaAs, GaInP or $\text{Cu}(\text{In},\text{Ga})\text{Se}_2$ it is a rather naive approach for the determination of the band gap of a non-ideal semiconductor such as $\text{Cu}_2\text{ZnSn}(\text{S},\text{Se})_4$. This particular technique assumes that the low-energy slope of the EQE is exclusively governed by the absorption of the absorber layer. This is certainly not the case in a material which is

prone to exhibit carrier localization due to potential or band gap fluctuations and an incomplete carrier extraction in consequence. This suggests that the band gap energies determined by EQE are rather too large. Even if the main contributing effect to the lineshape of the EQE was the absorption of the $\text{Cu}_2\text{ZnSn}(\text{S},\text{Se})_4$ layer it would still raise the question which absorption model should be employed since $\text{Cu}_2\text{ZnSn}(\text{S},\text{Se})_4$ exhibits a strong tailing in the absorption [78]. This topic will be discussed further in chapter 6.

Photoluminescence spectroscopy (PL) is a good technique to study defects within a semiconductor due to the nature of charge carriers to relax to the lowest energetic state. This is what this technique will be used for within this work. However, it will also be shown that the photoluminescence of $\text{Cu}_2\text{ZnSn}(\text{S},\text{Se})_4$ layers does not necessarily coincide with the band gap of the material. As a complementary technique photoluminescence excitation spectroscopy (PLE) will be used to investigate the optical absorption transition to gain insights into the nature of radiative recombination.

Modulation spectroscopy techniques such as electroreflectance offer the possibility of an easy and convenient experiment to measure the band gap of a semiconductor. They are well-established in semiconductor physics and can even be applied to finished solar cells. Therefore, it is possible to gain insights into the band structure of the device itself and one does not have to make comparison measurements such as absorption on bare films leaving the open question whether CZTSSe growth on glass and Mo-SLG is comparable. This is why the next chapter will mainly focus on this experimental technique and its implementation in the laboratory. PL and PLE will also be introduced as complementary and supporting experimental techniques.

Chapter 3

Experimental Techniques

This chapter gives an overview on the main experimental techniques which were applied within this work. These include modulation spectroscopy, photoluminescence and photoluminescence excitation spectroscopy. Since a major part of this work was dedicated to further develop the measurement and the analysis of modulated reflectance spectra of thin-film solar cells, the first part of this chapter presents the physical mechanism of this measurement technique.

PL is a valuable method to study the radiative recombination processes in semiconductors and represents a complementary technique to modulation spectroscopy since it measures the downward transition of CB carriers to the VB and is furthermore very sensitive to defect levels. Within this work, photoluminescence excitation spectroscopy has been used as an auxiliary technique to verify the results from modulated reflectance spectra. It is a particularly powerful technique when it comes to determining the nature of optical transitions in disordered systems such as $\text{Cu}_2\text{ZnSn}(\text{S,Se})_4$. Since these last two techniques have not been developed further but only applied within this work the reader will not be given a more detailed introduction. If necessary, further information will be provided within the respective chapters.

The used setups have been constructed and improved within this work and the Master's theses of Christian Huber [112], Christian Zimmermann [113], David Sperber [114], and Mario Lang [115]. The three experimental setups have to be seen as a whole which is why the reader is recommended to read all parts of the experimental setup sections to gain a full overview.

3.1 Modulation Spectroscopy

3.1.1 Optical Properties of Semiconductors

First, a very brief overview will be given on the relevant optical quantities which are necessary to describe the physical mechanism of modulation spectroscopy. These relations can also be found in standard textbooks on optics [116, 117].

The optical properties of a semiconductor are described by the complex dielectric function $\epsilon(\omega)$. Via the susceptibility $\chi(\omega)$ it connects the polarization \mathcal{P} of a medium and the applied electrical field \mathcal{E} .

$$\mathcal{P}(\omega) = \epsilon_0 \underbrace{(\epsilon(\omega) - 1)}_{\chi(\omega)} \mathcal{E}(\omega) \quad (3.1)$$

Generally, $\epsilon(\omega)$ is a second-rank tensor and observations such as birefringence are due to this fact. However, in this work a directional dependence of $\epsilon(\omega)$ is neglected due to the polycrystalline nature of the investigated samples and thus $\epsilon(\omega)$ will be considered as a scalar quantity. Furthermore, all measurements are assumed to take place in the regime of linear optics.

Excitations of a semiconductor are described by resonances in the dielectric function. Interband transitions are an example of such resonances and are particularly important for this work. The imaginary part $\epsilon_2(\omega)$ of the dielectric function is directly connected to the joint density of states $J(E_{CV})$ (JDOS) which can be seen in the energetic region of the fundamental band gap E_g of a direct semiconductor without the consideration of lifetime broadening:

$$\epsilon_2(\omega) = \frac{B}{\omega^2} \sqrt{\hbar\omega - E_g}. \quad (3.2)$$

ϵ_2 directly reflects the square-root shape of the JDOS in a three-dimensional semiconductor assuming parabolic bands. B represents a proportionality factor which is independent of ω .

Furthermore, causality dictates that the real and imaginary part of the dielectric function have to be connected mathematically via the Kramers–Kronig relations

$$\epsilon_1(\omega) - 1 = \frac{2}{\pi} \text{P} \int_0^\infty \frac{\omega' \epsilon_2(\omega')}{\omega'^2 - \omega^2} d\omega' \quad (3.3)$$

$$\epsilon_2(\omega) = \frac{2\omega}{\pi} \text{P} \int_0^\infty \frac{\epsilon_1(\omega')}{\omega^2 - \omega'^2} d\omega' \quad (3.4)$$

where P denotes the Cauchy principal value of the integral. It should be noted that these relations generally hold for quantities which are calculated from causal quantities. In particular, they also connect the real and imaginary part of the refractive index and can be applied to modulated reflectance spectra as it will be presented later.

For the description of electromagnetic waves in matter it is convenient to introduce the complex refractive index $\tilde{n}(\omega) = n(\omega) + i\kappa(\omega)$ with

$$\tilde{n}^2(\omega) = \epsilon(\omega) \quad \epsilon_1(\omega) = n^2(\omega) - \kappa^2(\omega) \quad \epsilon_2(\omega) = 2n(\omega)\kappa(\omega). \quad (3.5)$$

Here, $n(\omega)$ describes the change of the phase velocity within the medium whereas $\kappa(\omega)$ describes the amplitude damping of the electromagnetic wave. Using the Fresnel equations one can further calculate transmittivity and reflectivity of a semiconductor in dependence of the angle of incidence of the light and the refractive index. However, this will not be discussed in more detail at this point. Instead, the concept of modulation spectroscopy will be introduced in the following – in particular the modifications of the optical properties of a semiconductor which are induced as a consequence of a change in the dielectric function $\Delta\epsilon(\omega)$.

3.1.2 Main Idea of Modulation Spectroscopy

As discussed in the previous subsection, the reflectivity of a material is a function of the refractive index and in turn of the dielectric function. In a reflectance spectrum $R(\omega)$ resonances in the dielectric function are visible but they are usually broadened and it is therefore difficult to determine their exact energetic position. Furthermore, the measured lineshapes are distorted by instrument responses and have to be corrected for them first.

Modulation spectroscopy techniques rely on a simple physical principle. If a quantity f , e.g., the reflectivity R or the transmittivity T , depends on the dielectric function, that is $f(\epsilon(\omega))$, it will react to small changes $\Delta\epsilon$ linearly in a first approximation:

$$\Delta f = \frac{df}{d\epsilon} \Delta\epsilon. \quad (3.6)$$

In order to obtain a normalized quantity, both sides of eq. 3.6 are multiplied by $1/f = \frac{d \ln f}{df}$:

$$\frac{\Delta f}{f} = \frac{d \ln f}{df} \frac{df}{d\epsilon} \Delta\epsilon = \frac{d \ln f}{d\epsilon} \Delta\epsilon. \quad (3.7)$$

These small changes $\Delta\epsilon$ can be induced by various perturbations of the semiconductor such as heating, strain or an applied electric field \mathcal{E} . Especially the last one

will be given more attention in the following since the corresponding technique – electroreflectance – was applied in this work. It is important for this work that the described function $f(\epsilon(\omega))$ can represent various optical quantities. Modulated spectra can either occur in reflection $\Delta R/R$, transmission $\Delta T/T$ or, as will be shown in chapter 5, in diffuse reflection $\Delta R_D/R_D$. The measurement of normalized quantities $\Delta R/R$, $\Delta T/T$, or $\Delta R_D/R_D$ has the advantage of self-referencing. This means that influences such as detector responses or the spectrum of the incident light are automatically corrected for.

What is common to all modulation techniques is that they result in a change in the dielectric function mainly in the vicinity of a resonance of $\epsilon(\omega)$, which means

$$\Delta\epsilon(\hbar\omega \approx E_{\text{res}}) \neq 0$$

with the energetic position of the resonance E_{res} . Consequently, this means that the measured signal $\frac{\Delta f}{f}$ vanishes far away from a dielectric resonance and only yields a contribution in the vicinity of, e.g., critical points in the band structure, such as E_g . This is the main difference to non-modulating techniques – the measured lineshapes are more pronounced in the vicinity of resonances and a measurement background is suppressed which simplifies the determination of E_{res} .

3.1.3 Physical Mechanism and Lineshape Considerations

Seraphin and Bottka discovered a change in the refractive index of Ge and GaAs in the presence of an electric field. They stated that this “...extends the Franz–Keldysh effect to reflection phenomena...” [118] which can be considered as the experimental birth of modulation spectroscopy, in particular electroreflectance. Up to then the Franz–Keldysh effect was only known as a shift of the absorption edge of a semiconductor towards lower energies in the presence of an external electric field. A detailed theoretical description showed, that this change in the refractive index can be used to analyze the band structure of a semiconductor [119].

By making appropriate assumptions, Aspnes derived a simple expression for $\Delta\epsilon$ which is still commonly used as the standard evaluation method. In the following, the physical mechanism of electroreflectance will be discussed and an expression for the change in the dielectric function $\Delta\epsilon(\omega)$ will be derived. The derivation is based on the publication by Aspnes [15]. Furthermore, a very detailed discussion of the mechanism of modulation spectroscopy can be found in the Master’s thesis of Christian Huber [112].

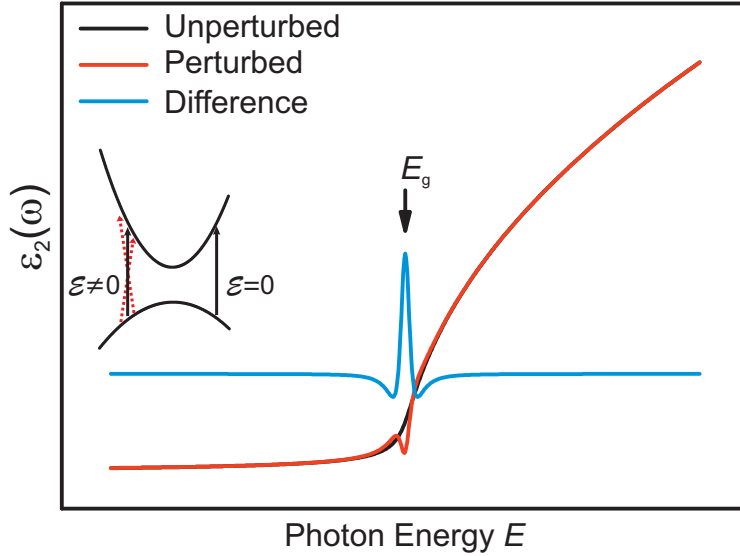


Figure 3.1: Imaginary part $\epsilon_2(\omega)$ of the dielectric function after Aspnes [15] with (red) and without (black) an applied electric field. The difference $\Delta\epsilon_2$ (blue) is centered around the fundamental band gap and vanishes for photon energies further away from the resonance.

The application of an electric field \mathcal{E} to a semiconductor breaks the translation symmetry of the crystal. Consequently, the momentum $\hbar\mathbf{k}$ in the direction of the field is not a conserved quantity anymore. In momentum space this means that optical transitions from VB to CB are not limited to $\Delta\mathbf{k} \approx 0$ anymore and non-vertical transitions become possible within a certain range.

Assuming only lifetime broadening, the shape of the dielectric function of a semiconductor around the fundamental band gap is given approximately by [120]:

$$\epsilon(\omega) = \frac{B}{\omega^2} i \sqrt{\hbar\omega - E_g + i\Gamma}. \quad (3.8)$$

The imaginary part ϵ_2 of this expression is still approximately square-root shaped but it is washed-out due to the broadening parameter Γ .

If additionally an electric field is applied, the contributions of non-vertical transitions from VB to CB smear out the JDOS especially around E_g and a finite difference between the dielectric function with and without the electric field $\Delta\epsilon$ can be detected. This situation is illustrated in Fig. 3.1.

Low-Field Limit

Using time-dependent perturbation theory, one can derive an analytical expression for $\Delta\epsilon$ depending on the applied electric field \mathcal{E} . After Aspnes [15] the dielectric function takes the following form which can be derived from Fermi's golden rule:

$$\epsilon(\omega, \mathcal{E}, \Gamma) \propto \frac{1}{(\hbar\omega)^2} \int_{\text{B.Z.}} d^3\mathbf{k} \int_0^\infty ds e^{-\Gamma s} \exp \left[i \left(\hbar\omega s - \underbrace{\int_{-s/2}^{s/2} ds' E_{\text{CV}}(\mathbf{k} + e\mathcal{E}s')}_{\mathcal{E}=0 \Rightarrow E_{\text{CV}}(\mathbf{k})s} \right) \right] \quad (3.9)$$

where $E_{\text{CV}} = E_{\text{C}} - E_{\text{V}}$ is the interband transition energy. The integration $\int_{\text{B.Z.}} d^3\mathbf{k}$ over the first Brillouin zone (B.Z.) can be replaced by an integration over dE introducing the JDOS. Note that a momentum independent transition matrix element has been assumed and has been absorbed as a constant. For simplicity, the parameter $s = t/\hbar$ has been introduced.

The use of this expression assumes lifetime (τ) broadened states described by a broadening term $e^{-\Gamma s}$ with the broadening parameter $\Gamma \approx \frac{\hbar}{2\tau}$. Mathematically, the decay of the broadening term cuts off contributions from the second exponential function in eq. 3.9 for times longer than τ .

For a vanishing electric field this expression simplifies to the expression for the dielectric function given in eq. 3.8.

In order to determine which further simplifications can be made to eq. 3.9, it is convenient to introduce

$$(\hbar\Omega)^3 = \frac{e^2 \mathcal{E}^2 \hbar^2}{8\mu_{\parallel}} \quad (3.10)$$

as a measure of how strongly the system is perturbed by the applied electric field. μ_{\parallel} represents the interband reduced mass in the field direction. Assuming parabolic bands μ_{\parallel} is a constant.

A Taylor series of $E_{\text{CV}}(\mathbf{k} + e\mathcal{E}s')$ can be performed so that

$$E_{\text{CV}}(\mathbf{k} + e\mathcal{E}s') = E_{\text{CV}}(\mathbf{k}) + (\nabla_{\mathbf{k}} E_{\text{CV}}(\mathbf{k}))e\mathcal{E}s' + \frac{1}{2}e^2(\mathcal{E}\nabla_{\mathbf{k}})^2 E_{\text{CV}}(\mathbf{k})s'^2 + \dots \quad (3.11)$$

The integration over the symmetric interval $[-s/2, s/2]$ in the exponential function in eq. 3.9 yields a term of the order of s for the zeroth order in eq. 3.11 and a term of the order of s^3 for the quadratic term s'^2 . The linear term vanishes due to the integration over a symmetric interval. This yields an expression for the perturbed dielectric function of the form

$$\epsilon(\omega, \mathcal{E}, \Gamma) \propto \frac{1}{(\hbar\omega)^2} \int_{\text{B.Z.}} d^3\mathbf{k} \int_0^\infty ds e^{-\Gamma s} \exp[i(\hbar\omega - E_{\text{CV}}(\mathbf{k}))s] \exp(-i(\hbar\Omega)^3 s^3/3). \quad (3.12)$$

In the case $\hbar\Omega \leq \Gamma/3$, a series expansion of the last exponential function of the form $e^x = 1 + x + \dots$ finally shows that the perturbed dielectric function can be expressed in the following form:

$$\epsilon(\omega, \mathcal{E}, \Gamma) \propto \epsilon(\omega, \mathcal{E} = 0, \Gamma) + \frac{1}{(\hbar\omega)^2} \int_{\text{B.Z.}} d^3\mathbf{k} \int_0^\infty ds e^{-\Gamma s} \times \exp[i(\hbar\omega - E_{\text{CV}}(\mathbf{k}))s] (-i(\hbar\Omega)^3 s^3/3). \quad (3.13)$$

Mathematically, the criterion $\hbar\Omega \leq \Gamma/3$ means that the broadening term cuts off the exponential function before higher-order terms of the series expansion come into play. This criterion plays a central role in modulation spectroscopy as it determines whether so-called low-field conditions actually apply for a measurement. The consequence of these higher-order terms are oscillatory contributions which will be discussed in the context of the intermediate field regime. The second term of the sum in eq. 3.13 is the change in the dielectric function $\Delta\epsilon$. This means that the perturbed dielectric function can be expressed as the sum of the unperturbed function and the change $\Delta\epsilon$.

Further mathematical simplifications show that – under the assumptions described above – the change in the dielectric function and hence the measured signal $\Delta f/f$ is related to the third derivative of the unperturbed dielectric function and can be written as

$$\Delta\epsilon(\omega, \mathcal{E}, \Gamma) \propto \frac{(\hbar\Omega)^3}{3(\hbar\omega)^2} \frac{\partial^3}{\partial(\hbar\omega)^3} ((\hbar\omega)^2 \epsilon(\omega, \Gamma)). \quad (3.14)$$

The proportionality to the third derivative of the unperturbed dielectric function is a distinct feature of the application of an electric field \mathcal{E} and the reduction of the translation symmetry of the crystal which is connected to it. The electric field \mathcal{E} represents a net force and accelerates electrons which leads to non-vertical transitions in $E_{\text{CV}}(\mathbf{k})$. Other modulation techniques such as stress or thermo-modulation directly influence the interband transition energy E_{CV} . A similar derivation as the one presented here leads to a change in the dielectric function which is connected to the first derivative of the unperturbed dielectric function. For completeness, it should be noted that in some cases, the application of an electric field can lead to first derivative terms [121]. This situation is typically found in quantum wells as the carriers are confined and cannot be accelerated freely.

In the following, the modifications of $\Delta\epsilon$ which come into play in case $\hbar\Omega \leq \Gamma/3$ is not valid anymore will be presented. This could be particularly important in solar cells since the p–n junction comprises a large electric field and it is not *a priori* clear which electric field regime the measurement of a modulated reflectance spectrum takes place in.

Intermediate Field Regime

In order to derive an expression for the imaginary part of the dielectric function in the presence of a static electric field the generalized Franz–Keldysh theory needs to be applied. The following derivation is based on a publication by Aspnes [122]. The starting point is an expression for ϵ_2 of the form

$$\epsilon_2(\omega, \mathcal{E}) \propto \frac{1}{(\hbar\omega)^2} \int_{\text{B.Z.}} d^3\mathbf{k} \int_{-\infty}^{\infty} ds \exp\left(i\hbar\omega s - i \int_{-s/2}^{s/2} ds' E_{\text{CV}}(\mathbf{k} - e\mathcal{E}s')\right). \quad (3.15)$$

The effect of the electric field \mathcal{E} is still to create contributions from non-vertical transitions in the band structure. For mathematical simplicity, lifetime broadening Γ is neglected here. The next step in the derivation is again to perform the Taylor series as shown in eq. 3.11. The integration over s' again yields a term of the order of s and a term of the order of s^3 . Using eq. 3.10 to express the electric field \mathcal{E} , ϵ_2 simplifies to

$$\epsilon_2(\omega, \mathcal{E}) \propto \frac{1}{(\hbar\omega)^2} \int_{\text{B.Z.}} d^3\mathbf{k} \int_{-\infty}^{\infty} ds \exp\left(i(\hbar\omega - E_{\text{CV}}(\mathbf{k}))s - i(\hbar\Omega)^3 s^3/3\right). \quad (3.16)$$

Since no lifetime term $e^{-\Gamma s}$ is cutting off contributions, the integral needs to be evaluated explicitly which is possible using the definition of the Airy function of the first kind $\text{Ai}(x)$ [123]:

$$\text{Ai}(x) = \int_{-\infty}^{\infty} ds \exp\left(\frac{i}{3}s^3 + ixs\right) \quad (3.17)$$

This finally yields an expression for the imaginary part of the dielectric function in the presence of an electric field \mathcal{E} :

$$\epsilon_2(\omega, \mathcal{E}) \propto \frac{1}{(\hbar\omega)^2} \int_{\text{B.Z.}} d^3\mathbf{k} \frac{1}{\hbar\Omega} \text{Ai}\left(\frac{E_{\text{CV}} - \hbar\omega}{\hbar\Omega}\right). \quad (3.18)$$

The physical meaning of the Airy function is again that electrons gain momentum in the applied electric field and interband transitions with $\Delta\mathbf{k} \neq 0$ become possible. For a vanishing electric field ($\hbar\Omega \rightarrow 0$) the Airy function is replaced by a δ -function and eq. 3.2 is obtained.

The consideration of lifetime broadening is also possible. However, the derivation of an expression for $\Delta\epsilon$ is rather lengthy and not relevant for the understanding of the basic physical mechanism of modulation spectroscopy. Instead, the expressions for $\Delta\epsilon(\omega)$ in the intermediate field regime will be given in the following. For this purpose it is convenient to define the electro-optic energy $\hbar\theta$ as

$$(\hbar\theta)^3 = 4(\hbar\Omega)^3. \quad (3.19)$$

Just like $\hbar\Omega$, the electro-optic energy determines the strength of the perturbation by the applied electric field. According to Batchelor *et al.* [124] an expression for the change in the dielectric function is given by:

$$\Delta\epsilon_1(\omega) = B\sqrt{\hbar\theta} \operatorname{Im} \left(\frac{H(z)}{(\hbar\omega - i\Gamma)^2} \right) \quad (3.20)$$

$$\Delta\epsilon_2(\omega) = B\sqrt{\hbar\theta} \operatorname{Re} \left(\frac{H(z)}{(\hbar\omega - i\Gamma)^2} \right) \quad (3.21)$$

where $H(z)$ denotes the electro-optic function [125] which is defined as

$$H(z) = \pi [\operatorname{Ai}'^2(z) - z\operatorname{Ai}^2(z) + i(\operatorname{Ai}'(z)\operatorname{Bi}'(z) - z\operatorname{Ai}(z)\operatorname{Bi}(z))] + i\sqrt{z}$$

with the Airy function of the first kind $\operatorname{Ai}(z)$ and of the second kind $\operatorname{Bi}(z)$ [123]. The dimensionless complex argument z is defined as

$$z = \left(\frac{E_g - \hbar\omega}{\hbar\theta} \right) + i \frac{\Gamma}{\hbar\theta}.$$

The imaginary part of z – the ratio of the broadening parameter Γ and the electro-optic energy $\hbar\theta$ – essentially determines whether low-field conditions are given or not. Figure 3.2 shows the change in the dielectric function $\Delta\epsilon$ for three different ratios $\Gamma/\hbar\theta$. For the highest ratio (a) low-field conditions are given and the change in the dielectric function is given by the third-derivative of the unperturbed dielectric function as derived above. This means in particular that the low-field limit is contained within the generalized Franz–Keldysh theory. For an increasing electric field (larger values of $\hbar\theta$) oscillations become first visible and then more pronounced at the high-energy side of the spectra (Fig. 3.2(b) and (c)). These oscillations are called Franz–Keldysh oscillations (FKOs) and their period relates to and hence allows the determination of the electro-optic energy [126].

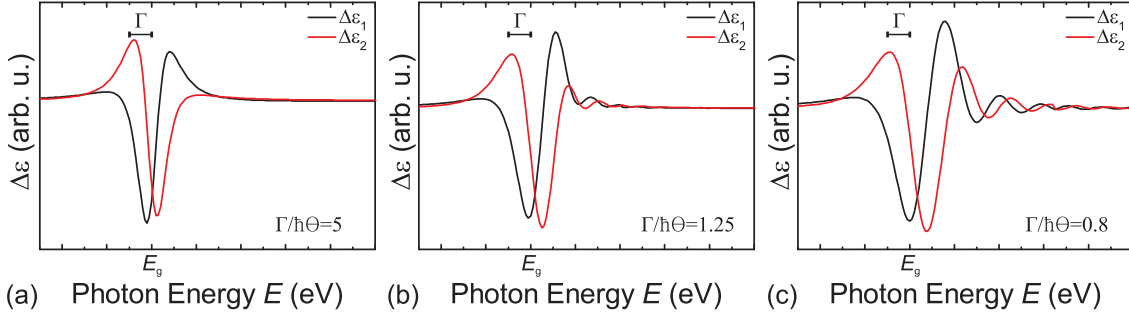


Figure 3.2: Calculated change in the real ($\Delta\epsilon_1$) and imaginary ($\Delta\epsilon_2$) part of the dielectric function according to Franz–Keldysh theory (using eqs. 3.20 & 3.21). (a) Under low-field conditions the change in ϵ is represented by the third derivative of the unperturbed dielectric function. For increasing electro-optic energies $\hbar\theta$ compared to the broadening parameter Γ pronounced Franz–Keldysh oscillations become visible above the band gap in (b) and (c). After [112].

3.1.4 Evaluation of Electroreflectance Spectra

In this subsection, the two main evaluation methods of modulated reflectance spectra will be presented – namely Aspnes’ Third Derivative Functional Form (TDFF) and the calculation of the so-called Modulus Spectrum based on a numerical Kramers–Kronig transformation. Both methods were used to evaluate the measured data sets in this work in order to check for consistence. The resulting values agreed within a few meV.

Aspnes’ Third Derivative Functional Form

Assuming that the measured signal $\Delta f/f$ is proportional to $\Delta\epsilon$ and applying the third derivative as derived in eq. 3.14 to a lifetime-broadened square-root shaped dielectric function (eq. 3.8) yields the well-known expression for $\Delta f/f$ after Aspnes [15] which is referred to as Aspnes’ Third Derivative Functional Form (TDFF)¹:

$$\frac{\Delta f}{f}(\hbar\omega) = \text{Re} \left(\frac{C e^{i\theta}}{(\hbar\omega - E_g + i\Gamma)^n} \right). \quad (3.22)$$

n determines the type of critical point and takes a value of $n = 2.5$ for a three-dimensional M_0 critical point. C is a slowly-varying function of the energy and is typically considered as a constant amplitude factor. It should be noted that in the low-field limit, the lineshape of the measured signal is invariant with respect to the electro-optic energy but the amplitude scales with \mathcal{E}^2 . The phase factor θ effectively

¹In most cases, $\Delta f/f$ refers to $\Delta R/R$.

mixes the changes in the real and imaginary part of the dielectric function $\Delta\epsilon_1$ and $\Delta\epsilon_2$. It is also a slowly-varying function of the energy and is considered as a constant over the energetic region of a resonance within this evaluation formalism.

A fit of expression 3.22 to a measured spectrum yields a set of parameters the most important ones being the energy E_g and the broadening Γ of the optical transition. The main advantage of this evaluation method is that no further assumptions have to be made about other parameters of the dielectric function. In the case of multiple optical transitions j in the signal, multiple TDFFs are summed up:

$$\frac{\Delta f}{f}(\hbar\omega) = \sum_j \operatorname{Re} \left(\frac{C_j e^{i\theta_j}}{(\hbar\omega - E_j + i\Gamma_j)^{n_j}} \right). \quad (3.23)$$

The individual terms are referred to as oscillators. As we will show later, there is the risk of using too many oscillators to fit a measured spectrum precisely instead of keeping an eye on the physics behind it. Distorted lineshapes may not fit exactly to a TDFF and an increase in the degrees of freedom produces an artifact which is then misinterpreted as a real optical transition. The reasons for lineshape distortions will be discussed in the next chapter.

Modulus Spectrum

Another evaluation method uses the fact that a modulated reflectance spectrum can be calculated from a causal function, this means $\Delta R/R$ or generally $\Delta f/f$ is proportional to $\Delta\epsilon$. This method was introduced by Hosea [127] and has the main advantage compared to Aspnes' TDFF that no assumptions about the type of critical point have to be made. The measurement signal as described in eq. 3.22 can be seen as the real part of a complex quantity. Since it is a function of $\Delta\epsilon$ – a causal function – the imaginary part of this quantity can be calculated by a Kramers–Kronig transformation. This operation can be performed numerically using a Fourier series approach [128].

By calculating the modulus of the complex modulated reflectance spectrum one obtains a peak structure the center of which determines the critical point energy – within this work the band gap E_g . It is important to note that this procedure can only be applied in the case of isolated resonances. Mathematically, this is due to the Kramers–Kronig transformation which leads to distortions due to interaction terms between resonances in close vicinity of each other.

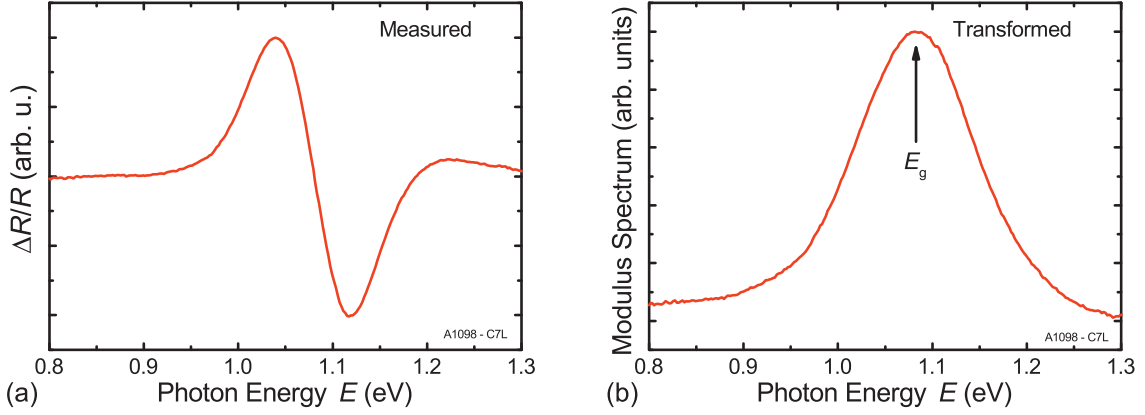


Figure 3.3: (a) Measured modulated reflectance spectrum of a CZTSSe thin-film solar cell. (b) The corresponding modulus spectrum shows a peak at the band gap E_g .

However, for isolated resonances (that means a separation of at least the linewidth Γ) the modulus spectrum $L(\omega)$ can be approximated as

$$L(\omega) \approx \sum_j \frac{C_j}{((\hbar\omega - E_j)^2 + \Gamma^2)^{n/2}} \quad (3.24)$$

with a set of peaks at the energetic position of the resonances E_j . Figure 3.3 shows the modulated reflectance spectrum of the energetic vicinity of the fundamental band gap of a solution-processed CZTSSe solar cell (a) which was measured in this work and the corresponding transformed spectrum (b). The band gap is determined by the center of the peak.

3.1.5 Electroreflectance Setup

In order to measure electroreflectance (ER) spectra a setup was designed within this work and improved during the Master's thesis of Christian Huber [112]. Figure 3.4(a) shows the electroreflectance setup which was used to acquire room temperature ER spectra. A detailed list of all parts of the optical setup as well as the data acquisition devices can be found in appendix A.

Light from a 250-W tungsten halogen lamp is dispersed in a 0.32 m focal-length monochromator with a 6001/mm grating. The divergent light is slightly focused using lens L_1 and reflected from mirror M_1 . A second lens L_2 is used to focus the light onto the sample so that a sharp image of the exit slit of the monochromator is

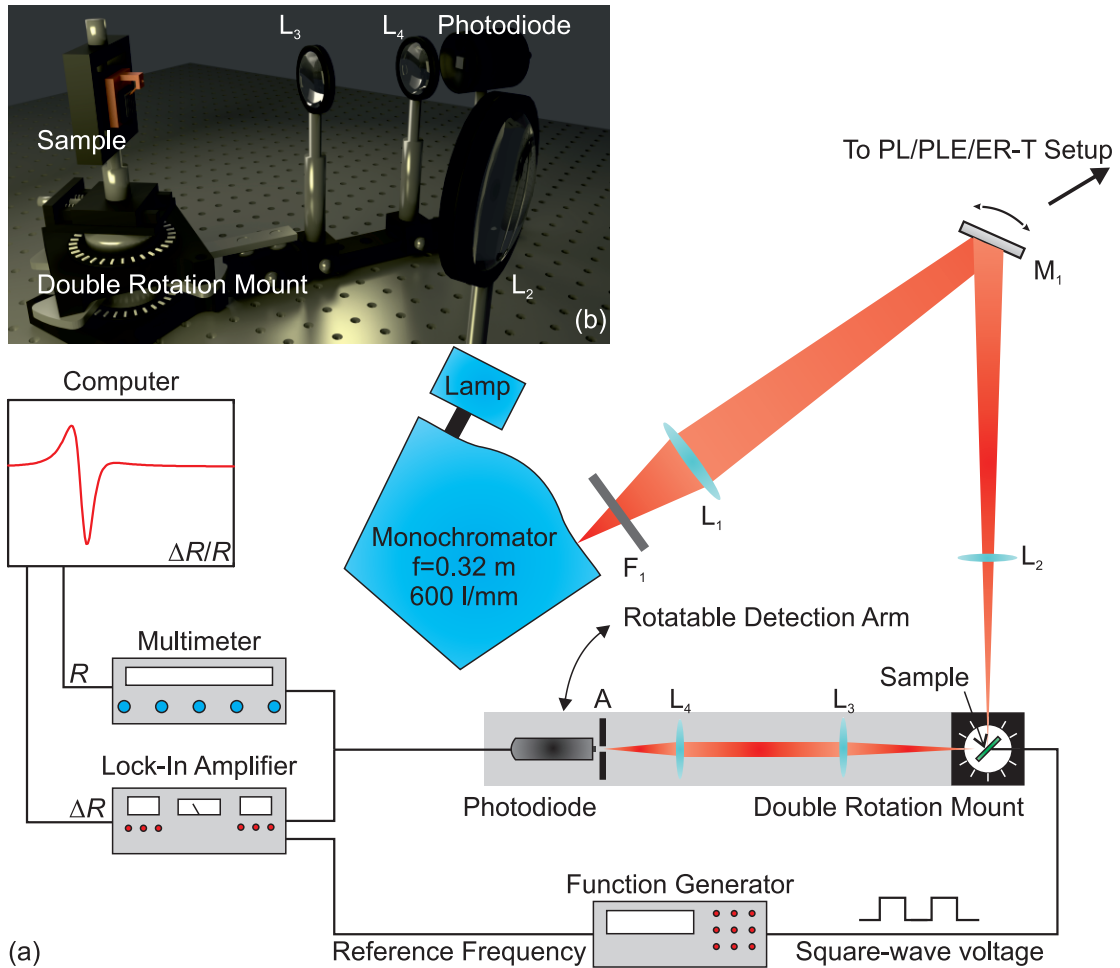


Figure 3.4: (a) Schematic of the ER setup used in this work. Monochromatic light is imaged onto the sample using a primary lens system (L_1 & L_2) and reflected/scattered light is collected using a secondary lens system (L_3 & L_4). To block higher diffraction orders, the incident light is filtered using F_1 . The secondary lens system as well as the sample are mounted on a double rotation mount so that the angle of incidence and angle of detection can be varied independently. A square-wave voltage is applied in reverse bias and a lock-in amplifier detects ΔR whereas a multimeter detects R . (b) Schematic of the detection lens system with the double rotation mount (Courtesy of Christian Huber).

visible on the sample. Furthermore, M_1 is used to precisely position the image on the sample. The sample is mounted on a copper sample holder which allows for electrical contacting by using a gold-coated tip which is pressed onto the window layer or, if available, the metal grid of the solar cell. The Mo back contact is electrically connected to the copper using silver conductive paint. A two-axis translation stage allows for a precise sample positioning in lateral direction. The sample holder is mounted on a double rotation mount which allows for a defined adjustment of the angle of incidence onto the sample. Using a third translation stage in axial direction the solar cell can be positioned exactly on the rotation axis of the double rotation mount.

Specularly or diffusely reflected light is collected using a second lens system (L_3 and L_4) and detected using an amplified InGaAs or Si photodiode, depending on the spectral region. An aperture (A) is used to block stray light. This part of the setup is mounted on a rail carrier system which is connected to the double rotation mount as shown in Fig. 3.4(b). This allows for an independent adjustment of the angle of incidence (AOI) and the angle of emergence (AOE). The role of the detection of diffusely or specularly reflected light will be discussed in chapters 4 and 5.

A square-wave voltage ($V_{pp} = 1.5 \text{ V}, V_{min} = 0 \text{ V}$ if not stated otherwise in appendix C) in reverse-bias is applied to the solar cell at a frequency of $f = 223 \text{ Hz}$. The reference frequency as well as the photodiode signal are fed into a lock-in amplifier which detects the AC part of the signal – proportional to the change in reflectance ΔR . The photodiode is further connected to a multimeter which detects the DC part of the signal – proportional to the average reflectance R of the solar cell. Both signals are acquired using a *LabVIEW* program and $\Delta R/R$ is calculated. The wavelength of the incident monochromatic light is scanned in energetically equidistant steps.

If necessary, temperature-dependent electroreflectance (ER-T) measurements can be performed as well. For this purpose, the sample is mounted in a helium bath cryostat and mirror M_1 is moved backwards to allow light to enter the photoluminescence spectroscopy setup shown in Fig. 3.5 later in this chapter. In the case of an ER-T measurement, L_{10} is used instead of L_2 to image the exit slit of the monochromator onto the sample. The chopper C_2 (used for PLE) is taken out of the beam.

Light reflected from the sample is then collected similarly to the secondary lens system in Fig. 3.4 with the exception that an aperture is used to observe an intermediate image of the sample and to block out-of-focus light. Details on the lens system can be found in subsection 3.2.2 and appendix A. Light is then focused into a 0.64 m focal-length monochromator with a 1501/mm grating which is scanned synchronously to the 0.32 m monochromator to suppress luminescence from the sample. Luminescence plays a role at low temperatures and a synchronous scan of the two

monochromators is necessary. Further details on the photoluminescence setup will be given in subsection 3.2.2. A mirror at the exit slit of the monochromator focuses the selected wavelength onto the photodiode which is again connected to a lock-in amplifier and a multimeter. The sample temperature T_S is adjusted by a software PID-controller which operates a resistive heater in the helium cryostat.

3.2 Photoluminescence Spectroscopy

3.2.1 Application of Photoluminescence Spectroscopy in this Work

Photoluminescence spectroscopy (PL) is a well-established technique to study radiative recombination processes in semiconductors. The technique is particularly useful to study defects that lie energetically close to the band gap as electrons tend to relax to the energetically lowest states. Since recombination is the complementary process of carrier excitation, PL is used as a complementary technique to ER on CZTSSe solar cells within this work.

Possible carrier recombination pathways are manifold and a review of standard mechanisms is given in, e.g., [129]. However, kesterites represent a highly defectious and compensated medium and some special observations are made in PL. First, the observed luminescence is very broad and asymmetric. Depending on the excitation power, additional contributions to the luminescence spectrum are observed – none of them as resolved peaks but shoulders on one side of the spectrum. In order to explain these findings, recombination models such as quasi-donor–acceptor pair recombination and fluctuating potential recombination have gained an increasing amount of attention in recent years [79, 130]. A comparison of the relevant theoretical models will be given in chapter 6 and individual contributions to the PL signal will be identified by comparison of the PL signal to the ER and photoluminescence excitation spectroscopy signal.

3.2.2 Photoluminescence Spectroscopy Setup

During this work the optical setup shown in Fig. 3.5 has been constructed. The intention behind it was to provide a platform for multiple optical measurements such as PL spectroscopy, photoluminescence excitation spectroscopy but also ER-T and Raman spectroscopy. This is why several optical paths are visible.

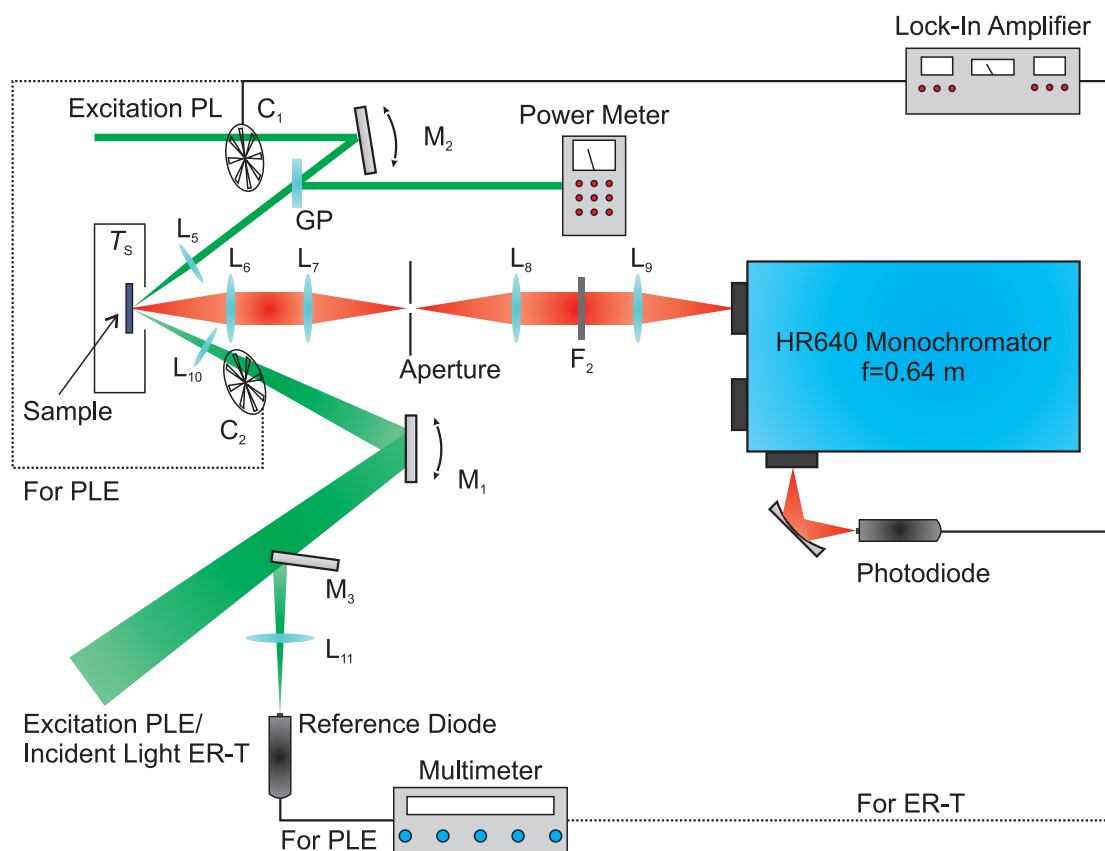


Figure 3.5: Optical setup for the measurement of temperature-dependent ER, PL and PLE spectra. Depending on the measurement, either small-bandwidth light from a halogen lamp dispersed in a monochromator or a laser is used as excitation.

The sample is either placed in a bath-cryostat or in front of it, depending on whether a low-temperature measurement is to be performed or not. There are several excitation sources available. For PL a high-power laser diode ($\lambda = 670$ nm) is used. The laser light is intensity-modulated using the mechanical chopper C_1 the reference frequency of which is fed into a lock-in amplifier. An adjustable mirror (M_2) allows for a precise positioning of the laser on the sample. The excitation light is then focused using lens L_5 which is mounted on a three-axis translation stage to adjust focus and position of the laser spot on the sample. Using a glass plate (GP), a fraction of the incident laser light is directed to a power meter to monitor the excitation power. Luminescence from the sample is collimated by lens L_6 and focused onto the aperture by lens L_7 . The aperture fulfills two purposes: it is used to verify the quality of the sample image and to reject out-of-focus light such as, e.g., laser reflections. The luminescence is again collimated using lens L_8 and laser light scattered from

the sample is blocked by a filter F_2 . The beam height is adjusted to the monochromator entrance slit using a periscope consisting of two silver mirrors (not shown in Fig. 3.5). Light is then focused into the $f = 0.64$ m monochromator using lens L_9 . This lens was chosen to match the numerical aperture (NA) of the monochromator in order to guarantee optimum illumination of the grating for maximum spectral resolution.

For PL measurements a 3001/mm grating was used. Due to broad PL features a large spectral region had to be recorded and gratings with a higher groove density often exhibit a strong decrease in diffraction efficiency in the infrared spectral region due to an inappropriate blaze angle. In order to suppress water vapor absorption, the monochromator was purged with nitrogen. Typical widths of the entrance and exit slit were 800 μm which corresponds to a spectral resolution² of 2 meV. The resolution has been verified not to be the limiting factor in PL spectra by recording spectra with smaller slit widths as well.

Luminescence is recorded using a liquid nitrogen-cooled amplified InGaAs photodiode which is connected to the lock-in amplifier in order to suppress unmodulated background light and detector noise. The monochromator wavelength is scanned in energetically equidistant steps. Monochromator movement, data acquisition as well as the cryostat temperature are controlled using *LabVIEW* programs.

The recorded samples are corrected for the detector response of the InGaAs diode. Further details on this can be found in appendix B. A more sophisticated correction using a calibrated halogen lamp was not performed due to the temporal instability of the lamp as well as the modified imaging conditions compared to a laser spot.

3.3 Photoluminescence Excitation Spectroscopy

3.3.1 Physical Mechanism of Photoluminescence Excitation Spectroscopy

In the case of thin-film solar cells it is not possible to measure the absorption spectrum directly due to the non-transparent Mo back contact although it would often be of highest interest. Even for thin films prepared on glass a transmission measurement will not yield the absorption but the extinction coefficient of the semiconductor. In the case of polycrystalline $\text{Cu}(\text{In,Ga})\text{Se}_2$ and $\text{Cu}_2\text{ZnSn}(\text{S,Se})_4$ absorbers this will certainly comprise contributions from scattering processes.

²Determined by the full width at half maximum of a Ne calibration lamp.

PLE is a powerful technique to shed light on the absorption and carrier relaxation processes in a semiconductor. For further reading on the basic principles of PLE the reader is referred to textbooks on semiconductor optics [117,131]. The main idea of this technique is to vary the excitation wavelength while observing the luminescence intensity of the sample at a fixed detection wavelength.

Since the exciting wavelength is smaller than the detection wavelength, generated carriers have to relax to the energetic level of the detection wavelength and recombine. After Yu [131] the intensity of the emission I_{em} at the detection wavelength is given by:

$$I_{\text{em}} = P_{\text{abs}}P_{\text{rel}}P_{\text{em}}I_{\text{exc}}, \quad (3.25)$$

where P_{abs} denotes the absorption probability which essentially correlates to the absorption coefficient at the excitation wavelength. P_{rel} denotes the probability of a relaxation towards the detection energy. Especially this term is a key factor in the observed spectra. In the case of potential and/or band gap fluctuations as they are likely to be found in kesterites this term plays an important role. At low temperatures, when carrier mobility is significantly lowered, it is not *a priori* clear whether all recombination energies will be accessible due to, e.g., carrier localization.

The emission probability P_{em} from the final state is assumed to be constant. Finally, the last factor which influences the emission intensity is the excitation intensity I_{exc} . Ideally, the excitation intensity is held constant. If this is not possible, it has to be verified that the luminescence spectrum exhibits an invariant lineshape for all excitation wavelengths to exclude nonlinear effects, e.g., due to state filling. If this is the case, the spectrum can be corrected for the varying excitation intensity as it was done in this work.

It has to be emphasized again at this point that a PLE spectrum is not generally identical with the absorption spectrum. In order to reach the energetic state of the detection wavelength, carriers have to relax. Only if this relaxation probability is constant for all detection wavelengths, the measured PLE signal is strongly correlated to the absorption spectrum.

3.3.2 Photoluminescence Excitation Spectroscopy Setup

The setup which was used to acquire PLE spectra is shown in Fig. 3.5 and was partly explained in subsection. 3.2.2. The main difference to a PL measurement is that the excitation wavelength λ_{exc} is scanned. This is why monochromatic light from the 0.32 m focal-length monochromator from the ER setup is used for sample excitation.

Mirror M_1 from the ER setup (Fig. 3.4) is moved backwards so that the exciting light can enter the PL setup (Fig. 3.5). The exciting light is chopped using C_2 and the corresponding reference frequency is fed into the lock-in amplifier. Light is focused onto the sample using L_{10} . The detection is completely analogous to a PL measurement with the exception that the detection monochromator is set to a fixed wavelength and the slits are opened further in order to obtain a stronger signal. A typical slit width of the detection monochromator was 2 mm which corresponds to a bandwidth³ of 5 meV with a 3001/mm grating.

Since it is of vital importance that nonlinear excitation effects are excluded, PL spectra with several different λ_{exc} are acquired and their shape is verified to be invariant. During the PLE measurement a small fraction of the exciting light is branched off using mirror M_3 and focused onto an InGaAs reference diode using L_{11} . The reference diode voltage is acquired using a computer-controlled multimeter and the recorded PLE signal is corrected for the intensity variation of the excitation light. The corresponding correction curves are shown in appendix B.

For the measurement itself the sample is placed within the cryostat and is set to a defined temperature T_S . The excitation wavelength is then scanned in energetically equidistant steps.

3.4 Summary

The presented spectroscopy techniques are all well-established in semiconductor physics and have been used for decades. However, chalcogenide thin-film solar cells represent a challenging task for all three methods. Especially highly defectious materials such as kesterites exhibit several peculiarities when it comes to radiative recombination. The importance of this work is that the materials were studied with complementary techniques to investigate both absorption and emission properties. Furthermore, an identification of the individual contributions is only possible by comparing PL and PLE spectra which has been done within this work. This is one aspect which underlines the significance of this work.

A central aspect of this work is the further development of modulation spectroscopy and the application of this technique to thin-film solar cells. In the derivation of the lineshapes presented in section 3.1 but also for data evaluation of modulated reflectance spectra several assumptions were made. In this work, it was investigated whether all these assumptions are justified for thin-film solar cells based on CIGS and CZTSSe.

³Determined by the full width at half maximum of a Ne calibration lamp.

First, Aspnes' derivation [15] assumes a low and homogeneous electric field as a perturbation and – and at least in its basic form – implicitly it also assumes a single semiconductor surface the reflectivity of which is only governed by $\epsilon(\omega)$. In contrast to that, thin-film solar cells represent a layered system with a contrast in the refractive index of each layer. Furthermore, a strong built-in electric field can deviate from the usually assumed low-field conditions and a spectrum evaluation using a TDFF fit may not be justified.

These circumstances are investigated in more detail within the next chapter and the applicability of TDFF and modulus spectrum analysis of measured spectra is examined.

Chapter 4

Electroreflectance on Thin-Film Solar Cells

The possibility to perform measurements on entire solar cell devices to determine the band gap of the absorber layer is one of the main advantages of electroreflectance, compared to, e.g., transmission measurements. However, the use of standard evaluation methods for electroreflectance spectra relies on several assumptions concerning the physical system as presented in the previous chapter.

The aim of this chapter is to give an overview on the challenges of electroreflectance due to the complicated structure of thin-film solar cells. The influence of both the built-in electric field as well as thin-film interferences are analyzed using one-dimensional simulations based on the transfer matrix method (TMM).

Finally, the simulations are adjusted manually to fit a measured electroreflectance spectrum of a CIGS solar cell and to determine the fundamental band gap as well as the spin-orbit splitting Δ_{SO} of the absorber layer.

A large part of the results presented in this chapter were achieved in the Master's thesis of Christian Huber. A detailed discussion of the topic – especially on the implementation of the TMM simulation – can be found in [112]. Furthermore, the results were published in [132].

4.1 Deviations from Ideal Measurement Conditions

A thin-film solar cell (TFSC) deviates from samples which were typically investigated using ER concerning several aspects. The derivation of the most important evaluation technique, Aspnes' Third Derivative Functional Form (eq. 3.22), makes several assumptions on the nature of the sample which do not necessarily hold for a TFSC. In this section, the main assumptions of low-field electroreflectance will be discussed and compared to a physically realistic situation for an ER measurement on a TFSC. The results of one-dimensional optical simulations will be shown in the following sections.

One of the most important assumptions in the derivation of eq. 3.14 and eq. 3.22 which has to be verified is $\hbar\theta/\sqrt[3]{4} \leq \Gamma/3$ – namely, the applied perturbation takes place in the low-field regime. However, in order to separate charge carriers efficiently, a TFSC comprises a p–n junction with a built-in electric field \mathcal{E}_{int} . The application of an AC voltage in reverse bias – as it is done in ER measurements – increases the electric field amplitude \mathcal{E} within the space-charge region (SCR). This means, that the measured spectrum $\Delta R/R$ actually corresponds to

$$\frac{\Delta R}{R}_{\text{measured}} \propto \frac{R(\hbar\theta_1) - R(\hbar\theta_2)}{R(\hbar\theta_1) + R(\hbar\theta_2)} \quad (4.1)$$

where $\hbar\theta_1$ and $\hbar\theta_2$ denote the electro-optic energies corresponding to the extreme values of the electric field during measurement \mathcal{E}_{int} and $\mathcal{E}_{\text{int}} + \mathcal{E}_{\text{ext}}$. This means that both the built-in electric field of the p–n junction as well as the externally applied electric field \mathcal{E}_{ext} influence the observed lineshape. It remains to investigate whether this lineshape shows a TDFFF behavior or whether the measurement takes place in the intermediate field regime and consequently, $\Delta\epsilon$ must be described according to eqs. 3.20 & 3.21. In case further influences are present, it would even be possible that neither of the two lineshapes is able to capture the measured signal accurately.

Another aspect of the built-in electric field is that the derivation of the TDFFF presented in [15] assumes the presence of a homogeneous electric field \mathcal{E} as perturbation. In a TFSC – as well as in every p–n junction – the built-in electric field decays over the length d_{SCR} of the SCR within the absorber and therefore represents an inhomogeneous perturbation. In the Schottky approximation the decay length mainly depends on the charge carrier concentration and the static dielectric constant ϵ_r of the material. In both CZTSSe and CIGS the doping level depends on the concentration of V_{Cu} and therefore on the chemical composition. Thus, the length of the SCR in the absorber as well as the maximum built-in electric field $\mathcal{E}_{\text{int,max}}$ will be a function of the latter. It should be mentioned that in the past ER measurements were

already performed using p–n junctions or Schottky barriers. As will be discussed, this is not a problem as long the measurements take place in the low-field regime. The, the influence of the presence of a strong applied inhomogeneous electric field and the built-in electric field will be investigated in section 4.3.

A different factor which influences the lineshape of measured ER spectra are thin-film interferences. An important assumption in the derivation of eq. 3.14 is that the reflectivity of the sample is a sole function of $\epsilon(\omega)$. A TFSC consists of several layers q with a thickness in the order of the wavelength of light (see Fig. 2.6). Furthermore, there is a strong contrast in the refractive indices $\tilde{n}_q(\omega)$ of the individual layers. These two factors lead to thin-film interferences which can be observed in the reflectance spectrum of a TFSC. More importantly, a modulation of the dielectric function $\epsilon(\omega)$ (and hence $\tilde{n}(\omega)$) leads to a modulation of the interference conditions for thin-film interferences due to a change in the optical layer thickness nd . This leads to features in modulated reflectance spectra which are due to thin-film interferences and not the critical point which is to be detected. The influence of interferences on electroreflectance spectra will be discussed in section 4.4.

The main problem concerning the evaluation of electroreflectance spectra of a TFSC is that lineshape distortions due to the above-named factors can easily be mistaken for contributions from real optical transitions. One is tempted to fit the resulting spectrum by increasing the number of TDFD oscillators thus producing evaluation artifacts which in turn can be misinterpreted as, e.g., an energetic splitting of one into two interband transitions.

4.2 One-Dimensional Simulation of Electroreflectance Spectra

In order to investigate the effects of the different factors discussed in the previous section, one-dimensional simulations based on the TMM were performed. In this formalism, the amplitudes of the electric field propagating into and out of the solar cell layer stack are represented by a two-component vector. An interface between two materials i and j of different refractive indices is represented by a 2×2 matrix M_{ij}^I . The same holds for the propagation of light within a medium j . The respective matrix will be referred to as M_j^P . The interface and propagation matrices are given by [133]

$$M_{ij}^I = \frac{1}{t_{ij}} \begin{pmatrix} 1 & r_{ij} \\ r_{ij} & 1 \end{pmatrix} \quad M_j^P = \begin{pmatrix} e^{-ik\tilde{n}_j d_j} & 1 \\ 1 & e^{ik\tilde{n}_j d_j} \end{pmatrix} \quad (4.2)$$

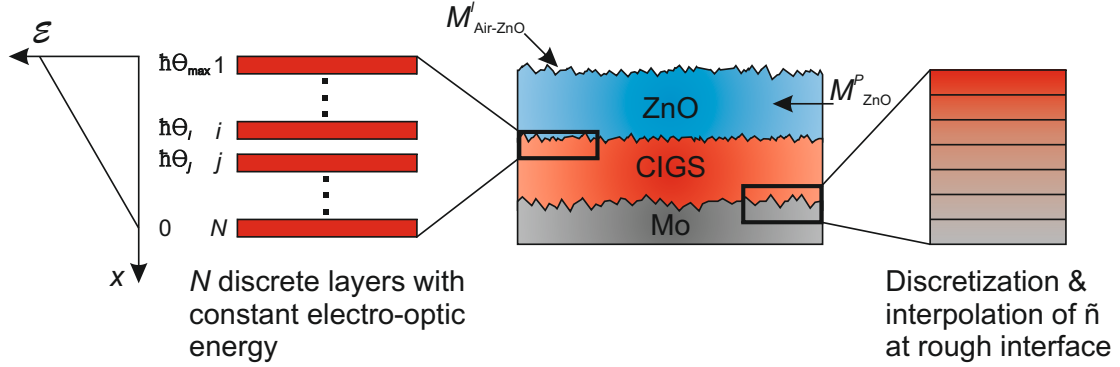


Figure 4.1: Schematic principle of the 1D simulations. The reflectivity of the layer stack is calculated using the TMM with interface matrices M^I_{ij} and propagation matrices M^P_j . The electric field in the p–n junction is implemented by discretizing the SCR into N layers of constant electro-optic energy $\hbar\theta$ (left). Rough interfaces are considered phenomenologically by dividing the transition regions into discrete layers and interpolating the refractive index of the parent materials linearly (right).

where t_{ij} and r_{ij} denote the transmission and reflection coefficients which are determined by the Fresnel equations. d_j and \tilde{n}_j are the thickness and the complex refractive index of layer j .

The propagation of light through a N -layer stack is characterized by the product of the 2×2 matrices of the individual layers [132].

$$M_{\text{stack}} = M_{01}^I M_1^P M_{12}^I M_2^P \dots M_N^P M_{N+1}^I = \begin{pmatrix} T_{11} & T_{12} \\ T_{21} & T_{22} \end{pmatrix} \quad (4.3)$$

The reflectivity R of the layer stack is given by $|T_{21}/T_{11}|^2$. Using this formalism it is then possible to calculate the quantity of interest in electroreflectance – the normalized difference of the reflectivity of the system with and without an applied electric field \mathcal{E} .

For the refractive index of ZnO [134] and Mo [135] tabulated data is used. The dielectric function of the thin-film absorber layer is described using a Critical Point Parabolic Band (CPPB) oscillator [120] which was fitted to experimental data for CIGS given in [28]. The threefold nature of the valence band in both CIGS and CZTSSe is explicitly neglected since the main purpose of the simulation was to study the lineshape distortions for a single resonance which are caused by the built-in electric field and thin-film interferences. Despite the fact that the simulations were conceived for CIGS absorber TFSCs, the results are universal and the conclusions can be transferred to CZTSSe. The principle of the employed TMM simulations

is illustrated schematically in Fig. 4.1. The change in the dielectric function of the absorber layer $\Delta\epsilon$ due to the applied electric field is calculated using eq. 3.20 and eq. 3.21 and is added to the unperturbed dielectric function. In order to simulate the inhomogeneous electric field, the SCR within the absorber is discretized and each section is attributed a constant electro-optic energy $\hbar\theta$ [124]. A linear decay of the electric field within the absorber is assumed (Schottky approximation). This results in a spatial profile $\hbar\theta(x)$ which is determined by $\hbar\theta_{\max}$ and a decay length d_{SCR} according to eq. 3.10 and eq. 3.19. To achieve numerical stability, the electro-optic function $H(z)$ which is part of eqs. 3.20 and 3.21 is partly approximated as [126]:

$$H(z) \approx \frac{i}{32} z^{-5/2} - \frac{i}{4z} \exp\left(i\frac{4}{3}z^{3/2}\right) \quad (4.4)$$

To determine whether or not this approximation is used or the full electro-optic function is evaluated, a slightly modified criterion as the one described by Hall *et al.* [112, 136] is used. Due to the one-dimensional nature of the simulation, surface and interface roughness cannot be described accurately. Yet, in order to account for this phenomenologically, rough interfaces were replaced by a set of thin sublayers with an interpolated value for the refractive index as it is shown on the right-hand side of Fig. 4.1.

The modulated reflectance spectrum is then determined by calculating the reflectivity of the layer stack R with and without an applied electric field and the normalized difference in reflectivity $\Delta R/R$.

It has to be emphasized that this is only a one-dimensional approximation of a truly three-dimensional problem. Furthermore, the CdS buffer layer is omitted since its thickness is smaller than the assumed interface roughness between the absorber and the window layer. Additionally, CdS is transparent in the spectral region of interest ($E_g = 2.4 \text{ eV}$ [137]). Furthermore, no reliable refractive index data for CBD-CdS was available. Still, the main idea is to study the distortions of a single resonance in the presence of a built-in electric field and thin-film interferences, separately.

4.3 Influence of the Electric Field on Electroreflectance Spectra

As already discussed in section 4.1, the measured signal in electroreflectance is the normalized difference of the reflectivity R of the layer stack at two different electro-optic energies $\hbar\theta_1$ and $\hbar\theta_2$. This means that both the built-in electric field as well as the externally applied electric field have to be considered. In the TMM simulations

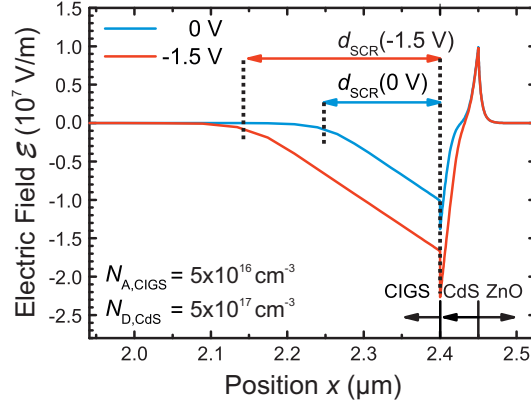


Figure 4.2: Simulation of the electric field $\mathcal{E}(x)$ within the SCR of a CIGS TFSC for an assumed acceptor density of $N_A = 5 \times 10^{16} \text{ cm}^{-3}$ in the absorber layer with and without an applied reverse bias of -1.5 V . For both configurations the electric field decays linearly over the largest part of the SCR justifying the use of the Schottky approximation within the TMM simulations. Furthermore, the width of the SCR is extended by the bias voltage. After [132].

this is achieved by the implementation of a linear decay of the electric field in the absorber. In order to determine appropriate values for the decay length d_{SCR} and the amplitude of the electric field with and without reverse bias, one-dimensional simulations using *SCAPS* [138] were performed.

4.3.1 The Electric Field in the Space-Charge Region

In order to simulate the band alignment in the SCR, a slightly modified version of the basic *SCAPS* model for a CIGS solar cell was used. Figure 4.2 depicts the spatial decay of the electric field in the SCR of a TFSC with and without a reverse bias voltage of -1.5 V . d_{SCR} denotes the decay length of the electric field within the absorber layer and not the depletion width of the entire SCR w . d_{SCR} is extended by the reverse bias voltage and the amplitude of the electric field \mathcal{E}_{max} is increased. Over a large part of the SCR the decay of the electric field can be considered as linear which corresponds to the physical situation in the Schottky approximation. Such a decay is also assumed in the TMM simulations.

However, the physical situation differs from the assumptions made in the derivation of the TDFE lineshape [15]. The built-in electric field represents a spatially inhomogeneous perturbation which varies in its decay length for the two extreme voltages which are applied during measurement. Aspnes and Frova pointed out that an in-

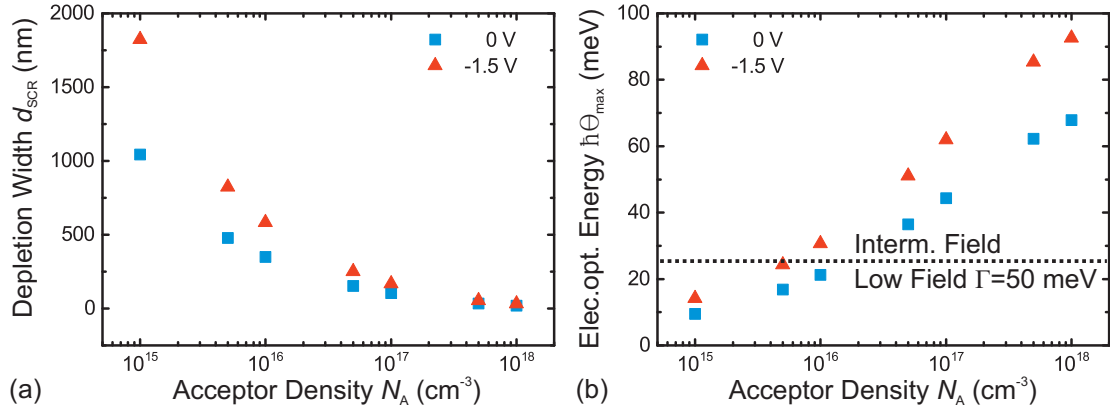


Figure 4.3: (a) Simulated width of the SCR within the CIGS layer with and without applied reverse bias for typical doping densities of the absorber layer. (b) Resulting maximum electro-optic energy $\hbar\theta_{\text{max}}$ for the same variation of the absorber doping density. The assumption of low-field conditions may not generally be justified, depending on the broadening Γ of the dielectric resonance.

homogeneous field can be treated as an effective homogeneous perturbation with a different amplitude [139]. This will be given more attention in the next subsection.

In order to estimate the electric field regime which electroreflectance measurements of TFSCs take place in, the acceptor density N_A and thus the charge carrier concentration in the CIGS layer was systematically varied in the electrical simulations. The decay length d_{SCR} depends strongly on the assumed doping density in the CIGS absorber layer as shown in Fig. 4.3(a). In the case of low doping densities in the order of 10^{15} cm^{-3} , the SCR extends over almost the entire absorber layer (thickness $t_{\text{CIGS}} = 2.4 \mu\text{m}$) for a reverse bias voltage of $V = -1.5 \text{ V}$ and it is almost doubled compared to the built-in SCR.

The second relevant quantity to describe the perturbation within the absorber layer is the maximum electro-optic energy at the buffer-absorber interface $\hbar\theta_{\text{max}}$. The corresponding values are shown in Fig. 4.3(b). Depending on the broadening parameter Γ of the fundamental band gap resonance in $\epsilon(\omega)$, low-field conditions as described in the previous chapter cannot be assumed and the appearance of FKOs could be expected. Furthermore, the lineshapes can be distorted when considering the measured signal $\Delta R/R$ in eq. 4.1. Typically observed widths of the measured ER lineshapes were in the order of 0.05-0.08 eV which would serve as an upper bound for Γ . The resulting upper limit of the low-field regime is also shown Fig. 4.3(b). As it will be discussed in chapter 5, inhomogeneous broadening is also observed in the ER spectra of TFSCs which is why the observed width of the ER spectrum only serves

as an upper bound for Γ . Therefore, Fig. 4.3(b) underlines that ER measurements on TFSCs are likely to occur in the transition region between the low-field and the intermediate field regime. This circumstance will be discussed in subsection 4.3.2

The electrical simulations were performed assuming CIGS as absorber layer material due to the availability of reliable material data. The physical properties of CZTSSe are not known in such detail so far. What is considered as certain is a lower static dielectric permittivity in the range of $\epsilon_r = 6.7 - 8.5$ depending on the sulfur content y [45, 140] compared to a value for CIGS of $\epsilon_r = 13.6$ [141] as it was assumed in the electrical simulations. In the Schottky approximation the depletion width w is given by

$$w = \sqrt{\frac{2\epsilon_0\epsilon_r}{e} \frac{N_A + N_D}{N_A N_D} V_D} \propto d_{\text{SCR}} \quad (4.5)$$

with the diffusion voltage V_D . Assuming the same values for N_A , N_D and V_D as in CIGS, the ratio of the decay lengths of the electric field d_{SCR} within the absorber for CIGS and CZTSSe is given by

$$\frac{d_{\text{CZTSSe}}}{d_{\text{CIGS}}} = \sqrt{\frac{\epsilon_{\text{CZTSSe}}}{\epsilon_{\text{CIGS}}}} \approx 0.7 - 0.8$$

depending on whether sulfide or a selenide kesterite is considered. Analogous reasoning yields a ratio of the maximum amplitude of the electric field of

$$\frac{\mathcal{E}_{\text{CZTSSe}}}{\mathcal{E}_{\text{CIGS}}} \propto \frac{\epsilon_{\text{CIGS}}}{\epsilon_{\text{CZTSSe}}}.$$

This means that the electric field within CZTSSe is decaying faster but with a steeper slope and starting at a higher value compared to CIGS. For electroreflectance measurements the electro-optic energy is the relevant quantity and as it was shown in eq. 3.10 the reduced mass in the direction of the field plays an important role as well. In order to estimate the ratio of the electro-optic energies in both materials the average effective masses from DFT calculations were considered [45] to obtain values for the reduced masses. Based on these very simple estimations the electro-optic energy is increased up to a factor of 1.5 for CZTSe (1.4 for CZTS) compared to CIGS:

$$\frac{\hbar\theta_{\text{CZTSSe}}}{\hbar\theta_{\text{CIGS}}} = \sqrt[3]{\frac{\epsilon_{\text{CIGS}}^2}{\epsilon_{\text{CZTSSe}}^2} \frac{\mu_{\text{CIGS}}}{\mu_{\text{CZTSSe}}}} \approx 1.4 - 1.5 \quad (4.6)$$

This means that deviations from low-field conditions in electroreflectance may be present in CZTSSe for lower carrier concentrations already.

Still, the simulations showed that the linear decay of the electric field within the SCR of the absorber layer was a realistic assumption for the TMM simulations. In

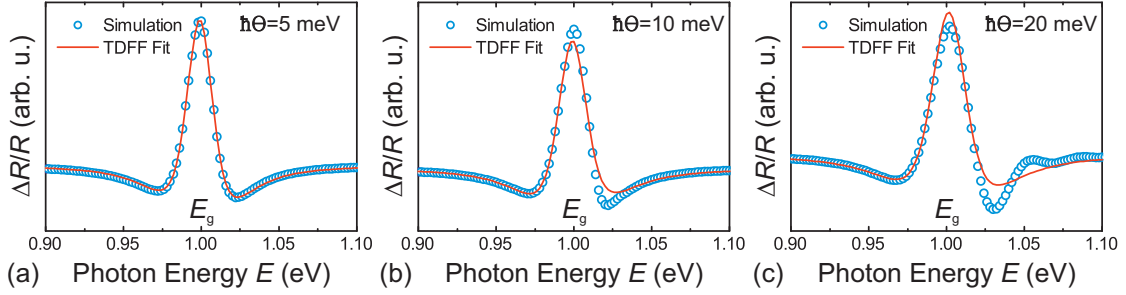


Figure 4.4: Simulated ER spectra for a fixed oscillator position of $E_g = 1$ eV, a fixed decay length d_{SCR} , and a broadening of $\Gamma = 0.02$ eV. (a) For $\hbar\theta = 5$ meV the lineshape is perfectly captured by a TDFE. (b) For $\hbar\theta = 10$ meV slight deviations on the high-energy side of the spectrum become visible. (c) For $\hbar\theta = \Gamma$ FKOs are clearly visible and the TDFE fit deviates clearly from the simulated lineshape. However, for all three situations the resulting band gap is well-captured by the fit within a range of 4 meV. After [112,132]

the following, the influence of the electric fields on the distortion of ER spectra will be investigated in terms of both a built-in electric field and electric field amplitudes corresponding to intermediate field conditions.

4.3.2 Electroreflectance with a Strong & Spatially Inhomogeneous Perturbation

In order to study the role of the electric field in terms of both inhomogeneity and field strength, TMM simulations of a CIGS half space for different electro-optic energies were performed. The ambient medium was assumed to be air ($\tilde{n}_{\text{air}} = 1$). Fig. 4.4 shows the resulting ER spectra for three different ratios $\hbar\theta/\Gamma$ for a fixed broadening of the resonance $\Gamma = 0.02$ eV and a band gap energy of $E_g = 1$ eV. A decay length within the absorber d_{SCR} of 150 nm was assumed. In this simulation no built-in electric field was assumed.

A TDFE fit captures the lineshape of the low-field simulation in Fig. 4.4(a) very well justifying the use of the laminar simulation approach for an inhomogeneous electric field. Furthermore, it shows that a linearly decaying inhomogeneous electric field does not represent a general problem for the application of a TDFE analysis. Interestingly, the TDFE fits for higher electro-optic energies in Fig. 4.4(b) and (c) result in band gap values which agree with the simulated values within 4 meV, despite the fact that the lineshape is not captured very well anymore. Deviations of the fit from the simulated spectrum arise on the high-energy side of the spectrum which is due to the appearance of FKOs. It should be noted that the broadening parameter

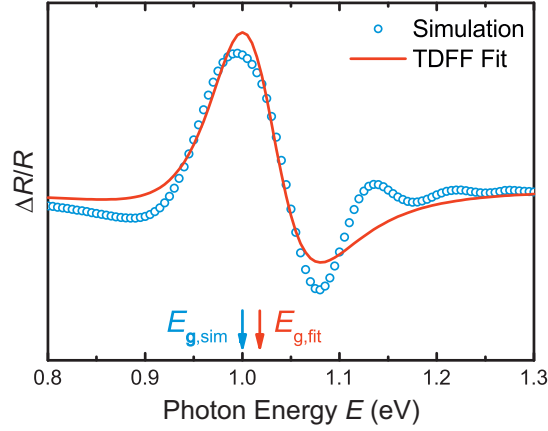


Figure 4.5: Simulated ER spectrum for a CIGS/air half space for a realistic and a changing decay of the electric field depending on the applied voltage and realistic electro-optic energies $\hbar\theta_1$ and $\hbar\theta_2$ assuming an acceptor density $N_A = 5 \times 10^{16} \text{ cm}^{-3}$ in the absorber layer. The assumed parameters for the oscillator were $E_g = 1 \text{ eV}$ and $\Gamma = 0.05 \text{ eV}$. The TDFE fit value of E_g deviates by 18 meV from the simulated value. After [112, 132].

is not well-determined by the fit for higher electro-optic energies compared to the simulations which is also a consequence of the FKOs on the high-energy side of the spectrum. The fit only yields the precise value of the broadening parameter for the low-field spectrum as shown in Fig. 4.4(a).

In real measurements however, besides the above-mentioned strong electric field the decay length d_{SCR} also varies depending on the applied bias voltage as it was shown in the previous subsection. Figure 4.5 shows a simulated ER spectrum for an electrically realistic situation assuming an acceptor density of $N_A = 5 \times 10^{16} \text{ cm}^{-3}$ in the absorber layer and an applied reverse bias of $V = -1.5 \text{ V}$. The respective values for d_{SCR} and $\hbar\theta$ were taken from the electrical simulations of the previous subsection. The physical difference to the previous simulation is the presence of a built-in electric field. During measurement, the SCR is extended from 150 nm to 250 nm due to the bias voltage.

Furthermore, the electro-optic energy of the built-in electric field is $\hbar\theta_1 = 36 \text{ meV}$ and it is increased to $\hbar\theta_2 = 51 \text{ meV}$ by the bias voltage. This is explicitly considered in the simulation. The oscillator broadening parameter was chosen as $\Gamma_1 = 0.05 \text{ eV}$ and the band gap was set to $E_g = 1 \text{ eV}$.

It is clearly visible that the TDFE fit is not able to capture the lineshape of the simulated spectrum properly and the resulting band gap value $E_{g,\text{fit}}$ deviates by 18 meV from the value of the simulation. The appearance of FKOs as evident from Fig. 4.5 can be seen as an indicator that low-field conditions do not apply. For lower

doping densities of the absorber layer – or in general lower electro-optic energies – further simulations have shown that a TDFE fit captures the resulting spectrum better and the band gap is determined correctly. The main reason for the deviations is the existence of the built-in electric field. The magnitude of these deviations is dependent on the amplitude of the maximum electric field and thus the doping density in the absorber layer.

In summary, one can state that the built-in electric field is one of the key factors which distort electroreflectance spectra of TFSCs. Especially in highly doped absorber layers as it could be found in, e.g., very Cu-poor CIGS, low-field conditions are not fulfilled and a strong built-in electric field is present. In this case, a TDFE analysis of measured ER spectra yields band gap values which clearly deviate from the real value. Experimentally, the appearance of FKOs on the high-energy side of the ER spectra indicates deviations from low-field conditions. It should be mentioned that the latter could be washed out due to inhomogeneous broadening.

It should be emphasized, that the TMM simulation assumed a single optical transition at the band gap. Despite this circumstance the resulting ER spectra cannot be captured properly by a single TDFE fit. An increase of the number of oscillators would certainly allow to correct the lineshape deviations but it would introduce an artifact which will inevitably be misinterpreted as a contribution from a real optical transition.

4.4 Interference Effects in Electroreflectance Spectra

After the discussion of the influence of the built-in electric field of a TFSC on ER spectra the role of the individual functional layers in the formation of the ER signal will be discussed. In particular, the ZnO window layer and the partly reflective Mo back contact will be investigated in the following.

The reason why interferences play a role in ER spectra is physically simple. The mechanism of modulation spectroscopy is a variation of the dielectric function $\epsilon(\omega)$ of a material and thus the refractive index in the energetic vicinity of resonances in $\epsilon(\omega)$. If a dielectric layer stack exhibits an interference pattern in its reflectivity, it is due to refractive index contrasts between the individual layers and layer thicknesses in the order of the wavelength of light. An applied perturbation now periodically modulates the resonance condition of the interferences in the energetic vicinity of resonances in the dielectric function of the individual layers. This modulation can either be due to a modified effective layer thickness nd_j of an individual layer j or a

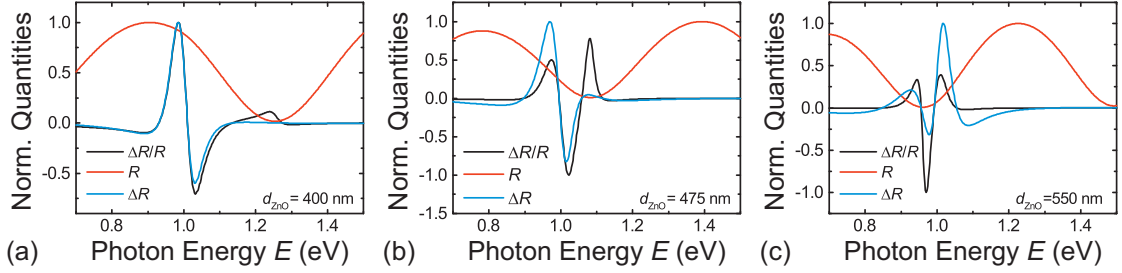


Figure 4.6: Simulated ER spectra for a CIGS/air half space with an intermediate ZnO layer of increasing thickness d_{ZnO} . The interference minimum in R is responsible for a distortion in the measured signal $\Delta R/R$. (a) In the case of a minimum in R energetically far away from the critical point, the lineshape still resembles that of a TDFE function. (b) and (c) For reflection minima in the energetic vicinity of the band gap the lineshapes of both ΔR and $\Delta R/R$ are strongly distorted. Further zero-crossings are visible which can be misinterpreted as additional optical transitions. After [112,132].

change in the reflection/transmission coefficient r_{ij}/t_{ij} between two adjacent layers i and j .

4.4.1 Influence of the ZnO Window Layer

Typical thicknesses of the ZnO window layer lie in the range of 300–500 nm. For simplicity of the simulations, the window layer will be considered as a homogeneous layer whereas in reality a combination of a thin intrinsic ZnO layer is followed by a doped ZnO:Al layer [61]. The main reason why $\Delta R/R$ is measured instead of ΔR is that this results in a self-referenced measurement and it is assumed that ΔR and R scale proportionally to each other so that detector responses and the spectrum of the used light source cancel out. This is certainly true for a spectrally flat reflectivity of a bulk semiconductor. However, with the thickness of the ZnO window layer being in the order of the wavelength of light, thin-film interferences are visible in the reflection spectrum of a TFSC.

Figure 4.6 shows simulated ER spectra for an increasing thickness of the window layer. In Fig. 4.6(a) the interference minimum in R is energetically well-separated from the band gap ($E_g = 1$ eV). The signal ΔR and $\Delta R/R$ are not distorted and a TDFE fit yields the correct band gap. For the simulations a broadening of $\Gamma = 0.05$ eV was assumed. The electro-optic energies $\hbar\theta_{1,2}$ and the decay lengths $d_{\text{SCR},1,2}$ were chosen for an assumed acceptor density of $N_A = 10^{15}$ cm $^{-3}$ in the absorber using the results of the electrical simulations. This corresponds to low-field conditions.

For an increasing ZnO thickness the interference minimum in R is shifted towards the resonance of the critical point as evident from Fig. 4.6(b) and (c). More importantly, ΔR and consequently $\Delta R/R$ are strongly distorted in the region of the critical point. The main visible effect is an increased number of zero-crossings compared to a regular TDFE. Again, such a spectrum cannot be fitted with a single TDFE function although only one single optical transition (with valid low-field conditions) is present. Analogously to the previous section, an increase in the number of oscillators to fit the spectrum would lead to the false interpretation that multiple optical transitions were involved in the signal.

Furthermore, the results show that the reflectivity R and the change in reflectivity ΔR are not scaling proportionally to each other in the vicinity of interference minima in R . Instead, this circumstance leads to a distortion of the ER spectra which can easily be misinterpreted. The consideration of a CIGS/air half space with an intermediate window layer is realistic for the energetic region above the band gap and the vicinity of it. Below the band gap the absorber layer is essentially transparent and its finite width needs to be considered. This will be discussed in the following.

4.4.2 Influence of the Mo Back Contact

Additionally to the finite absorber width, the partly reflective Mo back-contact acts as a mirror which amplifies interferences compared to a transparent substrate. Figure 4.7 shows a TMM simulation for a ZnO/CIGS/Mo layer stack with a rough interface between Mo and CIGS (implemented phenomenologically by mixing of refractive indices). E_g was again assumed to be 1 eV and the broadening parameter to be $\Gamma = 0.04$ eV. An electro-optic energy of $\hbar\theta = 0.01$ eV and a decay length $d_{\text{SCR}} = 200$ nm were chosen for simplicity and correspond to low-field conditions. The built-in electric field is neglected in this simulation.

Interference fringes below E_g are visible in all three signals and have the same periodicity. The implemented roughness essentially broadens the interferences in the modulated reflectance spectrum and is necessary to prevent poles due to the division by $R = 0$ in the simulations. It can be seen that an extremum in R corresponds to an inflection point in $\Delta R/R$. The high-frequency oscillation is damped in the energetic region of the band gap but still distorts the resonance as it is visible from the shoulder at around 0.97 eV. Above the band gap the interference fringes caused by the entire layer stack is damped due to absorption in the CIGS layer.

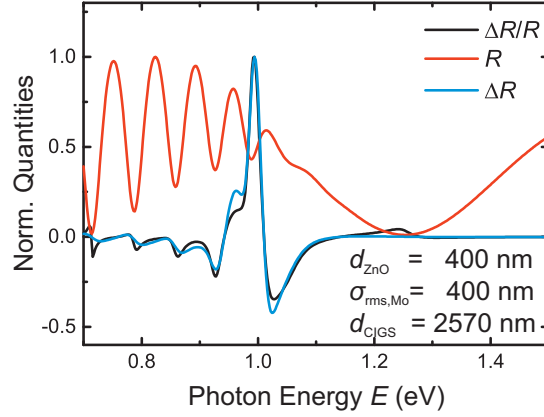


Figure 4.7: Simulation of a layer stack ZnO/CIGS/Mo with a rough CIGS/Mo interface (implemented by mixing of refractive indices). Below the assumed band gap of $E_g = 1$ eV, R shows interference fringes with a high frequency due to the combined layer thickness of ZnO and CIGS. The oscillations are damped for E approaching E_g . Above E_g the frequency of the oscillation is smaller due to the interference arising mainly from the ZnO layer. $\Delta R/R$ shows interference fringes with the same period as R below E_g . Above E_g the signal is distorted around the interference minimum. After [112, 132].

As already shown in the previous section, the remaining interference fringes above E_g are caused mainly by the ZnO layer. However, since the minimum of the ZnO interference is well-separated from the band gap there is only a slight distortion of $\Delta R/R$ at around 1.25 eV (compare Fig. 4.6(a)).

In summary, one can say that interferences play the second important role in the distortion of electroreflectance spectra of TFSCs compared to theoretical expectations. Especially in the energetic vicinity of interference minima in R , $\Delta R/R$ is strongly distorted and it has to be verified in the experiment that the measurement does not take place under such conditions. Interference fringes far below E_g are easy to identify due to the regular pattern. However, in the energetic region around the band gap, interferences distort the measurement signal strongly and it seems natural at first to increase the degrees of freedom by introducing additional optical transitions to fit the measured lineshape precisely.

When it comes to real ER spectra, both interference and electric field effects are present and have to be considered if one is to extract critical points such as the band gap or higher optical transitions. In the following, a manual adjustment of the TMM simulations to a measured spectrum of a CIGS TFSC is performed.

4.5 Experiment and Simulation: Determination of the Band Gap of Cu(In,Ga)Se₂

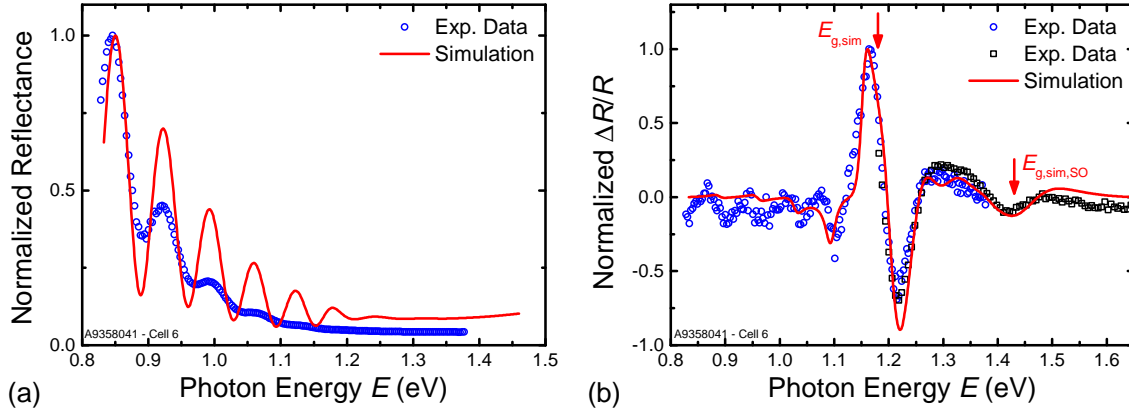


Figure 4.8: Adjustment of the TMM simulation to a measured ER spectrum. (a) Layer thicknesses are adjusted so that reflectance extrema coincide. (b) The energetic position of the fundamental band gap is determined to be $E_{g,sim} = 1.18$ eV. The second contribution is attributed to the split-off VB transition at $E_{g,sim,SO} = 1.43$ eV. The high-energy side of the spectrum was measured using Si photodiode (black squares), the low energy side was measured using an InGaAs photodiode (blue circles). Taken from [132] and formatted.

4.5 Experiment and Simulation: Determination of the Band Gap of Cu(In,Ga)Se₂

In the previous sections, several properties of TFSCs were discussed which influence or distort the lineshape of measured ER spectra. In order to exclude artifacts due to an increased amount of oscillators in a TDFE fit, the TMM simulation was adjusted to manually fit a measured spectrum recorded from a CIGS solar cell. The TFSC had a GGI gradient starting at $x = 0.23$ at the surface to a depth of about 500 nm. Then a parabolic increase to $x = 0.35$ is present at the back side of the device. The ER spectrum was recorded at an angle of incidence and an angle of detection of 20° . Both a Si and an InGaAs detector were used to cover a larger spectral range in the measurement.

Figure 4.8(a) shows the manual fit for the reflectance signal R . The measured signal R was corrected for the system response using a gold mirror as a reference. The layer thicknesses were then adjusted to yield matching reflectance extrema in both simulation and measurement. An actual capture of the measured lineshape was not possible. This is attributed to the phenomenological implementation of surface and interface roughness of the TFSC. Furthermore, the CdS layer was again omitted for the reasons already discussed in section 4.2.

Table 4.1: Resulting parameters of a manual fit to a measured spectrum of a CIGS solar cell. For both transitions an extension of the SCR within the absorber layer from 100 nm (withouth electric field) to 150 nm (with electric field) was assumed.

| Oscillator | E (eV) | Γ (meV) | $\hbar\theta_{\text{high}}$ (meV) | $\hbar\theta_{\text{low}}$ (meV) |
|-----------------------|----------|----------------|-----------------------------------|----------------------------------|
| $E_{\text{g,sim}}$ | 1.18 | 46 | 40 | 25 |
| $E_{\text{g,sim,SO}}$ | 1.43 | 110 | 40 | 25 |

However, the resulting thicknesses of the layers agree well with the thickness of the individual layers as determined by a secondary neutral mass spectrometry (SNMS) measurement.

Figure 4.8(b) shows the corresponding fit for the modulated reflectance signal. The oscillator position of the fundamental band gap was determined to be $E_{\text{g,sim}} = 1.18$ eV and the corresponding broadening parameter to be $\Gamma = 46$ meV. As expected, the position of the interference fringes in simulation and experiment match well. Deviations in the amplitudes of the fringes are probably due to the phenomenological implementation of roughness in the TMM model.

A second structure in the measured modulated reflectance signal arises at around 1.43 eV. This could not be captured by using only one optical transition in the simulation. Hence a second optical transition at 1.43 eV was introduced to capture the lineshape correctly. We note that this transition is energetically clearly separated from the fundamental band gap by 0.25 eV which is much larger than the broadening parameter of the fundamental resonance. The first transition at 1.18 eV is attributed to an effective oscillator consisting of the two topmost VB–CB transitions which cannot be resolved individually. The second optical transition is due to the third VB–CB transition which is energetically well-separated from the two uppermost VB–CB transitions by spin–orbit splitting. The energetic value for the split-off VB transition at $E_{\text{g,sim,SO}} = 1.43$ eV agrees well with results in literature, which have been determined by ellipsometry [52, 53, 142]. The reported values for the fundamental transition at $E_{\text{g,sim}} = 1.18$ eV are slightly lower than the determined value. However, the sample which was investigated within this work was very copper-poor ($[\text{Cu}]/[\text{Group III}] = 0.82$) and as already discussed the Cu-content also influences the band gap (as discussed in subsection 2.1.2). The results in this work thus reinforce the findings that a decrease in the Cu-content increases the fundamental band gap in CIGS as reported by Han *et al.* [57].

The resulting set of parameters for this manual fit is summarized in Table 4.1. The decay length of the electric field in the absorber was assumed to be 150 nm with

and 100 nm without applied electric field. It has to be emphasized that the use of two oscillators to fit the measured spectrum is justified since the two resonances are energetically well-separated. Furthermore, these results were obtained by calculating the modulated reflectance spectrum for the layer stack and not by a fit procedure involving multiple TDFFs.

4.6 Electroreflectance on Thin-Film Solar Cells in Literature

For CIGS thin films and single crystals several modulation spectroscopy studies were published. Chichibu *et al.* investigated excitonic effects using photorefectance spectroscopy on single crystals, thin films and epitaxial layers of the CIGS parent compounds CuInSe_2 and CuGaSe_2 . As already discussed in subsection 2.1.2, Shay *et al.* investigated the band structure of I–III–VI₂ semiconductor samples such as CIGS single crystals using electroreflectance and determined crystal field and spin–orbit splittings as well as the very low thermal dependence of the band gap of CuInSe_2 . What is common to all these reports is that the modulated reflectance spectra exhibited isolated and spectrally narrow resonances which makes an evaluation using multiple TDFFs possible.

In recent years, there were several reports on electroreflectance measurements on entire TFSCs. Theoropoulou *et al.* performed ER on Cu(In,Ga)S_2 solar cells with varying gallium content x in the absorber layers [143]. To evaluate the spectra, the energetic region of the fundamental band gap was fitted using up to 4 TDFFs for comparatively featureless ER spectra. The measured spectrum and the corresponding fit is shown in Fig. 4.9.

The individual oscillators were then attributed to two sets of fundamental band gaps and split-off VB oscillators corresponding to regions in the absorber layer with different Ga content. It is rather questionable why a statistical distribution of Ga and In atoms in the lattice should yield two sets of discrete oscillators instead of a single set of broadened effective oscillators.

The only explanation which might lead to such a conclusion might be an in-depth band gap gradient. However, an ER signal from a critical point can only arise if both a modulation of the built-in potential and a reflection are present at a certain position at the same time. There are two positions in the absorber at which a pronounced reflection can occur – the buffer–absorber interface and the back contact.

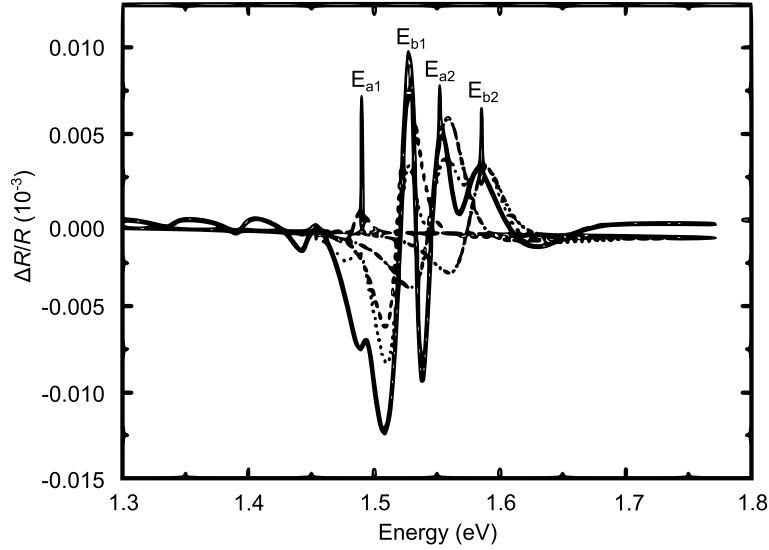


Figure 4.9: Electroreflectance spectrum of a $\text{Cu}(\text{In}_{0.96}\text{Ga}_{0.04})\text{S}_2$ solar cell with the corresponding fit using 4 TDFFs after [143]. The spectrum clearly shows interference fringes which extend into the signal at the fundamental band gap. Taken from [143] and formatted.

A modulation of the built-in electric field however, only occurs at the p-n junction which excludes signals from the back contact. A significant modulation caused by, e.g., a Schottky contact at the back side of the device would lead to very bad J - V characteristics of the device.

In the context of this chapter and this work, it is likely that the work of Theodoropoulou *et al.* suffers from an overinterpretation of the measured ER spectrum due to interference phenomena. The measured spectra in [143] (shown in Fig. 4.9) show clear signs of thin-film interferences below the band gap. As it was shown in section 4.4 of this chapter, thin-film interferences with different origins can lead to artifacts in the measured ER spectrum which can in turn be mistaken for real optical transitions.

Kiowski *et al.* also performed ER measurements on 4 $\text{Cu}(\text{In,Ga})\text{Se}_2$ solar cells with different Ga contents and a graded band gap CIGS sample [144]. Band structure analysis on the absorber layer as well as the buffer/window layer was then performed for measurements under different angles of incidence. Again, multiple TDFFs were used to fit the different spectral regions and for some samples up to 4 oscillators were assumed to fit the energetic region of the fundamental band gap of the absorber layer. Furthermore, a parabolic background is subtracted in order to yield a good capture

of the measured lineshape, which is hard to motivate physically, since the main advantage of modulation spectroscopy is exactly the suppression of other features than critical points. Furthermore, this represents an additional increase in the degrees of freedom. What is more likely is that the measured spectra are distorted by the effects which were discussed in this chapter. This will be shown explicitly and discussed in the next chapter as ER measurements on the same samples were performed.

In order to interpret ER spectra of TFSCs correctly, it is important to consider both the modulated reflectance and the reflectance signal. In case an interference minimum in R is in the vicinity of the fundamental band gap, the measured modulated reflectance spectrum is very likely to be distorted. Considering the findings of this chapter, a general procedure of determining the band gap of the absorber layer of a TFSC should be to reduce the number of oscillators – ideally to a single effective oscillator comprising all transitions at the fundamental band gap. Instead of trying to capture the measured lineshape perfectly only the main features such as the maximum oscillation and the steep slope should be attempted to be captured by a TDFF fit to estimate the band gap of the absorber correctly.

A manual fit using the presented TMM simulation is a second possibility to distinguish real optical transitions from artifacts produced by the built-in electric field or interferences. The main advantage is that it incorporates all the effects discussed within this chapter. Furthermore, it incorporates the correct physical description of intermediate electric fields as a perturbation. The TDFF case is incorporated as well for low electro-optic energies. However, the model comprises further degrees of freedom and it is necessary to obtain information on the layer thicknesses in order to check whether the resulting parameters from the simulation are consistent with the real solar cell.

4.7 Summary

In this chapter, the peculiarities of the investigation of TFSCs using electroreflectance were analyzed in detail. Using TMM simulations it has been shown that both the built-in electric field in a solar cell and thin-film interferences can strongly distort the measured signal compared to a theoretically expected ER spectrum.

The electric field and hence $\hbar\theta$ within the absorber layer highly depends on the value of the acceptor density N_A . For moderate acceptor densities in the order of 10^{15} cm^{-3} up to low values in the order of 10^{16} cm^{-3} the built-in electric field is not distorting the modulated reflectance lineshape strongly. A TDFF evaluation of the measured signal yields a correct value for the critical point energy within an error

of a few meV in the absence of interference distortions. However, starting at doping densities of around $N_A = 5 \times 10^{16} \text{ cm}^{-3}$, $\Delta R/R$ is distorted increasingly and the deviations from the TDFE fit value for E_g and the real value increase as discussed in section 4.3.

Furthermore, thin-film interferences play the second important role in the distortion of ER lineshapes. In the energetic region of reflection minima further lineshape distortions occur which can even lead to additional zero-crossings in $\Delta R/R$ as it was shown in section 4.4. Furthermore, the partly reflective Mo back contact acts as a mirror for photon energies below the fundamental band gap.

The gist of this chapter is that there are two main influences which distort a measured electromodulated reflectance spectrum. The resulting lineshapes cannot be fitted with a single TDFE function. Mathematically, a superposition of multiple closely spaced oscillators allows for an almost perfect capture of a measured spectrum. However, this holds the risk of an overestimation of the number of optical transitions involved.

To the best knowledge of the author, this is the first time that TMM simulations were performed to simulate ER spectra of TFSCs with their characteristic layers. In particular, this approach allowed for a detailed study of the influence of the built-in electric field and thin-film interferences separately.

In conclusion, ER is a technique which is challenged by artifacts when it comes to determining the band gap of the absorber of a TFSC – or generally critical points in the band structure of the materials in the layer stack. A large part of these problems is caused by the layered nature of the investigated samples – namely interferences. In the following chapter, it will be shown how to get rid of or at least how to reduce these artifacts dramatically by not only considering the specular reflectance R_S but also the diffuse reflectance R_D .

Chapter 5

Electromodulated Diffuse Reflectance

In the previous chapter, it was shown that both the built-in electric field and the layer structure of a TFSC represent non-ideal measurement conditions for ER. Both factors lead to distortions of the lineshape of a measured signal compared to the one expected for a single optical transition. The distortions can in turn be misinterpreted and mistaken for contributions originating from additional optical transitions. Especially features due to thin-film interferences can lead to additional zero-crossings of the signal $\Delta R/R$. A correct interpretation of specular ER spectra requires the knowledge of a lot of properties of the sample itself and makes thus the broad applicability of ER in the case of TFSCs very challenging.

In this chapter, modulated diffuse reflectance spectra are investigated as a way to reduce thin-film interferences drastically. First, it will be shown that the signature of a modulation of the dielectric function $\Delta\epsilon(\omega)$ cannot only be detected in the specular reflection R_S but also in the diffuse reflection R_D from a rough surface. This will be shown by means of two-dimensional finite-difference time-domain (FDTD) simulations.

After that, a CZTSe sample series with identical absorber thicknesses but with three different window layer thicknesses will be investigated. In specular ER measurements the samples show very different spectra and the data cannot be fitted by TDFFs comprising the same parameters for the absorber band gap. The measurement of diffuse ER yields almost identical spectra for all samples and in turn consistent absorber band gaps for all three window layer thicknesses as it would be expected.

Futhermore, as an application example, the absorber band gaps of a series of CIGS solar cells with different gallium contents x are determined. The findings of this chapter show that diffuse ER can actually be used as a characterization technique to determine the absorber band gap of a TFSC. In contrast to specular ER, the measured spectra can be evaluated without a detailed knowledge of, e.g., the thicknesses of the individual functional layers as it was discussed in the previous chapter.

Finally, the role of inhomogeneous broadening of the band gap and its impact on ER spectra are discussed. It will be shown that this is not limiting the applicability of ER to TFSCs and that it is still possible to determine the average value of a spatially fluctuating band gap.

As an introduction to the topic the morphology of a TFSC will be discussed briefly in the following since it is the basis for ER measurements in diffuse reflection. Parts of the results of this chapter were achieved in the Master's thesis of Christian Huber [112].

5.1 Layer Morphology of Thin-Film Solar Cells

A major drawback of the TMM simulations presented in the previous chapter is their one-dimensionality and thus the phenomenological implementation of the layer roughness which cannot be used to obtain information about diffuse reflection processes. A scanning electron microscopy (SEM) image of the typical cross-section of a real CZTSSe solar cell is shown in Fig. 5.1. TFSCs typically comprise polycrystalline functional layers with grain sizes in the order of micrometer. A morphological peculiarity of the solution-based solar cell absorbers from ZSW [102, 146] – as they are investigated in chapters 6 & 7 – is a triple-layer structure in the CZTSSe film with different grain sizes the origin of which is not yet understood. CZTSSe absorbers which were prepared using other methods and CIGS absorbers are also polycrystalline, yet, the films are smoother and grain sizes can be as large as the entire absorber layer thickness.

Concerning ER, one of the most important aspects of the polycrystalline absorber layer is the pronounced appearance of a diffuse reflection R_D of light originating from the absorber layer. This means that light can also be detected at an angle of detection (AOD) which is different from the AOE of the specular reflection. The role of the diffuse reflection from a rough surface in modulation spectroscopy will be investigated in the following section.

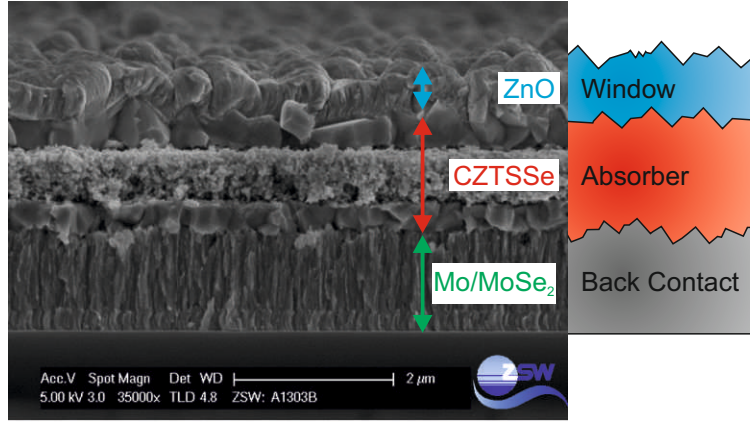


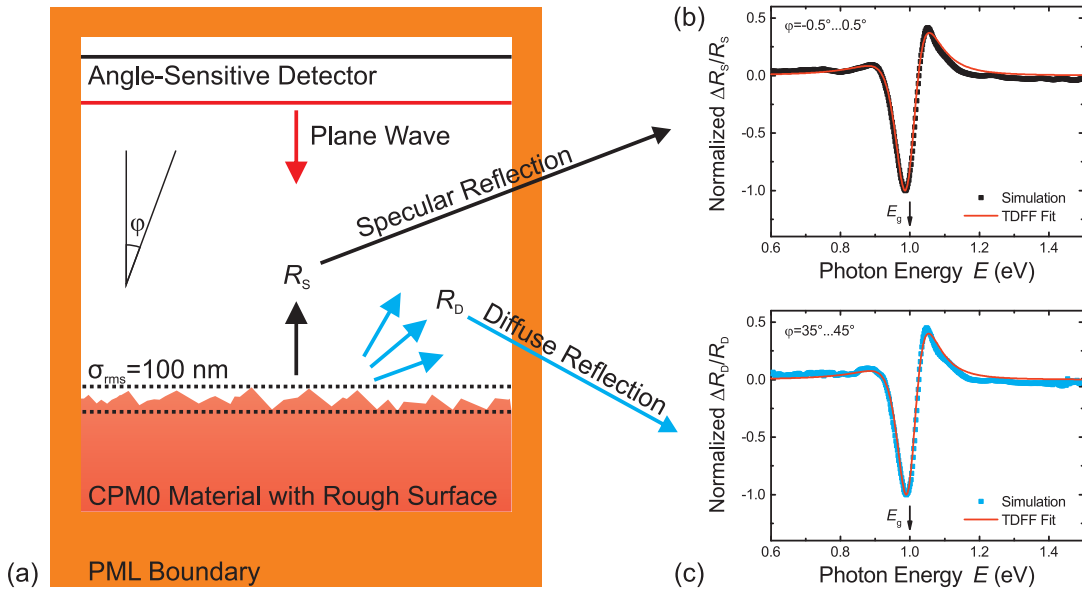
Figure 5.1: SEM cross-section image of a standard solution-processed CZTSSe solar cell (left) and schematic layer sequence with occurring interface roughness (right). The CdS buffer layer is not visible in this image. Solution-processed absorbers investigated in this work (ZSW) typically exhibit three CZTSSe layers of different morphology. Courtesy of ZSW.

5.2 Simulation of Modulated Diffuse Reflectance from a Rough Surface

In order to implement a more realistic model of a rough surface, two-dimensional FDTD simulations using the software package *Lumerical FDTD Solutions* were performed. For simplicity, perpendicular incidence of light ($\text{AOI} = 0^\circ$) was chosen.¹

Figure 5.2(a) schematically shows the implementation of the FDTD simulation. A CIGS half space with a roughness described by $\sigma_{\text{rms}} = 100 \text{ nm}$ is considered with an unmodulated dielectric function for a M_0 critical point (CPM0) after Adachi [147]. The band gap was chosen to be $E_g = 1 \text{ eV}$ and the broadening parameter to be $\Gamma = 0.06 \text{ eV}$. In order to obtain the modulated dielectric function, $\Delta\epsilon(\omega)$ is calculated according to eq. 3.20 and eq. 3.21 for an electro-optic energy of $\hbar\theta = 0.01 \text{ eV}$ and a value of $B = 2$. The parameters were chosen to be within the low-field limit of ER. Furthermore, $\Delta\epsilon$ was multiplied by a factor of 100 to yield a more pronounced change in reflectance in order to lessen the requirements on the simulation accuracy. It should be noted that the actual shape of $\Delta\epsilon$ is not relevant since the sole purpose of the simulation is a proof of principle that the signature of $\Delta\epsilon$ is also found in the change of the intensity of diffusely reflected light ΔR_D .

¹The simulation assumed a slab of $100 \mu\text{m}$ width and perfectly matched layers (PML) as boundary conditions.



The reflection of the surface is calculated for both the modulated and unmodulated case and an angle-sensitive detector records the reflected intensity depending on the AOE. Based on this data, the modulated specular reflectance spectrum $\Delta R_S/R_S(\omega)$ is calculated by adding up the resulting spectra for an AOE range of $\varphi = [-0.5^\circ, 0.5^\circ]$. The resulting spectrum can be seen in Fig. 5.2(b) and carries the signature of $\Delta\epsilon$. A TDFE fit to the simulation captures the lineshape almost perfectly and yields the parameters which were used within the simulations. This reproduces the findings of the TMM simulations for low-field conditions. The small deviations of the lineshape could be due to the scaled change in the dielectric function $\Delta\epsilon$ and thus contributions from terms of the order $(\Delta\epsilon)^2$ in eq. 3.6.

More importantly, the simulation allows to calculate the modulated diffuse reflectance spectrum $\Delta R_D/R_D(\omega)$. By adding up the resulting partial modulated reflectance spectra for an AOE ranging from $\varphi = 35^\circ$ to $\varphi = 45^\circ$ (assumed for a collection angle of 10°) the signature of $\Delta\epsilon(\omega)$ can be seen as well. This is evident from Fig. 5.2(c) and shows that the diffuse reflectance R_D also represents a function $f(\epsilon(\omega))$ as described in eq. 3.7 and can therefore be used for modulation spectroscopy measurements. This demonstrates that modulation spectroscopy is not limited to specular ER measurements but can be applied to any physical quantity f which depends on the dielectric function $\epsilon(\omega)$.

An interesting aspect of a diffuse reflectance measurement is that there is a defined AOI but no defined AOE since one is collecting light from multiple angles at once due to the numerical aperture of the detection lens system. This means that no strict thin-film interference condition can be formulated and interference fringes may be reduced.

5.3 Electroreflectance Measurements in Diffuse Reflection

In order to investigate the evolution of the ER signal depending on the AOI and the AOD a sample series with three different ZnO:Al thicknesses was investigated. All three samples were fabricated at the University of Luxembourg. The CZTSe absorber layers were all fabricated in the same run of a coevaporation process as described in [104]. After CdS and i-ZnO (80 nm) deposition the samples were coated with three different thicknesses of ZnO:Al (180, 280, and 380 nm).

Figure 5.3 shows ER spectra of the three samples with different window layer thicknesses for measurements in specular reflection. It is not possible to fit the individual

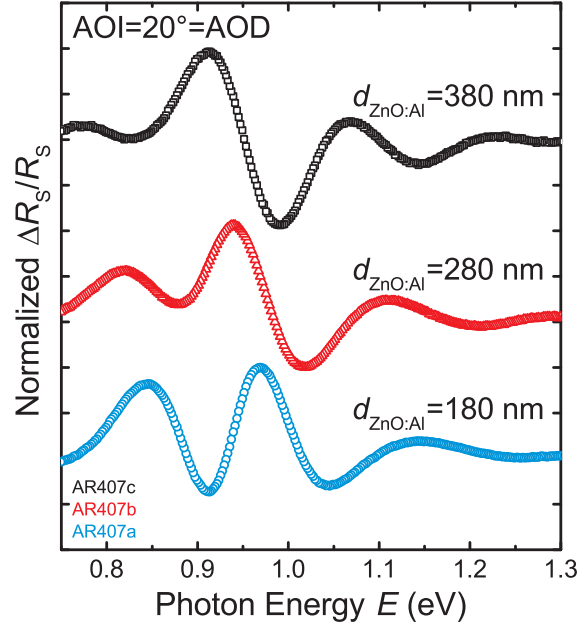


Figure 5.3: ER spectra of three CZTSe solar cell with different thicknesses $d_{\text{ZnO:Al}}$ of the ZnO:Al layer in specular reflection geometry. None of the spectra can be fitted by a single TDFE function and the shape of the measured spectrum changes strongly depending on $d_{\text{ZnO:Al}}$. Furthermore, fits involving multiple TDFEs do not result in identical oscillator positions for the three samples. After [112, 145].

spectra with a single TDFE and a fit involving multiple TDFEs yields different parameters for the single oscillators depending on which sample is investigated. This is not a physically meaningful result since the absorber layers of the individual cells were produced in the same coevaporation run and should therefore exhibit the same or at least very similar band gaps. The explanation for this finding is the influence of thin-film interferences on the modulated reflectance spectrum due to the different window layer thicknesses as it was discussed in section 4.4.

The samples were then gradually rotated from specular reflection to diffuse reflection using the double rotation mount setup described in Fig. 3.4. Figure 5.4(a) shows the evolution of the ER signal under sample rotation. The sample is rotated so that backscattered light is detected as evident from the definition of AOI and AOD in Fig. 5.4(b). Interestingly, similar spectra emerge independently of the sample which excludes lineshape distortions due to different ZnO:Al thicknesses and thus interferences as evident from Fig. 5.4(c). All spectra can be fitted by a single TDFE function and an average value for the band gap with its respective standard deviation can be determined:

$$\bar{E}_g = 0.880 \pm 0.005 \text{ eV} .$$

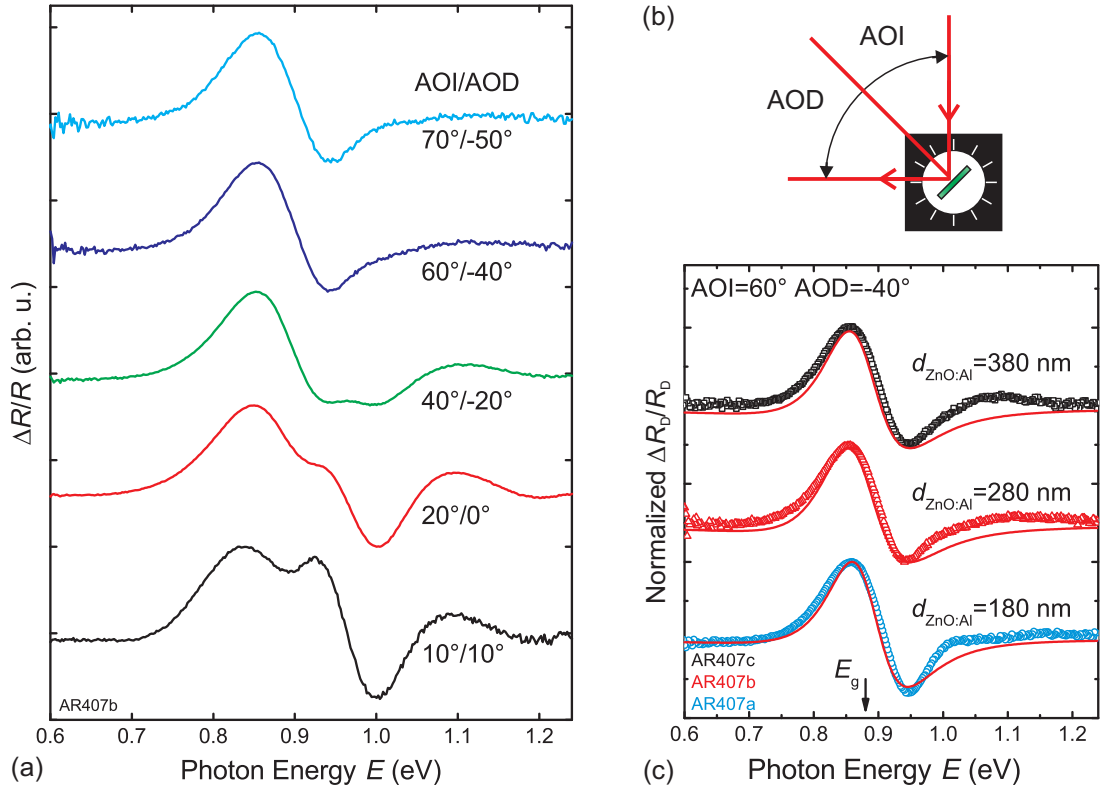


Figure 5.4: (a) Evolution of the modulated reflectance spectrum from specular reflection (black, bottom) to diffuse reflection (cyan, top). The signal changes drastically and converges to a lineshape resembling a single TDFF function. (b) Definition of positive direction for AOI and AOD. (c) ER spectra for all samples with different ZnO:Al thickness in diffuse reflection geometry and example TDFF fit (red solid line). The TDFF fits yield identical band gaps for all samples within measurement accuracy. After [145].

One has to consider that the samples comprise a pure $\text{Cu}_2\text{ZnSnSe}_4$ absorber and the fabrication involved a rapid cool-down after the absorber fabrication. As will be discussed in chapter 7 this thermal treatment has a strong and lowering impact on the band gap of the absorber which explains the low band gap value of 0.88 eV compared to typical literature values of around 1 eV [45]. The measurement of an electromodulated diffuse reflectance spectrum thus allows to reduce the influence of thin-film interferences drastically and turned out to be a universal method throughout this work. In the following, the term ER will always refer to measurements in diffuse reflection $\Delta R_D/R_D$. Measurements in specular reflection will be mentioned explicitly.

Still, deviations from an ideal TDFFF lineshape can be seen in Fig. 5.4(c) (red solid lines) which suggests that there are still other distorting influences than interferences. The diffuse ER measurement does not allow the exclusion of signal distortions due to the built-in electric field of the TFSC as discussed in section 4.3. In the context of electric field distortions of ER spectra, the most relevant physical property of the absorber is the acceptor density N_A and thus the carrier concentration. For CIGS typical carrier concentrations are in the range of $10^{15} - 10^{16} \text{ cm}^{-3}$ as determined by drive-level capacitance profiling (DLCP) [148]. The same orders of magnitude for the carrier concentration are found in kesterite solar cells [105, 140]. These carrier concentrations result in estimated electro-optic energies that are still within the low-field limit of ER but close to the intermediate field regime.

Consequently, distortions of the measurement signal due to the built-in electric field can be expected as discussed in section 4.3. However, no FKOs are visible in the measured spectra in Fig. 5.4(c) which suggests that the electric fields are comparatively low. Consequently, corresponding TMM simulations showed that a TDFFF analysis still determines the band gap within an uncertainty of around 10 meV despite the fact that the curve might not capture the measured lineshape perfectly. These results demonstrate the broad applicability of ER for the analysis of thin-film solar cell absorbers.

5.4 Gallium-Content-Dependent Band Gap of CIGS

The band gap of the absorber layer is one of the most important properties of a TFSC. As discussed in subsection 2.1.2, the band gap of CIGS can be tuned continuously from around 1 eV to 1.6 eV by varying the $[\text{Ga}]/([\text{Ga}]+[\text{In}])$ ratio (GGI). ER offers the possibility to determine the absorber band gap without destroying the sample and without the necessity of a certain sample preparation. However, it has been shown in this work that the recorded spectra have to be analyzed carefully in order to prevent evaluation artifacts.

Kiowski *et al.* performed specular ER measurements on a series of CIGS TFSCs with a varying GGI [144]. Critical points of the absorber band structure were determined using up to four TDFFFs and a parabolic background. This means that the number of degrees of freedom of each fit (a TDFFF comprises four parameters) was between 15 and 19, depending on whether three or four TDFFFs were used. Figure 5.5(a) shows the measured specular ER spectra (taken from [144] and formatted) and the corresponding TDFFF fits.

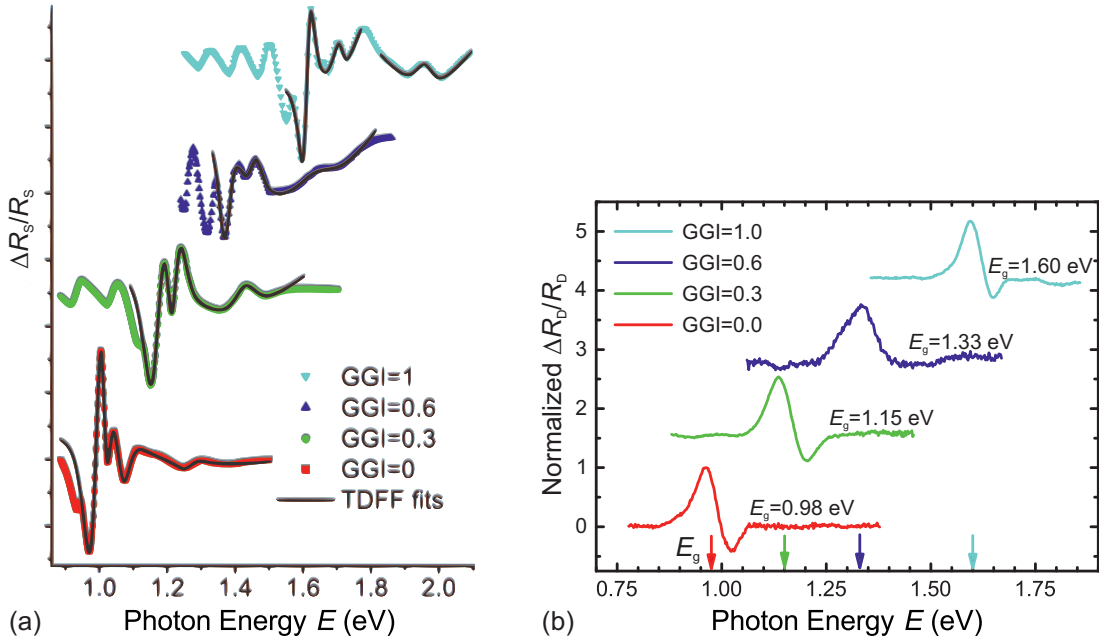


Figure 5.5: (a) Specular ER spectra of a series of CIGS solar cells with increasing Ga content (GGI) and corresponding fits involving multiple TDFFs and a parabolic background. Figure (a) taken from [144] and formatted. (b) Measurements in diffuse reflection geometry performed on the same cells. In contrast to specular ER, the diffuse ER spectra have less features and the band gap can be determined assuming a single optical transition. Arrows indicate the band gap determined from the modulus spectrum.

In the context of the previous chapter and this chapter it should be clear that especially the oscillatory features on the low-energy side of the spectra are due to thin-film interferences and that the entire signal is heavily distorted. As discussed in section 4.6 these spectra are likely to be overinterpreted due to the use of multiple TDFFs.

Figure 5.5(b) shows measurements on the same TFSCs which were performed in this work. Instead of specularly reflected light, diffusely reflected light was detected to measure $\Delta R_D/R_D$. It can be clearly seen that the spectra are much smoother in diffuse ER measurements. Furthermore, the lineshape rather resembles a single optical transition instead of multiple ones due to the single oscillatory feature. In a polycrystalline sample without a preferential grain orientation – as it is typically the case in CIGS TFSCs – selection rules cannot be applied and all optical transitions are allowed, independently of the AOI or the polarization of light. Consequently, an oscillator which is due to a critical point in the band structure cannot simply vanish when diffusely reflected light is detected instead of specularly reflected light which identifies the additional features in specular ER spectra as artifacts.

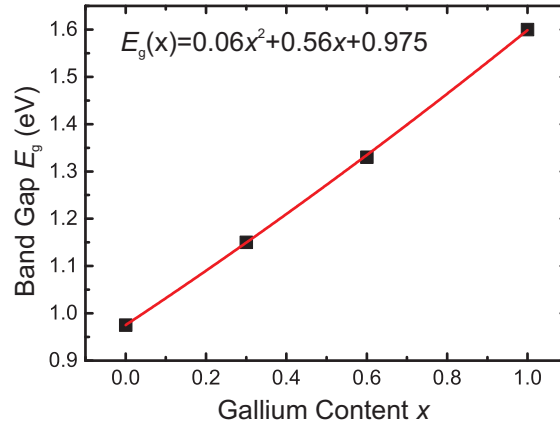


Figure 5.6: Determination of the band bowing coefficient b of CIGS. The bowing coefficient $b = 0.06$ is rather low and the band gap dependence on the gallium content is almost linear.

The band gaps of the TFSC absorbers were determined using the modulus spectrum method and are also shown in Fig. 5.5. The band bowing coefficient b was determined using a parabolic fit to the gallium-content-dependent band gap. This fit yields a comparatively low value of $b = 0.06$ eV and the resulting curve is shown in Fig. 5.6. It should be emphasized, however, that the exact composition of the samples besides the GGI is not known. Since the band gap of CIGS is not a sole function of x as discussed in subsection 2.1.2 the error due to the unknown composition is certainly larger than the error of the ER measurement and the corresponding evaluation. However, an increase of the band gap from 0.98 eV for CuInSe_2 to 1.6 eV for CuGaSe_2 can be seen in both Fig. 5.5 and Fig. 5.6 and is consistent with literature [30, 53]. The ER measurements were conducted on finished solar cells and therefore application-relevant film compositions. The deviation of the band bowing coefficient b from typical literature values [53] underlines again the importance of a reliable determination method of the absorber band gap in TFSCs such as ER.

5.5 Inhomogeneous Broadening in Electroreflectance

The last section of this chapter is dedicated to a discussion of the influence of inhomogeneous broadening in electroreflectance spectra. It will be shown, that inhomogeneous broadening may influence the lineshape of a measured ER spectrum, however, the presented evaluation methods in this work still extract the band gap correctly.

Aspnes' Third Derivative Functional Form is certainly the most popular method to analyze modulated reflectance spectra – mainly due to its simplicity of use. As it was shown in chapter 4 there are factors, namely thin-film interferences and the built-in electric field, which complicate the analysis of ER spectra of TFSCs.

One aspect which was not discussed so far is the impact of inhomogeneous broadening on a resonance of the dielectric function. The derivations of $\Delta\epsilon$ in the low-field and intermediate field regime explicitly consider a broadening parameter Γ . However, this parameter relates to homogeneous/lifetime broadening [15] of the excited state. In materials such as CIGS and especially CZTSSe this type of broadening is likely not the dominant one. It is more likely that, due to structural disorder and spatial composition fluctuations, the band gap itself varies spatially which is a form of inhomogeneous broadening. In the case of CIGS, the impact of a spatially varying band gap on solar cell efficiency was studied by Mattheis *et al.* and the main result of it is a lowering of the open-circuit voltage V_{OC} of the solar cell which was shown both theoretically and experimentally [48, 149]. Similar observations in terms of a lowered V_{OC} were reported for CZTSSe as well [12, 78, 150].

In the following, the role of inhomogeneous broadening in ER will be discussed in more detail. For simplicity, the derivations presented here will be limited to the low-field regime of ER.

5.5.1 Inhomogeneous Broadening in the Low-Field Limit

The central expression for the change in the dielectric function – and thus the basis for third-derivative modulation spectroscopy – is given by [15]:

$$\Delta\epsilon(\omega, \mathcal{E}) \propto \frac{(\hbar\Omega)^3}{(\hbar\omega)^2} \frac{\partial^3}{\partial(\hbar\omega)^3} ((\hbar\omega)^2 \epsilon(\omega)) \quad (5.1)$$

with $\hbar\Omega$ being a function of \mathcal{E} . It is important to note that the derivation of this expression in section 3.1 does not assume a particular shape of the dielectric function. Under the assumption of a square-root-shaped JDOS and lifetime broadening the expression simplifies to Aspnes' TDFF. The change in the dielectric function which corresponds to this situation is given by

$$\Delta\epsilon(\omega) \propto \frac{i}{(\hbar\omega - E_g + i\Gamma)^{2.5}} \quad (5.2)$$

which can be obtained by applying eq. 5.1 to the expression of $\epsilon(\omega)$ given in eq. 3.8.

A simple model to describe spatial band gap fluctuations in a solar cell would be a Gaussian distribution of the band gap within the ER measurement spot. A similar

assumption was made by Gokmen *et al.* to describe the absorption coefficient of CZTSSe [78]. Making the same assumptions, $\epsilon(\omega)$ reads

$$\epsilon(\omega) \propto \frac{i}{\sqrt{2\pi}\sigma} \int_0^\infty dE_g \exp\left(-\frac{1}{2}\left(\frac{E_g - \bar{E}_g}{\sigma}\right)^2\right) \frac{\sqrt{\hbar\omega - E_g + i\Gamma}}{(\hbar\omega)^2} \quad (5.3)$$

where \bar{E}_g denotes the average band gap value of the Gaussian distribution and σ the standard deviation. This means that every infinitesimal band gap interval dE_g contributes with a weighted square-root-shaped partial dielectric function $d\epsilon(\omega)$ of the form $\frac{1}{(\hbar\omega)^2} \sqrt{\hbar\omega - E_g + i\Gamma}$ as described in eq. 3.8. Similar to lifetime broadening, one effect of inhomogeneous broadening is the appearance of a tail in the imaginary part of the dielectric function below the average band gap, however, with a different decay behaviour.

In order to calculate the change in the dielectric function using eq. 5.1 one has to assume that the length over which the band gap fluctuates is larger than the average displacement of the electron during the acceleration by the applied electric field \mathcal{E} . Since eq. 5.1 requires the third derivative of the unperturbed dielectric function with respect to the photon energy it can simply be applied within the integral expression and thus yields

$$\Delta\epsilon(\omega) \propto \frac{1}{\sqrt{2\pi}\sigma} \int_0^\infty dE_g \exp\left(-\frac{1}{2}\left(\frac{E_g - \bar{E}_g}{\sigma}\right)^2\right) \frac{i}{(\hbar\omega - E_g + i\Gamma)^{2.5}}. \quad (5.4)$$

The consequence of band gap fluctuations which can be described by a Gaussian distribution is thus a Gaussian superposition of TDFE terms in $\Delta\epsilon$. It should be noted that the new expression for $\Delta\epsilon$ now contains two parameters which describe the individual broadening mechanisms. Whereas Γ still describes the influence of a finite lifetime of the excited state, σ represents the standard deviation of the band gap fluctuations. In the following, the resulting lineshapes of $\Delta\epsilon$ and thus the ER spectrum will be investigated for different ratios Γ/σ .

Figure 5.7 shows numerically calculated ER spectra assuming Gaussian broadening of the band gap for an assumed average band gap of $\bar{E}_g = 1$ eV. The corresponding TDFE fits (which assume lifetime broadening exclusively) and modulus spectra are shown as well. In order to obtain the spectra, $\Delta\epsilon(\omega)$ was calculated using eq. 5.4 and real and imaginary part were mixed using a phase factor θ , analogously to the lifetime-broadened TDFE expression (eq. 3.22):

$$\frac{\Delta R}{R} = \text{Re}\left(e^{i\theta} (\Delta\epsilon_1 + i\Delta\epsilon_2)\right).$$

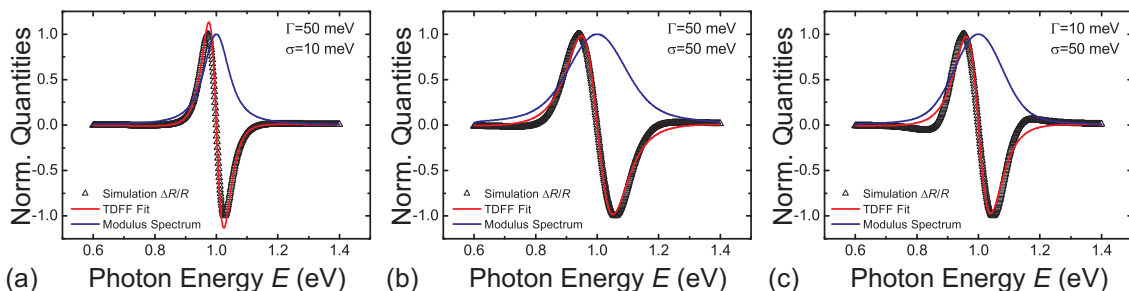


Figure 5.7: Simulated ER lineshapes for band gap fluctuations which can be described by a Gaussian distribution with standard deviation σ and corresponding TDFE fit as well as the corresponding modulus spectrum. In case lifetime broadening dominates (a) the lineshape is well-captured by a TDFE. In case of comparable homogeneous and inhomogeneous broadening (b) slight deviations in the lineshape become visible. For an inhomogeneously broadened system (c) the lineshape is not captured well at an increasing distance to the critical point at $\bar{E}_g = 1\text{ eV}$ due to overshoots. However, both the TDFE fit and the modulus spectrum yield correct energetic values for the critical point.

For a mainly homogeneously broadened system as shown in Fig. 5.7(a) with a Γ/σ ratio of 5 the ER lineshape still resembles a TDFE and is thus well captured by the fit. However, it should be noted that even in this case the resulting lineshape broadening Γ_{TDFE} determined by a TDFE fit does neither correspond to Γ nor σ . Hence it is not a good quantity for an absolute determination of, e.g., the amplitude of the occurring band gap fluctuations. The modulus spectrum is still centered at 1 eV and yields a correct value for the critical point. In the case of equal contributions of homogeneous and inhomogeneous broadening as shown in Fig. 5.7(b), and finally, in the case of a spectrum which is dominated by inhomogeneous broadening (c), the TDFE fit is not able to capture the resulting lineshape perfectly. This is mainly due to changes in the slope of the oscillation. However, the capture of the main feature of the oscillation is sufficient in both cases to determine the energetic value of the average band gap correctly.

The same holds for the corresponding modulus spectra which are still centered around 1 eV. The lineshape of the modulus spectrum is transformed from a rather Lorentzian lineshape in Fig. 5.7(a) to a Gaussian lineshape in Fig. 5.7(c). However, also in these two cases, the broadening of the simulated lineshape does not allow for a simple determination of Γ and σ . The values of Γ_{TDFE} of the fit to the ER spectrum and σ_{Gaussian} of the Gaussian fit to the modulus spectrum are systematically larger than the values which were used in the simulation. Generally, the lineshape of the modulus spectrum can also be fitted with a Voigt lineshape, which is able

to capture this superposition of Gaussian and Lorentzian lineshape. However, the energetic values for the resulting average band gap were independent of the used lineshape. In principle, a modified procedure could be used in order to fit measured ER spectra in this work. However, this was not performed since it would have introduced further degrees of freedom and although the ER spectra of TFSCs are influenced by several circumstances they are still rather featureless. Since both a TDFF fit and the evaluation of a modulus spectrum yield the correct values for \overline{E}_g they were used instead.

In conclusion, this means that a TDFF analysis can also be performed in the case of an ER spectrum which is inhomogeneously broadened due to a Gaussian distribution of local band gaps. The resulting energetic value represents the average band gap value \overline{E}_g . The broadening parameter of the resulting lineshape does not exhibit a simple correlation to the homogeneous or inhomogeneous broadening parameters and should therefore not be used to derive quantitative statements. It was furthermore shown, that a TDFF analysis and a modulus spectrum analysis yield consistent results for the energetic position of the critical point.

5.5.2 Experimental Evidence of Inhomogeneous Broadening

After this theoretical consideration of inhomogeneous broadening in ER experimental evidence will be provided in the following. Figure 5.8(a) shows a measured ER spectrum of a solution-processed CZTSSe solar cell. The AOI was set to 40° and the AOD to 0° . On the low energy side of the spectrum remainders of thin-film interferences still influence the lineshape slightly. On the high-energy side of the spectrum a TDFF fit is not able to capture the lineshape of the measured ER spectrum completely. This slope of the measured spectrum in this spectral region is steeper compared to the TDFF lineshape. As discussed in the previous subsection this could be due to a dominant inhomogeneous broadening as shown in Fig. 5.7(c).

The corresponding modulus spectrum yields further insights. The lineshape of the transformed spectrum can be captured by a single Gaussian function the center of which is identical with the energetic position of the critical point resulting from a TDFF fit. The observation of a Gaussian-shaped modulus spectrum was a general observation in ER spectra of CZTSSe solar cells. A fit with a Lorentzian lineshape did not capture the measured lineshape as well as a Gaussian lineshape, however, it resulted in the same energetic value of E_g . It should be noted that the spectra shown in Fig. 5.8 were recorded on CZTSSe solar cells with a low degree of Cu–Zn disorder. As it will be shown in chapter 7 this accounts for the relatively large energetic value of the absorber band gap [151]. Another feature of the modulus

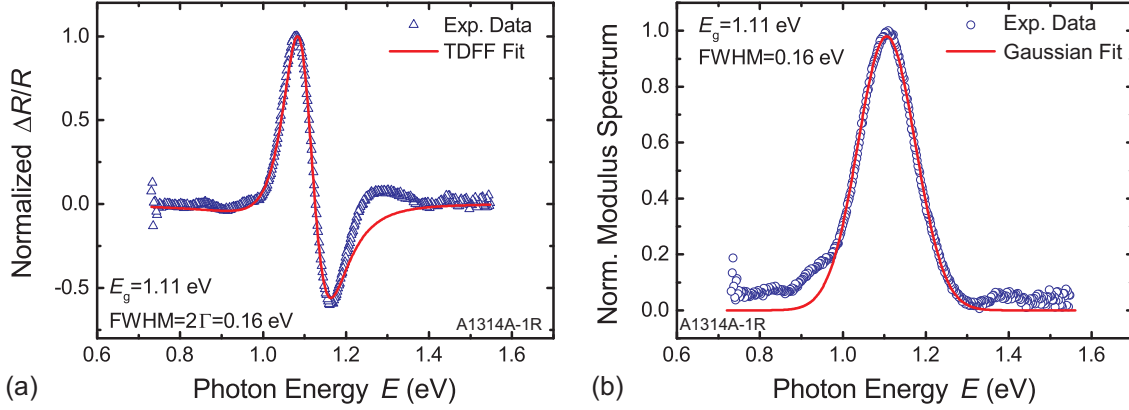


Figure 5.8: (a) Measured ER spectrum of a CZTSSe solar cell and corresponding TDFF fit. (b) The resulting modulus spectrum exhibits a Gaussian shape and indicates a dominant inhomogeneous broadening. Both methods of analysis yield equivalent values for the energetic position of the critical point.

spectrum in Fig. 5.8(b) is a second small peak at $E \approx 1.39$ eV (determined by fitting a second Gaussian function). This peak was frequently detectable in the modulus spectra of ER measurements and is separated from the fundamental resonance by more than the FWHM of it. It could be attributed to a band splitting due to the spin-orbit interaction. The corresponding split-off energy in this case is

$$\Delta_{\text{SO}} = 0.18 \text{ eV}.$$

So far in this work, it was shown how to record and analyze ER spectra of TFSCs correctly, also in the case inhomogeneous broadening is present. Different lineshape-distorting mechanisms have been introduced and discussed thoroughly. In the following, ER measurements will be compared to and supported by different characterization techniques to shed light on the radiative transitions of CZTSSe.

5.6 Summary

In this chapter, it was shown that the effect of interference-related lineshape distortions in ER spectra can be substantially reduced by detecting the diffuse reflection instead of the specular reflection in ER measurements. Using FDTD simulations it has been shown that diffusely reflected light R_D from a rough surface reacts analogously to specularly reflected light R_S to a change in the dielectric function $\Delta\epsilon$. The TDFF signature could be detected in $\Delta R_D/R_D$ which makes this quantity suitable for modulation spectroscopy.

Experimentally, a series of three CZTSe solar cells with different window layer thicknesses but identical absorber layers was investigated. The sample series showed very different ER spectra in specular reflection and could not be fitted with a consistent set of oscillators. Interestingly, in diffuse reflection all ER spectra reduced to a single oscillatory feature which could be fitted with a single TDFF lineshape. The resulting band gap values coincided within a range of a few meV.

Furthermore, similar results could be found for a CIGS TFSC series with different Ga contents. In contrast to specular ER measurements, diffuse ER measurements revealed single optical transitions at the fundamental band gap for each GGI. It should be emphasized that an increase in the number of oscillators to capture the lineshape of the measured spectrum perfectly is not the correct way to analyze ER spectra of TFSCs. Instead, the number of oscillators should be kept at a minimum and ideally, only one effective optical transition should be assumed.

Furthermore, it has been shown that ER spectroscopy can also be used to investigate samples the ER spectra of which exhibit inhomogeneous broadening. Both a TDFF analysis and the modulus spectrum are able to determine a correct value for the band gap, except that this value represents an average band gap. Inhomogeneous linewidth broadening can be seen in the modulus spectrum of measured ER spectra since they can be fitted better by a Gaussian function, in contrast to lifetime-broadened spectra which can be fitted by a Lorentzian lineshape.

If these precautions both in terms of measurement and evaluation are taken, ER spectra, in particular diffuse ER spectra, reveal the spectral position of the fundamental band gap of TFSC absorber layers.

After chapters focussing on the method itself, ER will be used to correlate the fundamental band gap to radiative recombination processes in the next chapter. Furthermore, the full potential of this technique will be used to easily detect even smallest band gap changes in CZTSSe absorber layers which are induced by post-annealing procedures. The results of these experiments will be presented in chapter 7.

Chapter 6

Optical Transitions in $\text{Cu}_2\text{ZnSn}(\text{S,Se})_4$

The optical transitions in CZTSSe are the subject of many publications in literature and this field of research is controversially discussed. One of the main reasons for that is the wide range of material compositions in solar cells. In addition, very often only one particular technique is used to obtain data. Therefore, many reports in literature about radiative recombination are contradictive. This chapter gives an overview on the insights into the radiative processes in CZTSSe gained in this work. In contrast to most reports in literature, the identification of the individual contributions to radiative recombination is done using complementary techniques such as PL and PLE or ER. Furthermore, the temperature dependence of the band gap of CZTSSe is investigated by ER measurements. Beforehand, ER is compared to the measurement of the external quantum efficiency (EQE) of a CZTSSe solar cell as a means of absorber band gap determination. Parts of the results of this chapter were achieved in the Master's thesis of Christian Zimmermann, and a more detailed PLE investigation can be found in [113].

6.1 Comparison of Different Methods of Band Gap Determination in Thin-Film Solar Cells

Although ER is a commonly used characterization technique in semiconductor physics there are only few reports in literature dealing with the determination of the absorber band gap in TFSCs using ER [143, 144]. The standard method of band gap determination in TFSCs is the analysis of the low-energy slope of an EQE

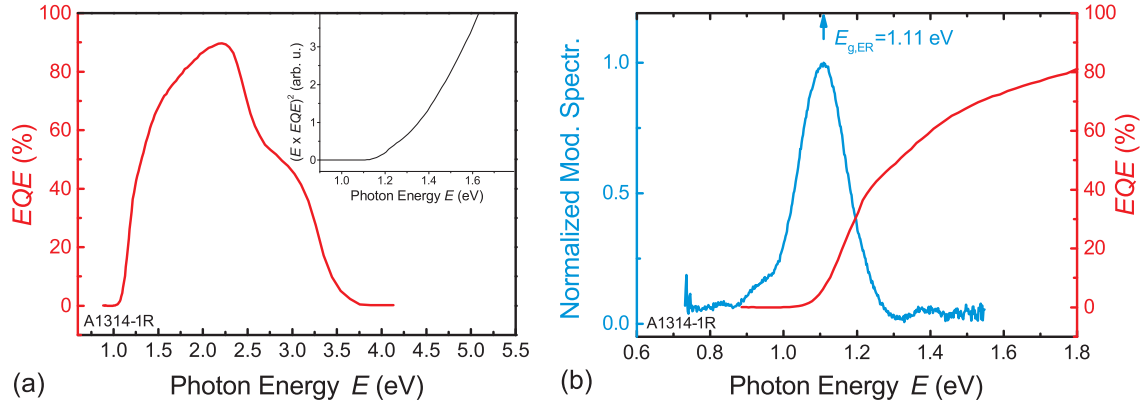


Figure 6.1: (a) EQE spectrum of a CZTSSe TFSC (Courtesy of ZSW). The corresponding Tauc plot (inset) does not show a linear slope and can therefore not be used to extrapolate a band gap value. (b) Modulus spectrum of an ER measurement on the same cell (blue) and zoomed view of the EQE in this spectral region. The modulus spectrum lies in the tail region of the EQE.

measurement [111]. Therefore, this technique will be discussed and compared to ER measurements in the following. Fig. 6.1(a) shows an EQE measurement of a CZTSSe TFSC and the corresponding Tauc plot [153] within the spectral region of the absorber band gap (inset). Normally a linear regression would be used to extrapolate the slope of the Tauc plot and to determine E_g at the corresponding zero-crossing. However, this is not possible as there is no well-defined region in the Tauc plot which could be used for a linear regression. The reasons for this will be discussed in more detail in the following.

There are several physical assumptions for an EQE Tauc plot analysis the validity of which has to be verified. First, the scaling of the EQE Tauc plot assumes a complete and energy-independent carrier extraction from the device so that the shape of the low-energy side of the EQE is proportional to the absorption coefficient $\alpha(\omega)$ exclusively. While this may be a reasonable assumption in crystalline Si solar cells and high-quality epitaxial III–V solar cells [111] it is highly questionable whether those assumptions are also valid for a semiconductor with a poor electronic quality such as CZTSSe. Since an EQE measurement represents a macroscopic current measurement, it is not only influenced by the absorber properties but also by interface properties and the bulk properties of the other functional layers of a TFSC. Influences such as a low carrier mobility or band gap fluctuations can lead to carrier localization which will effectively distort the lineshape of the EQE.

6.1 Comparison of Different Methods of Band Gap Determination in Thin-Film Solar Cells

Second, even if the assumption of an external quantum efficiency which is simply proportional to the absorption coefficient $\alpha(\omega)$ was justified, the Tauc plot still assumes a very simple shape of the absorption for a direct semiconductor [153]:

$$\alpha(E) \propto \frac{1}{\omega} \sqrt{E - E_g}.$$

Only in this case, the scaling of $(E\alpha(E))^2$ over E yields a straight line and allows for an extraction of E_g at its zero-crossing. It has been shown that the CZTSSe material system exhibits severe band tailing which is also supposed to contribute to the lack of open-circuit voltage [78]. In some reports this has been accounted for by modeling the absorption using a Gaussian band gap distribution as shown in subsection 5.5 and [150]. Furthermore, it was already pointed out that the term band gap needs to be used with caution since it is not unambiguously defined in CZTSSe [150]. In particular, this means that optically active states as they are defined by the dielectric function and macroscopically mobile states as they are defined by contributions to current transport do not necessarily coincide. In this work the term band gap refers to the optical band gap – defined by a significant contribution in the JDOS.

Figure 6.1(b) shows the low-energy slope of the EQE and the corresponding modulus spectrum of an ER measurement which was performed on the same cell. A pronounced tail in the EQE can be observed in the vicinity of the absorber band gap. It can further be seen that the center of the modulus spectrum is situated within the tail of the EQE and the center of it yields a band gap value which rather coincides with the root of a linear extrapolation of the EQE plot and not the Tauc plot. Again, this means that there is a large amount of optically active states in CZTSSe which do not contribute to current transport. In turn, this limits the use of the Tauc plot for band gap determination from an EQE spectrum.

For completeness, it should be mentioned that another method to determine the absorber band gap is the inflection point of the low-energy slope of the EQE spectrum [78]. The justification of this method is that the band gap values derived using it are more robust than the values determined by the Tauc plot [78]. The absorber band gap determined by this method would be $E_{g,\text{inflection}} = 1.15 \text{ eV}$ and hence larger than the value derived by ER which is $E_{g,\text{ER}} = 1.11 \text{ eV}$.

In conclusion, it can be stated that a determination of the optical band gap of CZTSSe is not possible from EQE data due to the mechanism of the measurement. EQE is a perfectly valid method to judge the performance of a solar cell and to identify loss mechanisms spectrally resolved. However, there are too many other influences on an EQE spectrum which forbid the simple application of a Tauc plot to determine the band gap of the absorber layer. It is certainly possible to determine the spectral position at which the solar cell starts to generate a photo-current, however,

this onset cannot simply be related to the optical band gap of the absorber (unless it is simply defined that way).

In contrast to that, the validity of the assumptions of ER measurements have been discussed and investigated intensively in this work. The main advantage of ER is that the measurement does not need a macroscopic mobility over the entire device and electrons only need to be accelerated by the applied electric field \mathcal{E} . Comparing ER to the low-energy slope of EQE measurements suggests severe structural inhomogeneities in the CZTSSe devices. Although a significant optical activity is present, as indicated by the spectral position of the ER measurement, current transport is not taking place. Similar measurements on CIGS solar cells yielded a smaller difference between the band gap as determined by ER and the resulting band gap from the extrapolation of a Tauc plot or the inflection point of the corresponding EQE measurement. The splitting of the two “band gap” energies in CZTSSe as determined by EQE and ER and the width of the corresponding ER spectra could therefore be seen as a measure of the depth of the band tailing and subsequent carrier localization.

6.2 Review of Radiative Recombination Mechanisms in $\text{Cu}_2\text{ZnSn}(\text{S},\text{Se})_4$

A central problem of the analysis of luminescence spectra from CZTSSe layers or solar cells is their featureless structure. Individual contributions are washed out and can only be recognized as shoulders at best. Furthermore, the presence of different defects in CZTSSe strongly depends on the composition and the fabrication procedure. The same holds for secondary phases with band gaps in the energetic vicinity of the CZTSSe band gap and defect-related transitions. This makes it very difficult to draw a conclusive picture of radiative recombination in CZTSSe which accounts for all observed phenomena. Therefore, an overview on reported radiative recombination mechanisms in CZTSSe will be given in the following. The discussion is partly based on a review which has recently been published by Teixeira *et al.* [80] and additional information will be given when necessary.

6.2.1 Defect-Related Recombination

A high density of intrinsic point defects in CZTSSe does not only lead to a high doping but also a high degree of compensation [78–80, 140]. Therefore, both types, donor and acceptor defects are present in the material and are likely to participate

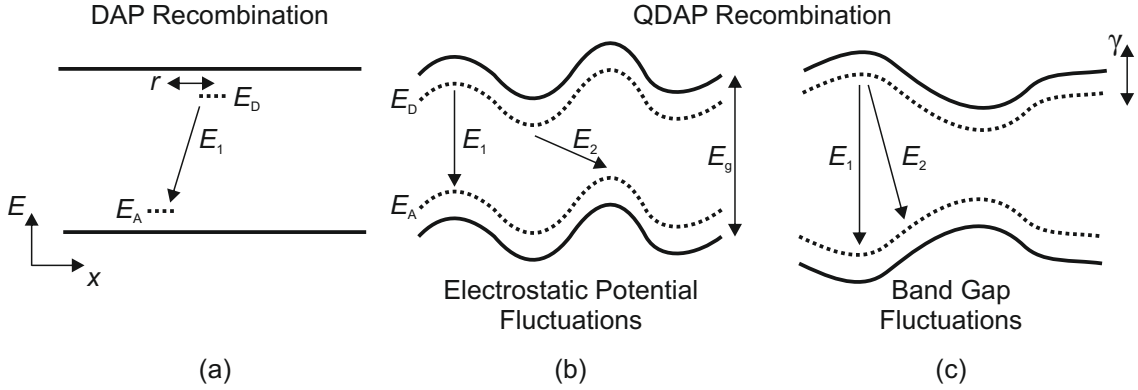


Figure 6.2: Comparison of (a) donor–acceptor pair recombination to (b) + (c) quasi-donor–acceptor pair recombination. In the case of quasi-donor–acceptor pair transitions the energy levels of donor and acceptor states are typically not formed by individual defects but by defect aggregates. (b) Very often this is accompanied by band edges fluctuating in parallel which is caused by charged defects or defect aggregates. The occurrence of spatially indirect radiative transitions leads to a redistribution of photon emission energies over a larger interval. (c) Similar observations can be made in case the band gap itself is fluctuating due to, e.g., spatial composition variations.

in radiative recombination processes. Hence, donor–acceptor pair (DAP) transitions are likely to occur. The emission energy of a DAP transition is given by [154]

$$h\nu \approx E_g - (E_d + E_a) + \frac{e^2}{\kappa r} \quad (6.1)$$

with E_d and E_a being the ionization energy of donors and acceptors, respectively and $\kappa = 4\pi\epsilon_{\text{rel}}\epsilon_0$. In addition to that, the distance between donor and acceptor r influences the emission energy due to Coulomb interaction. This situation is illustrated in Fig. 6.2(a). The luminescence from DAP transitions shows a characteristic behaviour with varying experimental conditions. In the case of an increase in excitation power a shift of the PL maximum towards higher energies is observed. This is due to DAPs with a smaller distance, and therefore higher transition energy, being populated (compare eq. 6.1). A similar observation is made for an increase in temperature. The contribution from DAP transitions will also experience a shift towards higher photon energies due to thermal population of energetically higher levels. It should be noted that very often in literature the spectral position of the PL maximum is discussed. As will be shown in this chapter this quantity is somewhat difficult to interpret which is why additional to this quantity, the shape of the PL spectrum is analyzed as well.

Dobrego and Shlimak pointed out that in the case of high defect concentrations the energy levels participating in recombination processes are not formed by individual

defects but by defect aggregates. The figure of merit which is used to characterize the high defect density is $N_d a_e \gg 1$ ($N_a a_h \gg 1$) for donors (acceptors) with N_d (N_a) being the donor (acceptor) density and a_e (a_h) being the Bohr radius of the donor (acceptor) defect [80]. After Dobrego and Shlimak, the distance r which is relevant for the Coulomb interaction is given by the distance between defect aggregates and not individual point defects in the case of high defect densities. Therefore, the term quasi-donor–acceptor pair (QDAP) recombination was introduced. Additional to that charged defect aggregates lead to fluctuations in the band edges. The most simple situation is given by a fluctuation of CB and VB edge in parallel. This is referred to as electrostatic potential fluctuations and has been mentioned in the context of CZTSSe as well [78, 79]. The corresponding band structure is shown in Fig. 6.2(b). In the case of fluctuating band edges, the experimental observations in luminescence spectra differ from those of DAP transitions. This is due to a distribution of radiative transitions over a larger energetic interval due to spatially indirect transitions. Furthermore, an increase in excitation power leads to a shift of the PL maximum towards higher energies, however, larger than the one observed for DAP transitions [154]. This is again due to the fact that the energy levels are distributed over a larger energetic interval and in turn filling effects result in this increased shift of the PL maximum.

In contrast to that, screening of charged defects by the additionally generated carriers can lead to a decrease of electrostatic potential fluctuations [80]. However, this should lead to an actual blue shift of the entire PL signal since this modifies the JDOS whereas the above-mentioned state-filling only affects the occupation of states. In both cases of fluctuating band edges an increase in the sample temperature leads to a shift of the PL maximum towards lower energies in contrast to DAP transitions. This can be explained by an increased mobility of the carriers which are then able to reach energetically deeper valleys in the spatially-fluctuating band structure and recombine at lower emission energies. From this discussion it is evident, that the sole consideration of the energetic position of the PL maximum is somewhat problematic. Therefore, not only the energetic position of the PL maximum is analyzed in the following but also the shape of the measured spectra. In particular, the low-energy slope of the spectra is analyzed in order to distinguish screening and state-filling effects.

Yu *et al.* extended this picture of recombination to a spatially-fluctuating band gap [155, 156]. The emission energy is not given by eq. 6.1 anymore but mainly influenced by the amplitude of the band edge fluctuation γ :

$$h\nu \approx E_g - (E_d + E_a) - 2\gamma. \quad (6.2)$$

This formula is also valid for electrostatic potential fluctuations in case the amplitude of the band edge fluctuations γ dominates over the Coulomb term in eq. 6.1. For

band gap fluctuations the same qualitative observations were made in the experiment both in terms of a shift of the PL maximum towards higher photon energies with increasing excitation power and a red shift with increasing temperature [156]. The corresponding spatial band structure is illustrated in Fig. 6.2(c).

These are aspects of defect-related recombination which are relevant for an investigation of radiative recombination in CZTSSe. It remains to be proven whether defect levels with a defined distance to the band edges are a realistic assumption for CZTSSe. By means of DFT calculations for the sulphide kesterite, Huang and Persson were able to show that an abundant (in the order of one per unit cell) presence of $[\text{Zn}_{\text{Cu}}+\text{Cu}_{\text{Zn}}]$ and $[\text{Zn}_{\text{Cu}}+\text{V}_{\text{Cu}}]$ defect pairs influences the band gap itself [77]. Similar calculations were published by Chen *et al.* and therefore it cannot be excluded that defects and defect clusters are altering the local band structure in kesterite materials [47].

6.2.2 Band-Related Recombination

As it was discussed in the previous section, in the QDAP model radiative transitions occur via defect levels or defect aggregates which are separated from the band edges. However, a large density of charged defects alters the band structure locally and leads to the formation of band tails in the JDOS [157]. Romero *et al.* suggested a model for the radiative recombination in CIGS and CZTSSe in which pronounced contributions to PL spectra are due to band tail states [130]. The tails are caused by a large and spatially inhomogeneous defect distribution. However, the recombination is taking place between band tail states and not defects. Especially excitation power-dependent PL measurements are often performed for the identification of band-related luminescence [79,80,104]. In terms of the spatial band structure the situation is very similar to the one presented in Fig 6.2(b) [130]. However, the radiative transitions occur via band tail states and not via isolated defect levels as in the case of QDAP recombination. Again, the main factor which influences the energetic position of the PL maximum is the amplitude of the band edge fluctuations γ [80]:

$$h\nu \approx E_g - 2\gamma. \quad (6.3)$$

In a comparative study with CIGS, Gokmen *et al.* suggested that electrostatic potential fluctuations due to charged defects such as, e.g., $[\text{Cu}_{\text{Zn}}^- + \text{Zn}_{\text{Cu}}^+]$ mainly influence the formation of band tails in CZTSSe. They even suggested electrostatic potential fluctuations to be the dominant performance-limiting factor in CZTSSe solar cells [78]. An important aspect of electrostatic potential fluctuations in kesterites was discussed by Teixeira *et al.* [80]. The amplitude of electrostatic potential fluctuations γ depends on the carrier density N in the material. An increase in charge

carrier density by, e.g., an increase in excitation power leads to a screening of charged defects and therefore a lowering of the amplitude γ . Therefore, a blue shift of the PL peak with increasing excitation power can be attributed to a screening of charged defects in the case of electrostatic potential fluctuations. The same argument would also be valid for the case of QDAP transitions involving electrostatic potential fluctuations. In this case, however, an actual blue shift of the entire PL spectrum should be observable since the JDOS is modified and energetically lower transitions are extinguished.

Some reports in literature depict the presented recombination mechanisms as contradictory to each other [158]. Instead, they should be seen as different aspects of radiative recombination in CZTSSe and they are likely to occur simultaneously depending on the excitation regime and the sample composition. Furthermore, it should be noted that there can be multiple causes for band tails to arise. Electrostatic potential fluctuations are one mechanism which leads to a spatially constant band gap, and the lowering of the energetic position of the PL maximum is due to spatially indirect transitions. In contrast to that, compositional fluctuations can lead to a spatial fluctuation of the band gap itself and thus to an inhomogeneous broadening of E_g as it was discussed in section 5.5. However, spatially indirect transitions are also possible in this case.

The main difference between the presented recombination mechanisms is whether the recombination involves isolated impurities/impurity clusters or whether it involves band states. As will be shown in the next sections, both situations are present in the CZTSSe layers which were investigated in this work – depending on which excitation power and temperature is used. Furthermore, it will be shown that the dominating cause for fluctuating band edges in the investigated CZTSSe solar cells are likely to be band gap fluctuations and not electrostatic potential fluctuations since screening effects can be excluded from the measurements. However, since the measurements were performed at low temperatures a precise knowledge of the band gap at this temperature is necessary. This will be investigated in the following.

6.3 Anomalous Thermal Dependence of the Band Gap of $\text{Cu}_2\text{ZnSn}(\text{S,Se})_4$

When it comes to the analysis of radiative recombination processes the temperature dependence of the band gap has to be taken into account, especially when comparing absolute energetic positions of different contributions of a PL spectrum. In the case of the I–III–VI₂ semiconductors a very low temperature dependence of the band gap

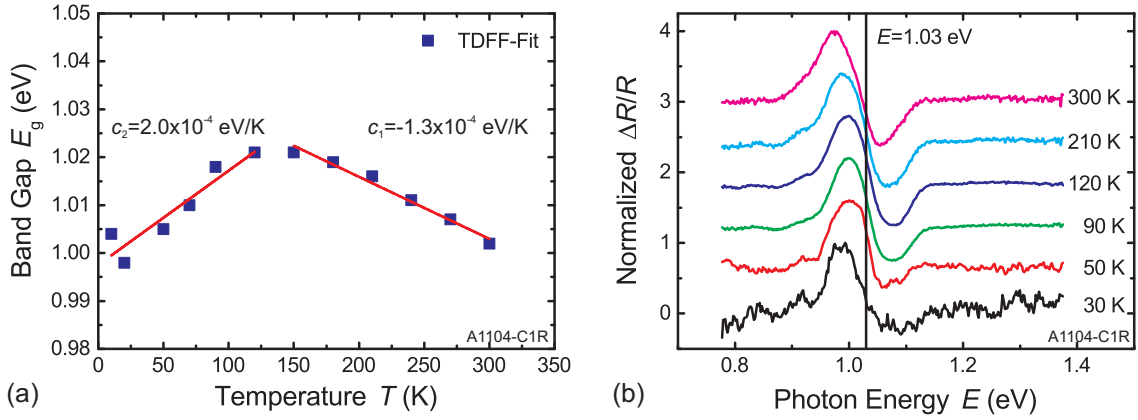


Figure 6.3: (a) Temperature-dependent absorber band gap of a CZTSSe solar cell as determined by a TDFE fit of an ER measurement. From 120 K to room temperature E_g decreases by approximately 0.02 eV. For temperatures below 120 K, E_g also decreases by 0.02 eV. (b) Corresponding ER spectra (stacked) for different temperatures. Whereas for temperatures above 120 K the ER feature actually shifts, it mainly becomes more asymmetric for lower temperatures. The black vertical line is for orientation.

was found compared to their respective II–VI analogues [56, 159]. The change in band gap energy of, e.g., CuInSe_2 from room temperature down to 77 K is as low as 40 meV [159].

The reason for this is the admixture of Cu-d orbitals to the valence band states [159]. Due to the similarity in the band structures of the chalcopyrite and kesterite semiconductors similar observations can be expected in terms of the thermal dependence of E_g .

Figure 6.3(a) shows the temperature dependence of E_g as measured by ER for a solution-processed CZTSSe solar cell with a sulfur content of $y \approx 8\%$. The band gap at each temperature was determined using a TDFE fit of the individual measurement. Above 120 K the band gap can be described by a negative linear temperature coefficient of $c_1 = -1.3 \times 10^{-4}$ eV/K. In this temperature range the band gap shifts by about 0.02 eV and is in a similar range as the band gap shift reported for CuInSe_2 and hence much lower than in comparable II–VI semiconductors [159].

Going from 120 K to even lower temperatures the band gap is decreasing again by 0.02 eV. Comparing the individual ER spectra at different temperatures in Fig. 6.3(b) one finds that the ER feature actually shifts its spectral position from room temperature to a temperature of 120 K which the detected shift in the band gap is due to. For lower temperatures the ER spectrum becomes more asymmetric rather than it

shifts. This suggests that the modulation mechanism could also be modified at low temperatures. In this region the temperature coefficient is positive and is determined to be $c_2 = 2.0 \times 10^{-4} \text{ eV/K}$.

Similar observations concerning this anomalous temperature dependence of the fundamental band gap were reported by several researchers for chalcopyrite (CP) semiconductors of various compositions [160–163], however, not yet for CZTSSe. This physical peculiarity can be explained by the band structure of CP semiconductors, in particular the presence of Cu-d orbitals in the formation of the VB states. Due to the similarities of CPs and kesterite in the formation of the VB states, the same mechanisms can account for the anomalous temperature dependence of the band gap in CZTSSe.

The following mechanism was proposed by Artus and Bertrand [163]. As it is the case in II–VI semiconductors as well, in CP semiconductors the temperature dependence of the band gap is also caused by lattice dilatation with increasing temperature and electron–phonon interaction. In II–VI and III–V semiconductors both effects influence the band gap in the same way in terms of their temperature dependence. However, in CP materials the lattice dilatation with increasing temperature leads to a decrease in the p–d hybridization between the group I (Cu) cations and the chalcogen anions. Since the energetic position of the topmost VBs is due to a repulsive interaction between the p- and d-states a lattice dilatation causes the topmost VB not to be pushed upward into the band gap as strongly as for smaller lattice constants.

This effectively increases the band gap of the material with increasing temperature. This volume effect dominates at low temperatures due to the lack of phonons. It is then compensated by the electron–phonon interaction at temperatures around 100 K which is also observed in our measurements on CZTSSe solar cells. Due to the analogous formation mechanism of the VB states in CZTSSe this explanation can account for the observed temperature dependence of E_g as well. It should be emphasized that this is the first time that an anomalous temperature dependence of the band gap in CZTSSe with temperature is observed experimentally.

The same temperature-dependent ER measurements were performed for a pure CZTS solar cell. The cell was fabricated at the University of Uppsala by annealing of sputtered metallic precursors described in the baseline process in [164]. The resulting ER spectra are shown in Fig. 6.4.

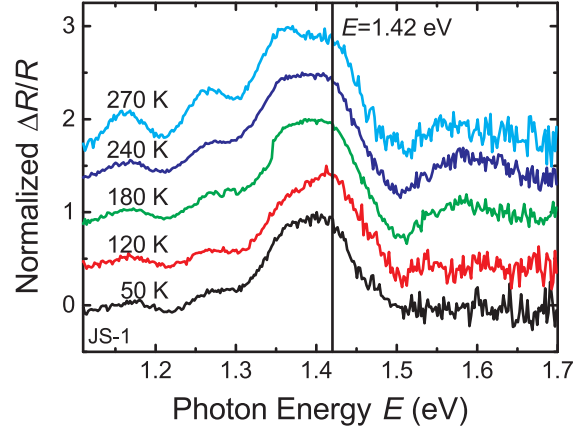


Figure 6.4: Temperature-dependent ER spectra of the fundamental band gap region of a CZTS solar cell. Within the accuracy of the measurement no shift in the band gap with temperature can be observed. The black vertical line is for orientation.

The ER measurements still showed strong interference fringes within the region of the fundamental band gap which made an exact determination of the band gap impossible. An estimated value by a manual TDFE fit would yield a band gap of $E_g \approx 1.42 \text{ eV}$, however, with a large uncertainty of at least 0.03 eV . However, by inspection with the naked eye, a possible shift of the band gap with temperature can be estimated to be lower than 0.02 eV . It should be emphasized that the purpose of this experiment was not to accurately determine the band gap of CZTS. The sole purpose of it was to confirm the low thermal dependence of E_g which is consistent with the observations presented above for CZTSSe.

However, the results contradict the findings presented by Sarswat *et al.* for CZTS thin films on glass which were characterized by transmission measurements [165] employing a Tauc plot. For these measurements a decrease of about 0.1 eV was found for an increase in temperature from 77 K to 300 K . However, no data for temperatures below 77 K is presented which makes it impossible to judge whether the band gap is decreasing again with lower temperatures.

In conclusion, the thermal dependence of E_g in the kesterite material system was studied using ER measurements and was determined to be anomalous compared to the structurally related II–VI semiconductors in terms of a change from a positive to a negative temperature coefficient. The reason for this lies in the p–d hybridization of atomic orbitals which leads to the formation of the VB states. The low temperature dependence of E_g needs to be taken into account in the analysis of temperature-dependent PL spectra of CZTSSe solar cells in the next section.

6.4 Identification of Contributions to Radiative Recombination

As it was discussed in section 6.2 there is no agreement in literature about the radiative recombination mechanisms in CZTSSe. In this section, the results of ER-T, PLE- and PL-measurements will be presented in order to determine the energetic position of the radiative recombination with respect to the band gap.

It stands to emphasize that the results which were found in this work are valid for solution-processed CZTSSe solar cells prepared after [102, 146]. The conclusions which are drawn in the following are therefore specific for this kind of sample. In order to draw a generalized picture of the radiative recombination in the entire CZTSSe material system, an investigation of a larger composition range remains to be performed.

6.4.1 Excitation Power-Dependent Photoluminescence

In order to identify individual contributions to the PL spectrum, an excitation power series was recorded. The sample which was used exhibited a low degree of Cu–Zn disorder due to an additional annealing procedure and thus an increased band gap. Details on the dependence of E_g on the degree of Cu–Zn disorder will be discussed in chapter 7. This particular sample was chosen since the increased band gap allowed to record the entire PL spectrum over several orders of magnitude of excitation power due to the improved overlap with the spectral responsivity window of the InGaAs photodiode which was used to record PL spectra. Furthermore, a low degree of Cu–Zn disorder actually corresponds more to the ideal kesterite crystal structure than the degree of Cu–Zn disorder of the as-prepared state of the solar cell as will be shown in the next chapter. However, it should be noted that the results presented here were typical and the conclusions which will be drawn apply to as-prepared samples without thermal post-processing as well.

In order to analyze the spectra quantitatively, a double sigmoidal expression after Krustok *et al.* was used to fit the obtained PL spectra [166].

$$I_{\text{PL}}(\hbar\omega) = A \left(\frac{1}{1 + \exp\left(-\frac{\hbar\omega - E_1}{W_1}\right)} \right) \left(1 - \frac{1}{1 + \exp\left(-\frac{\hbar\omega - E_2}{W_2}\right)} \right) \quad (6.4)$$

The expression is able to capture the asymmetric lineshape of the PL spectrum for low excitation powers as long as only one contribution to the spectrum is visible as

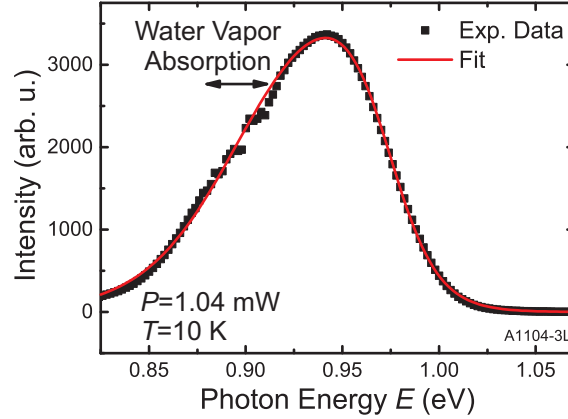


Figure 6.5: Comparison of experimental data and corresponding double sigmoidal fit after Krustok [166]. The fit captures the asymmetric lineshape well. Deviations only arise in the energetic vicinity of water vapor absorption lines.

shown in Fig. 6.5. The sole purpose of the fit is to determine the integrated PL yield Y and the maximum of the PL spectrum $E_{\text{PL,max}}$ using an analytic expression. The assumptions of the model presented in [166] have not been validated. Therefore, the fit parameters A , E_1 , E_2 , W_1 and W_2 do not have a physical meaning which relates to material parameters of CZTSSe.

Figure 6.6(a) shows low-temperature PL spectra for which the excitation power was varied over four orders of magnitude. A clear shift of the PL maximum towards higher photon energies is visible with increasing excitation power. Whether this shift is due to state-filling or screening of electrostatic potential fluctuations will be investigated in the following.

Figure 6.6(b) shows logarithmic plots of the PL excitation power series. It is evident that the low-energy slope of the spectra remains unaltered by an increase in excitation power. In the case of screening of electrostatic potential fluctuations by generated charge carriers a change in the slope on the low-energy side of the spectrum would be expected. In consequence, contributions of indirect transitions from deeper valleys would vanish due to the flattening of the spatial band structure.

Since this is not observed, it can be concluded that the influence of electrostatic potential fluctuations is not the dominant contribution to the low-energy side of the PL spectra in our samples or charged defects cannot be screened sufficiently by the additionally generated carriers. Instead, the reason for the shift of the PL maximum towards higher energies is a filling of energetically higher states. This is consistent with the observation of ER and PLE measurements which were recorded

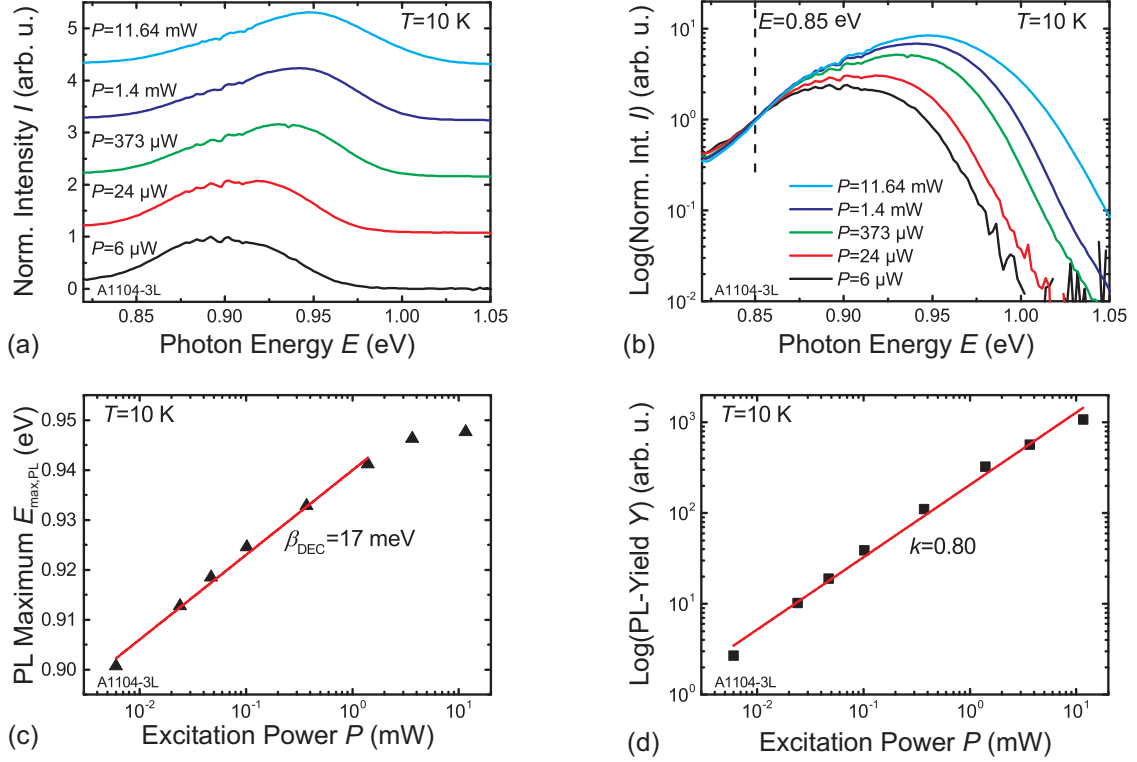


Figure 6.6: (a) Normalized PL-spectra of a CZTSSe solar cell show a shift of the PL maximum towards higher photon energies with increasing excitation power. (b) A logarithmic plot reveals that the low-energy slope of the spectrum does not change. On the high-energy side the slope is not changing either. Instead, a second contribution emerges for nominal pumping powers above $P = 1.4\text{ mW}$. Spectra were normalized to 0.85 eV (dashed line). The shift of the PL maximum (c) with increasing excitation power is 17 meV per decade in the range where only a single contribution is visible in the PL spectrum. (d) The double-logarithmic plot of the power-dependent PL-yield Y reveals a value of $k = 0.8$ consistent with the assumption of a defect-related radiative recombination. After [113, 152].

in the presence of an additional constant light bias. Both measurements showed an invariant lineshape under the additional excitation and therefore no evidence of screening effects.

Furthermore, it should be noted, that the determination of $k_B T$ by a linear fit to the high-energy side of the logarithmically plotted PL spectra yields a slope corresponding to a temperature of $T \approx 100$ K although the sample temperature during measurement was $T_S = 10$ K. This means that charge carriers cannot be described by a Boltzmann distribution. However, the fact that the shape of the low-energy side of the PL spectrum in Fig. 6.6(b) remains invariant for all excitation powers shows that carrier relaxation even towards the lowest energetic states is possible. This means that the shape of the high-energy side of the PL spectrum is mainly influenced by an energy-dependent density of states and not a hindered relaxation of carriers.

For comparison to reports in literature, the shift of the PL maximum $E_{\text{PL,max}}$ towards higher energies is quantified in Fig. 6.6(c) and shows an exponential increase with excitation power. $E_{\text{PL,max}}$ shifts by $\beta_{\text{DEC}} = 17$ meV per decade for low excitation powers. Similar results have been reported by Teixeira *et al.* for CZTS [79, 80]. As discussed in [79] this large shift towards higher energies cannot be caused by conventional DAP transitions with flat bands. It should be emphasized again, that the interpretation of the PL maximum alone could draw a misleading picture of the physics involved. The observation of an invariant lineshape of the low-energy side of the PL spectrum due to state-filling instead of a blue shift due to screening suggests that the PL is mainly influenced by band gap fluctuations instead of electrostatic potential fluctuations.

In order to determine whether the radiative transitions at low excitation powers involve defect levels or band states, the PL yield Y was analyzed depending on the excitation power L [167].

$$Y(L) \propto L^k \tag{6.5}$$

Figure 6.6(d) shows the corresponding double-logarithmic plot from which a value of $k = 0.8$ can be determined. According to Schmidt *et al.* this corresponds to a radiative transition involving one or more defect levels [167]. Hence, the observations are consistent with the assumption of transitions involving defect levels and fluctuating band edges. It should be noted that the shift of the PL maximum towards higher energies and the value of $k < 1$ is determined for a variation of the excitation power over four orders of magnitude. For even higher excitation powers additional contributions arise on the high-energy side of the PL spectrum which will be discussed in the following.

6.4.2 Comparison of Photoluminescence to Photoluminescence Excitation Spectra

In order to determine the origin of these additional contributions, PLE spectra were recorded for comparison. Figure 6.7(a) shows logarithmically-plotted PL spectra at two different excitation powers and a logarithmically-plotted PLE spectrum of a CZTSSe sample. The PL spectrum clearly shows a second contribution on the high-energy side for an increased nominal excitation power of $P = 78.62$ mW compared to a low nominal excitation power of $P = 1.08$ mW. The higher-energy contribution reaches into the tail of the PLE spectrum and coincides with the band gap as determined by ER which suggests a transition involving at least one band or band tail state.

The measurement data for high excitation power were fitted using 2 Gaussian functions and the fit results are shown in Fig. 6.7(b). The aim of this fit was not to perfectly capture the lineshape of the measured signal. Instead, it is used to estimate the energetic positions of the two individual contributions. The fit shows two contributions with center energies of $E_1 = 0.96$ eV and $E_2 = 1.06$ eV. Interestingly, E_2 coincides with the center of the modulus spectrum of the corresponding ER signal (dashed line, $E_{g,\text{ER}} = 1.05$ eV) within the uncertainty of the individual fit parameters and the accuracy of the measurements. Furthermore, this contribution to the PL signal is located in the tail of the PLE signal. This supports the conclusion that the high-energy contribution at E_2 involves a band or a band tail state whereas the low-energy contribution at E_1 is due to a defect-related transition.

It has to be emphasized that the results were obtained by using complementary techniques such as ER and PL or PLE and PL. This draws a more complete picture of radiative recombination in CZTSSe compared to other reports in literature which only apply one single technique such as PL. Furthermore, the results show that there are two aspects of radiative recombination in CZTSSe. First, there are defect levels which take part in radiative transitions and second, the presence of fluctuations of the band edges distributes these defect levels over a larger energy range due to the possibility of spatially indirect transitions.

The absence of screening phenomena in PL power series as well as the inhomogeneously broadened ER spectrum the width of which is not changing with temperature (compare Fig. 6.3(b)) suggest fluctuations of the band gap itself rather than electrostatic potential fluctuations.

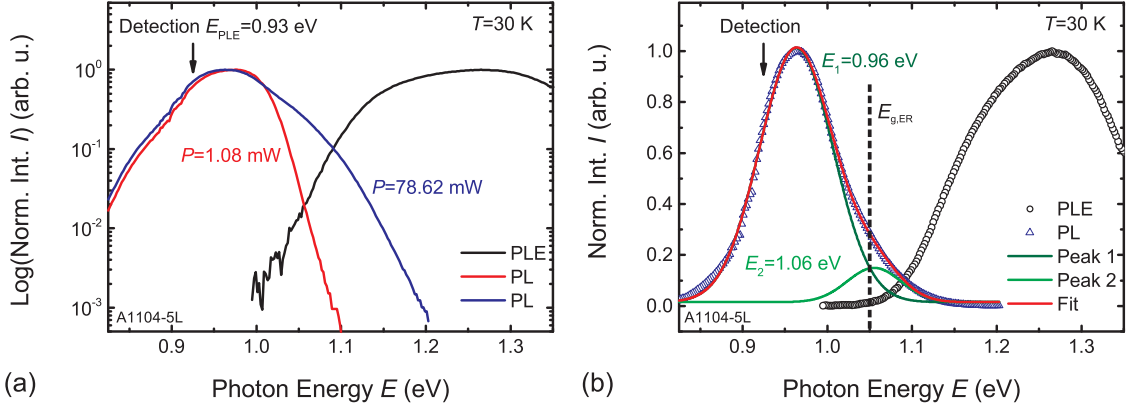


Figure 6.7: (a) Logarithmic PL and PLE spectra for low (red) and high (blue) PL excitation. For high excitation a second contribution to the PL spectrum emerges in the tail of the PLE (black) spectrum. (b) Normalized PL and PLE spectrum with two Gaussian peaks fitted to the PL spectrum. The low-energy contribution lies well below the band gap whereas the high-energy contribution coincides with the tail of the PLE spectrum and the band gap according to the corresponding ER measurement (dashed line) within the accuracy of the measurement. After [113, 152].

After the theoretical considerations of Mattheis *et al.* such band gap fluctuations have a decreasing effect on solar cell device performance [149] due to additional recombination of localized carriers which could account partly for the generally rather low device performance of CZTSSe solar cells.

Finally, a few remarks on PLE measurements should be made. For different PLE detection energies E_{PLE} different absorption models were fitted to recorded and corrected PLE spectra, in order to obtain an estimation for the band gap value. These fits involved the assumption of a Gaussian band gap distribution [48, 149] or a single exponential tail below the band gap [168]. The resulting values for E_g differed depending on the detection energy of the PLE spectrum. Furthermore, a common observation of all PLE experiments was that a higher detection energy E_{PLE} resulted in higher maximum PLE signal (PLE signals were corrected for the PL signal strength at the detection energy as well). This suggests that carrier relaxation plays an important role in the PLE signal of CZTSSe. Therefore, band gap values determined from PLE measurements have to be looked at with caution and the PLE signal is not only determined by the absorption of the absorber layer. Reliable insights into radiative recombination mechanisms of CZTSSe can only be gained if the results of all measurements – PL, PLE and ER – are taken into account.

6.4.3 Temperature-Dependent Photoluminescence

Generally, the interpretation of temperature-dependent PL spectra is often very difficult since a variation of the sample temperature modifies several factors at once such as carrier mobility as well as the occupation of the different energy levels and recombination paths. This is why only a very basic interpretation of the performed temperature-dependent measurements will be presented in the following.

An important implication of both electrostatic potential fluctuations as well as band gap fluctuations is a shift of the PL maximum towards lower energies with increasing temperature [156, 169], additionally to a possible shift of E_g . The temperature-dependence of the latter was investigated in this work using ER and it was shown that E_g increases by about $\Delta E_g = 0.02 \text{ eV}$ for an increase from $T = 10 \text{ K}$ to $T = 120 \text{ K}$ as shown in Fig. 6.3(a).

For a low excitation power of $P = 1.08 \text{ mW}$ a temperature-dependent PL measurement was performed. The low excitation power ensured that only one contribution to the PL signal was present. As already presented in the previous section a double-sigmoidal expression was used to determine the maximum of PL spectrum $E_{\text{max,PL}}$ of the individual PL spectra. The resulting temperature dependence of the PL spectra is shown in Fig. 6.8(a). For an increasing temperature the PL spectrum shifts towards lower energies which is consistent with the assumption of the generated carriers being able to reach energetically lower states. A second contribution to the PL spectrum arises for temperatures above 90 K on the high-energy side of the spectrum which suggests additional state-filling effects.

The temperature dependence of the maximum of the PL signal is shown in Fig. 6.8(b). Despite the increase in the band gap of $\Delta E_g = 0.02 \text{ eV}$ as determined by ER the maximum energy of the PL signal shifts by $\Delta E_{\text{max,PL}} = 0.03 \text{ eV}$ towards lower energies for an increase in the temperature from 10 K to 120 K. The slope of this decrease is $m_t = -2.5 \times 10^{-4} \text{ eV/K}$. This observed shift is consistent with the assumption of both electrostatic potential fluctuations and band gap fluctuations. Similar results in terms of this shift towards lower energies have been found for CIGS absorber layers by Dirnstorfer *et al.* [170]. An increase in the temperature leads to an increased carrier mobility which results in carriers finding deeper valleys in the band structure in order to recombine at lower emission energies. This red shift was observed for all investigated samples in this work and did not change within the accuracy of the measurements for a variation of excitation power or for a variation of the degree of Cu–Zn disorder in the absorber layer as discussed in the next chapter.

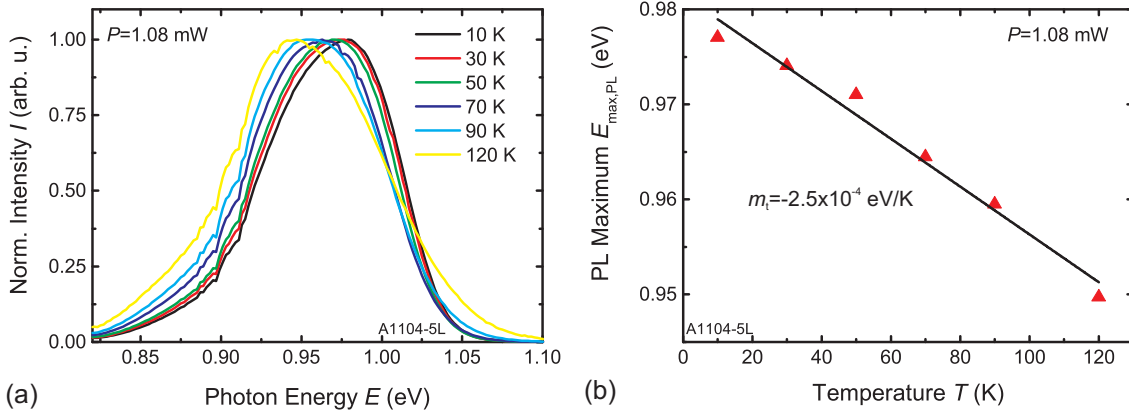


Figure 6.8: (a) Temperature-dependent PL spectra of a CZTSSe sample. The spectra show a shift of the PL signal towards lower photon energies but at the same time also a filling of energetically higher states. (b) Temperature dependence of the PL maximum $E_{\max, \text{PL}}$ as determined by a double-sigmoidal fit to the measurement data. The PL signal shifts towards lower photon energies despite a simultaneous increase in the band gap energy as determined by ER measurements.

It should be emphasized, however, that it is not possible to distinguish electrostatic potential fluctuations from band gap fluctuations in this measurement. The temperature-dependent measurements primarily show the presence of either one. Therefore, the findings are not contradictory to the suggestion of band gap fluctuations as the dominant mechanism in radiative recombination. On the contrary, no unambiguous evidence of electrostatic potential fluctuations could be found. The results underline that the entire PL spectrum needs to be analyzed and not only the energetic position of the PL maximum in order to shed light onto the underlying physics.

6.5 Summary

In this chapter it has been shown that the standard band gap determination method in the TFSC community – a Tauc plot of the low-energy side of an EQE spectrum – cannot be applied. This is partly due to the inhomogeneous broadening of the dielectric function as it was already discussed in section 5.5. In addition to that the assumption that the low-energy side of the EQE spectrum represents the absorption of the absorber layer is rather questionable. A comparison of EQE and ER spectra revealed that optically active states exist in the CZTSSe absorber layer which do not contribute to current transport.

In other words, this means that the optical band gap as determined by ER does not coincide with an electronic state of macroscopic mobility in the device.

Furthermore, the temperature-dependent band gap of the CZTSSe absorber layer in a TFSC was determined and showed an anomalous behaviour, similar to chalcopyrite materials. The reason for this behaviour lies in the band structure of CZTSSe. Due to the p–d hybridization in the formation of the VBs the contribution of lattice dilatation and electron–phonon interaction to the changes in the band gap energy compensate each other partially which first leads to an increase of E_g with temperature at low temperatures followed by a decrease for temperatures above 120 K.

Finally, by comparing power-dependent PL spectra to PLE and ER spectra, individual contributions to the PL spectra were identified in terms of defect-related luminescence and band- or band tail-related luminescence. Additionally, the absence of screening effects in power-dependent PL spectra suggest that band gap fluctuations due to structural disorder dominate in the investigated CZTSSe samples in contrast to electrostatic potential fluctuations.

Chapter 7

Assessment of the Role of Cu–Zn Disorder in $\text{Cu}_2\text{ZnSn}(\text{S},\text{Se})_4$

Recently, the so-called order–disorder transition in CZTSSe experienced an increasing amount of attention [171–175]. The term “order–disorder transition” denotes a thermally-induced cation reordering in the Cu–Zn lattice planes of the kesterite unit cell [171]. Cu–Zn disorder in the kesterite unit cell is connected with the occurrence of $[\text{Cu}_{\text{Zn}}+\text{Zn}_{\text{Cu}}]$ defect pairs [41]. These defect pairs could lead to electrostatic potential fluctuations which have been suggested by Gokmen *et al.* to be the dominant efficiency-limiting mechanism in CZTSSe solar cells [78]. In this chapter it will be shown that in contrast to that, a controlled manipulation of the degree of order within the Cu–Zn lattice planes corresponds to a continuous transition between two materials with different effective crystal structures and band gaps.

First, a brief overview on different efficiency-limiting factors in CZTSSe solar cells will be given. Then, the order–disorder transition will be introduced from a crystallographic point of view and a model for the qualitative description of the kinetics of Cu–Zn reordering processes will be presented. Furthermore, it will be shown that the band gap of the CZTSSe absorber is directly correlated with the degree of Cu–Zn disorder in the kesterite unit cell. This will be achieved by ER measurements to detect thermally-induced absorber band gap shifts in CZTSSe solar cells. The devices were still functional after the thermal treatments and hence the impact of Cu–Zn disorder on the solar cell performance could be assessed directly. However, it will be shown, that Cu–Zn disorder is not the main efficiency-limiting factor of kesterite solar cells.

Parts of the results of this chapter have been achieved in the Master’s theses of Christian Huber and Christian Zimmermann. Further details on this subject can

be found in the respective Master’s thesis [112, 113]. Furthermore, the results were published in [151, 176].

7.1 Efficiency Limitations of $\text{Cu}_2\text{ZnSn}(\text{S,Se})_4$ Solar Cells

Despite the similarity in their physical properties, CIGS and CZTSSe show large differences once it comes to finished solar cell devices. CIGS solar cells already represent a mature technology and achieve power conversion efficiencies of up to 21.7% [7]. In contrast to that, CZTSSe solar cells still lack in performance and the world record efficiency of only 12.6% [12] is not compensated economically by the use of earth-abundant constituting elements.

In order to improve CZTSSe devices, the main device performance-limiting mechanisms need to be identified first. Table 7.1 summarizes the J – V characteristics of recent CZTSSe and CIGS high-efficiency and world record solar cells. By comparing the individual device parameters it is obvious that the main reason for the lower efficiency of CZTSSe solar cells is their comparatively low open-circuit voltage V_{OC} . The corresponding figure of merit is the so-called V_{OC} deficit [12] which denotes the difference

$$\frac{E_{\text{g}}}{e} - V_{\text{OC}}.$$

The devices in Tab. 7.1 all exhibit similar absorber band gaps and although they were determined by means of an EQE measurement the error of the measurement cannot account for the systematically larger V_{OC} deficit of CZTSSe solar cells by approximately 200 mV.

The main reason for an insufficient V_{OC} is carrier recombination which can occur at different locations in solar cells. One possibility is carrier recombination at the buffer–absorber interface which has been shown for CZTSSe solar cells by means of J – V – T -measurements [177, 178]. The results suggest a non-ideal band alignment between the absorber layer and the CdS buffer. In contrast to that, band gap fluctuations in the absorber material lead to carrier localization and recombination in the bulk and also lower V_{OC} . Such models have been proposed for CIGS and were investigated by means of photoluminescence spectroscopy [48, 149]. The results of chapter 6 suggest such band gap fluctuations in CZTSSe solar cells as well.

7.2 Controlling Cu–Zn Disorder in the $\text{Cu}_2\text{ZnSn}(\text{S},\text{Se})_4$ Unit Cell

Table 7.1: Device characteristics of different record solar cells for both CZTSSe and CIGS absorber layers. In the case of CZTSSe solar cells the main performance-limiting factor is the low open-circuit voltage in comparison to the band gap of the respective absorber layer. Excerpts from device characteristics taken from [7, 12, 84, 146]. Band gap values estimated from EQE measurements.

| Device | η (%) | V_{OC} (mV) | J_{SC} (mA/cm ²) | FF (%) | $\frac{E_{\text{g}}}{e} - V_{\text{OC}}$ (mV) |
|--------------|------------|----------------------|---------------------------------------|--------|---|
| CZTSSe (IBM) | 12.6 | 513 | 35.2 | 69.8 | 617 |
| CZTSSe (ZSW) | 10.3 | 471 | 31.6 | 69.6 | n/a |
| CIGS (ZSW) | 21.7 | 746 | 36.6 | 79.3 | 384 |
| CIGS (EMPA) | 20.4 | 736 | 35.1 | 78.9 | n/a |

The strong tailing observed in the EQE of CZTSSe solar cells is seen as the fundamental reason for the insufficient power-conversion efficiency [78]. A similar aspect was discussed in section 6.1 – the existence of optically active states which do not contribute to current transport.

In a highly compensated semiconductor such as CZTSSe charged defect pairs cause fluctuating band edges. As it was discussed in subsection 2.1.3 the defect pairs most likely to occur in kesterite materials are $[\text{V}_{\text{Cu}}+\text{Zn}_{\text{Cu}}]$ and $[\text{Cu}_{\text{Zn}}+\text{Zn}_{\text{Cu}}]$ defect pairs. While the first one is almost exclusively determined by the composition of the absorber layer, it was shown that the density of the latter defect pair can be controlled by thermal treatments which will be subject to the following sections.

7.2 Controlling Cu–Zn Disorder in the $\text{Cu}_2\text{ZnSn}(\text{S},\text{Se})_4$ Unit Cell

As discussed in subsection. 2.1.3, the formation of defect pairs in CZTSSe is favored over the formation of point defects due to their charge-neutrality. Since of the two prevailing defect pairs only $[\text{Cu}_{\text{Zn}}+\text{Zn}_{\text{Cu}}]$ does not change the sample composition the following discussion will focus on this defect pair.

The occurrence of Cu–Zn disorder in the kesterite unit cell was already the subject of a neutron diffraction study by Schorr [41]. Schorr found the kesterite crystal structure as the stable configuration for both $\text{Cu}_2\text{ZnSnS}_4$ and $\text{Cu}_2\text{ZnSnSe}_4$. Especially for the pure selenide it was not clear whether the kesterite or the stannite crystal structure represents the ground state of the material. However, a significant disorder in the Cu–Zn lattice planes was detected and it was pointed out that the

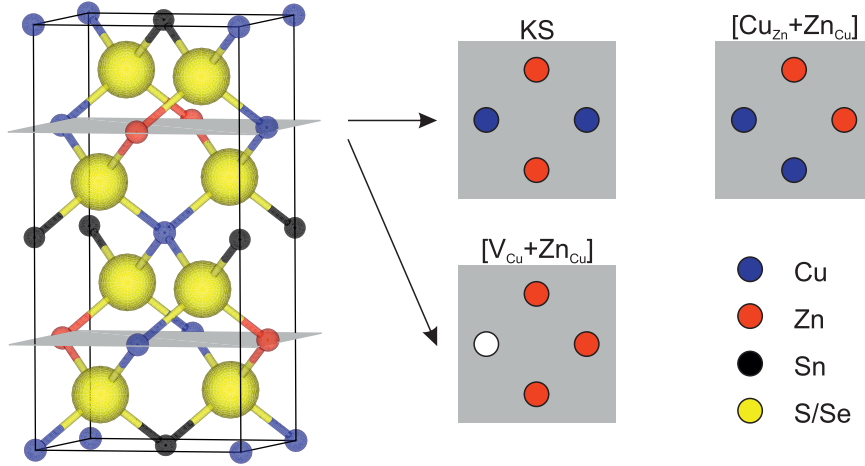


Figure 7.1: Illustration of the two most common neutral defect pairs in the Cu–Zn planes (grey) of the kesterite (KS) unit cell. While the abundance of $[\text{V}_{\text{Cu}}+\text{Zn}_{\text{Cu}}]$ defect pairs is almost exclusively governed by sample composition, the occurrence of $[\text{Cu}_{\text{Zn}}+\text{Zn}_{\text{Cu}}]$ defect pairs can be manipulated by a thermal treatment of the material.

degree of disorder depends on the thermal treatment of the sample during fabrication. Figure 7.1 shows the kesterite unit cell with the Cu–Zn planes marked in grey. Furthermore, it shows the most abundant neutral defect pairs and the connection of $[\text{Cu}_{\text{Zn}}+\text{Zn}_{\text{Cu}}]$ defect pairs to Cu–Zn disorder in the CZTSSe unit cell. It should be emphasized again that the terms “order” and “disorder” only refer to the arrangement of Cu and Zn atoms within the Cu–Zn lattice planes of the kesterite unit cell. The formation of the most abundant defect pairs involves two mechanisms. In the case of the $[\text{V}_{\text{Cu}}+\text{Zn}_{\text{Cu}}]$ defect pair a vacancy defect as well as an antisite defect have to form whereas for the $[\text{Cu}_{\text{Zn}}+\text{Zn}_{\text{Cu}}]$ defect pair two antisites are necessary. In the case of CZTS it has been shown by means of DFT that the involved point defects have an impact on the band edges of the material if present abundantly [77].

In order to describe the kinetics of the formation and dissociation of the defect pairs qualitatively, the stochastic Vineyard model [179] will be introduced in the following.

7.2.1 Cu–Zn Disorder Kinetics – The Vineyard Model

Vineyard derived a model for the kinetics of order–disorder transitions for the formation of vacancies and antisites in binary cubic (b.c.c. and f.c.c) lattices which is the basis for the discussion in this subsection [179]. It should be mentioned that the

model qualitatively yields the same predictions for both a vacancy and an antisite defect. However, since the scope of this chapter is the formation of $[\text{Cu}_{\text{Zn}}+\text{Zn}_{\text{Cu}}]$ antisite defect pairs the discussion will focus on the formation of the latter.

In order to describe the degree of order in the Cu–Zn planes of the kesterite unit cell, it is necessary to introduce the so-called long-range order parameter S [180]:

$$S = \frac{r_\alpha - f_A}{y_\beta} = \frac{r_\beta - f_B}{y_\alpha}. \quad (7.1)$$

Within the Vineyard model for a binary compound there are two types of lattice sites α and β for atoms of type A and B , respectively. $r_{\alpha,\beta}$ denotes the respective fraction of lattice sites α and β which are actually occupied by atoms of type A and B , respectively. $f_{A,B}$ denotes the fraction of the individual atoms in the compound. $y_{\alpha,\beta}$ denotes the respective fraction of available lattice sites of type α and β . In the case of perfectly ordered Cu–Zn planes in the kesterite unit cell, the long-range order parameter would take a value of $S = 1$ whereas a random distribution of Cu and Zn atoms would correspond to $S = 0$.

$\text{Cu}_2\text{ZnSn}(\text{S},\text{Se})_4$ does not represent a simple cubic semiconductor, however, similar circumstances to those considered in the Vineyard model are given. The Cu–Zn planes represent a two-dimensional cubic subcell thus making at least a qualitative application of the Vineyard model possible as it was also pointed out by Rey *et al.* [174]. Still, there are a few remarks to be made. Since the investigated CZTSSe absorber layers in this work and generally application-relevant absorber layers are off-stoichiometric [181] it is not possible to achieve a value of the long-range order parameter of $S = 1$. Instead the maximum value of this parameter will be $S_{\text{max}} < 1$, however, this will be neglected for simplicity. Additionally to that, since the Cu–Zn planes only represent a subcell of the kesterite unit cell the Vineyard model can only be used for qualitative considerations.

For the case of the interchange of two atoms in the lattice, Vineyard derived a differential equation for the temporal evolution of S [179]:

$$\frac{dS}{dt} = \frac{1}{f_B} \left[\underbrace{K_O f_A f_B (1 - S)^2}_{\text{ordering process}} - \underbrace{K_D (f_A + f_B S) (f_B + f_A S)}_{\text{disordering process}} \right]. \quad (7.2)$$

The formation or dissociation of the $[\text{Cu}_{\text{Zn}}+\text{Zn}_{\text{Cu}}]$ antisite defect pair corresponds to such a process and the corresponding kinetics can therefore be described qualitatively by this differential equation. K_O and K_D represent rate coefficients of the ordering and disordering process the origin of which will be discussed later in this section.

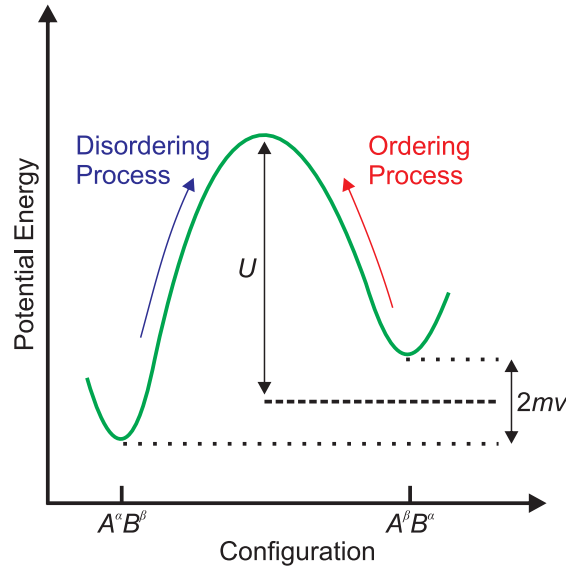
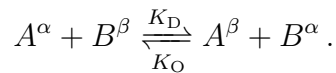


Figure 7.2: Potential energy governing the ordering and disordering process. The ordered configuration $A^\alpha B^\beta$ and the disordered configuration $A^\beta B^\alpha$ are separated by a barrier U and have an energetic difference of $2mv$, m depending on the degree of order in the environment and v being a characteristic energy of the system. Depending on the degree of order in the environment, the activation energies for the ordering and disordering process change. After [179].

Vineyard pointed out that eq. 7.2 describes an equilibrium reaction of the form



The equilibrium is established between two competing processes, an ordering and a disordering process with respective activation energies depending on the value of S . Figure 7.2 schematically shows the potential energy which is governing the above-mentioned exchange reaction. The two atomic configurations $A^\alpha B^\beta$ and $A^\beta B^\alpha$ are separated by a potential barrier U . The energetic difference between the initial and final atomic configuration is $2mv$ with v being a characteristic exchange energy of the lattice and m depending on the atomic environment surrounding the atoms A and B , in particular depending also on S . For a decreasing value of S the potential energy of the valley on the right-hand side of Fig. 7.2 is increased and the potential on the left-hand side is decreased – the potential becomes more asymmetric. This increases the activation energy for the disordering process and lowers the activation energy of the ordering process which will lead to a different equilibrium value of S depending on the temperature.

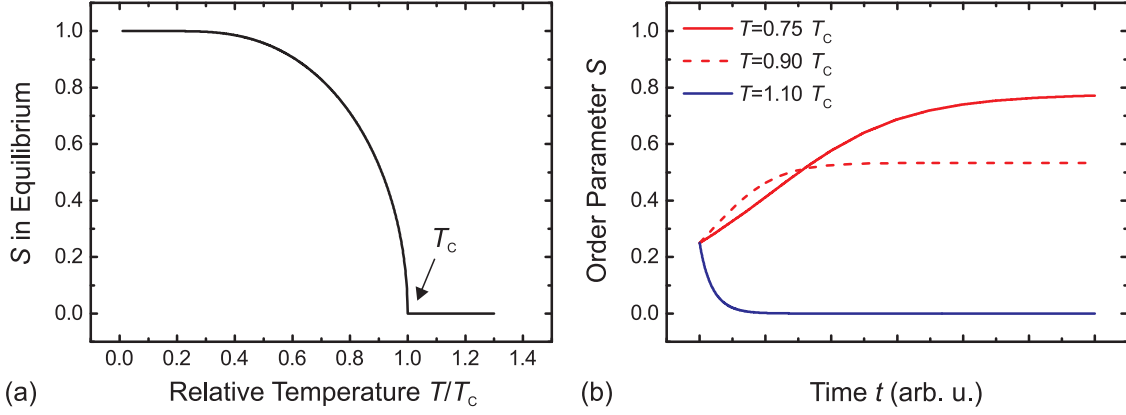


Figure 7.3: (a) Calculated temperature dependence of the long-range order parameter S according to the Vineyard model for an antisite defect. A characteristic temperature T_C exists above which the system is entirely disordered. (b) Calculated temporal evolution of the order parameter S . Both the timescale and the final stationary value of S depend on the ratio T/T_C . Taken from [112] and formatted.

Vineyard derived expressions for the rate coefficients K_O and K_D for a binary compound with a b.c.c. lattice [179]:

$$K_{O/D} = 8\nu \exp\left(\frac{-U \pm 7vS}{RT}\right). \quad (7.3)$$

In this equation, ν represents the characteristic hopping rate of the atoms. For a different type of lattice, similar expressions can be found and yield qualitatively analogous expressions for K_O and K_D [174,179]. Based on eqs. 7.2 & 7.3 it is possible to determine the equilibrium value of S for a given temperature T by searching for the stationary condition $dS/dt = 0$. Figure 7.3(a) shows the calculated thermal equilibrium value of S for different temperatures T . An important implication of the Vineyard model is the existence of a critical temperature T_C above which the system is entirely disordered ($S = 0$). In the case of CZTSSe this corresponds to a random distribution of the Cu and Zn atoms within the Cu–Zn lattice planes independent of the lattice sites which are assigned to them by the kesterite space group $I\bar{4}$.

Furthermore, the Vineyard model allows to calculate the temporal evolution with which the system establishes thermal equilibrium at a given temperature and a given initial long-range order S_0 . Figure 7.3(b) shows the calculated temporal evolution of S for three different temperatures for a starting value $S_0 = 0.25$. Whether an ordering or disordering process is taking place depends on T/T_C and so does the final value of S and the rate at which the system establishes thermal equilibrium. The

study of the timescale of these processes is particularly interesting for the fabrication of CZTSSe layers since it determines whether the results of this chapter can actually be applied to application-relevant processes.

7.2.2 The Order–Disorder Transition in Literature

At this point a brief review of the most relevant publications for this work will be given. This review does not claim completeness.

An abundant occurrence of the $[\text{Cu}_{\text{Zn}}+\text{Zn}_{\text{Cu}}]$ antisite defect pair in kesterite materials was predicted by DFT calculations and has been known for several years now [35,77]. As already discussed, experimental evidence of this circumstance has been provided by Schorr [41].

Paris *et al.* showed that it is possible to manipulate the degree of Cu–Zn disorder by using appropriate thermal treatments [175]. They used solid-state nuclear magnetic resonance (NMR) measurements as well as resonant Raman scattering to investigate CZTS powder samples. It was shown that the cool-down process the sample is subject to has a severe impact on the Cu–Zn disorder. Furthermore, Paris *et al.* were able to show that the degree of Cu–Zn disorder is correlated to the relative intensity of certain Raman modes in the investigated CZTS samples.

Scragg *et al.* investigated the same types of samples using resonant Raman scattering and employed the stochastic Vineyard model to determine the critical temperature T_C of CZTS to be 260°C [171]. Furthermore, the term order–disorder transition was introduced to denote the phase transition in the Cu–Zn planes in the CZTS unit cell. The comparatively low critical temperature of the order–disorder transition shows that such phenomena can be relevant for the fabrication of kesterite solar cells since typical chalcogenization or formation temperatures of the films are far above T_C .

Gershon *et al.* suggested that a detailed study of thermal post-processing of solar cells could help to reduce the band tailing and thus the V_{OC} deficit of CZTSSe solar cells [182]. The authors directly related Cu–Zn disorder to this phenomenon and, furthermore, underlined the importance of a study of the device performance after such annealing processes.

Huang and Persson calculated band gaps for CZTS layers with a high density of V_{Cu} as well as Zn_{Cu} and Cu_{Zn} [77]. The results suggested that an abundant presence of these defects alters the local band structure. Especially VB states are strongly modified due to the participation of Cu-d orbitals in their formation.

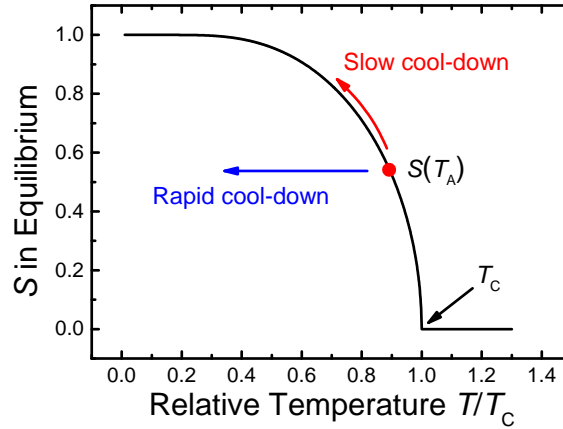


Figure 7.4: Long-range order parameter S in thermal equilibrium versus temperature. For a given equilibrium value $S(T_A)$ a rapid cool-down to room temperature corresponds to a horizontal transition (blue) which represents the conservation of the respective value $S(T_A)$. A slow cool-down from a temperature T_A (red) allows the system to establish thermal equilibrium and hence effectively increase S . Taken from [151] and formatted.

Rey *et al.* used transmission measurements to detect such band gap shifts due to thermal treatments of CZTSe samples on glass substrates and showed the correlation between the long-range order parameter S and the optical band gap of CZTSe [174].

ER represents an ideal technique to study the above-mentioned correlation of S and E_g . Furthermore, it can be used to study order–disorder related phenomena in entire CZTSSe solar cells which was not done before this work. In the following, a brief overview on the performed thermal treatments and their effect on S according to the Vineyard model will be given.

7.2.3 Post-Annealing of Solar Cells

In order to perform post-annealing treatments, a rapid thermal processing (RTP) tube furnace was used. The system was constructed and built by Timo Musiol. Technical details can be found in the corresponding Master’s thesis [183]. The samples were placed inside a graphite box and the annealing procedures were performed in a nitrogen atmosphere of 250 mbar.

In this work two different kinds of annealing procedures were employed. The only difference between them is the cool-down process. In the following, the effect of the annealing processes on the Cu–Zn disorder will be discussed in the context of the Vineyard model. Figure 7.4 shows the equilibrium curve of the long-range order

parameter $S(T)$. For a given temperature T_A above room temperature and a given long-range order parameter $S(T_A)$ a rapid cool-down to room-temperature leads to a freeze-out of $S(T_A)$. Therefore, a rapid cool-down corresponds to a horizontal transition (blue) in Fig. 7.4. In this work the rapid cool-down was realized by switching off the furnace, taking the sample out of the furnace and cooling it in a stream of air. This led to a cool-down of the sample from an annealing temperature T_A to room temperature in less than five minutes.

In contrast to that, a slow cool-down (at a sufficiently slow rate of 3 K/h) to room temperature (RT) allows the sample to establish a value of S close to thermal equilibrium $S(T)$ and thus follow the equilibrium curve in Fig. 7.4 approximately. This path (red) leads to a resulting value of roughly $S(RT)$ – or at least to the maximum value achievable at room temperature. These two different annealing procedures were applied to study the order–disorder transition in CZTSSe solar cells and the results will be shown in the following. Further details and modifications to the procedures will be provided, if necessary.

7.3 Order–Disorder Related Band Gap Changes

In this section it will be shown explicitly that the degree of Cu–Zn disorder (and therefore S) influences the band gap of the CZTSSe absorber layer. Furthermore, the critical temperature of the order–disorder transition will be determined and the findings regarding the temporal evolution of the band gap during annealing experiments will be presented.

7.3.1 Detection of Reversible Band Gap Changes Using Electroreflectance

As discussed in the previous section an important part of the post-annealing procedure of CZTSSe TFSCs is the cool-down process. Therefore, the first experiment which was performed regarding the investigation of the order–disorder transition was an annealing of a CZTSSe solar cell at 210 °C for 2 h followed by a slow cool-down (3 K/h) as discussed in the previous subsection. Remarkably, the devices were still functional after the procedure which made an investigation using ER possible. As will be shown later, the chosen temperature is above the critical temperature T_C of CZTSSe¹. According to the Vineyard model, the slow cool-down allows the system to establish a value of S close to the equilibrium value $S(RT)$ as discussed in the

¹In this study the sulfur content of CZTSSe is $y \approx 0.08$.

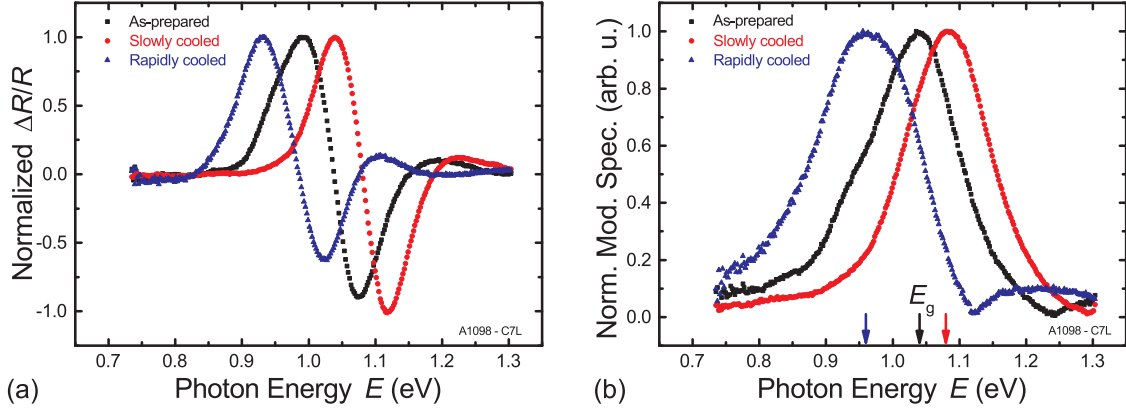


Figure 7.5: (a) ER spectra of a solar cell as-prepared (black) and after two post-annealing processes. The cell was heated to 210 °C and then cooled slowly (3 K/h, red curve) to room temperature. Afterwards the sample was again heated to 210 °C and cooled-down rapidly (blue curve) to room temperature. (b) The corresponding modulus spectra reveal a band gap increase from the as-prepared state ($E_g = 1.04$ eV) to the slowly cooled state ($E_g = 1.08$ eV) and a decrease from the as-prepared state to the rapidly cooled state ($E_g = 0.96$ eV). Taken from [151] and formatted.

previous subsection. Figure 7.5(a) shows the ER spectra of the as-prepared solar cell (black) before thermal treatment and the solar cell after slow cool-down (red). From the corresponding modulus spectrum (b) an increase in the absorber band gap from $E_g = 1.04$ eV (as-prepared) to $E_g = 1.08$ eV (slowly cooled) is evident². Considering the predictions of the Vineyard model [179], the experimental findings in [171, 175] and the predictions from DFT calculations [77] it can be concluded that a reduction of the Cu–Zn disorder corresponds to an increase of the absorber band gap.

Afterwards, the same sample was annealed at 210 °C for 2 h followed by a rapid cool-down. As discussed in the previous section, the rapid cool-down freezes the completely Cu–Zn disordered state of the CZTSSe layer in the TFSC since $T_A \geq T_C$ (this will be shown explicitly in the next subsection). Figure 7.5(a) shows the ER spectrum of the rapidly-cooled solar cell (blue). From the modulus spectrum (b) a decrease in the absorber band gap down to $E_g = 0.96$ eV can be determined.

Furthermore, an analysis of the full width at half maximum (FWHM) of the individual modulus spectra was performed. For a transition from the state of maximum Cu–Zn order (slow cool-down) to the state of maximum Cu–Zn disorder (rapid cool-down) the FWHM increases from 0.15 eV to 0.18 eV. Due to the discussion in section 5.5 not the absolute number but the increase of the broadening parameter

²Peak positions were determined by fitting a Gaussian to the modulus spectrum, see section 5.5.

should be mentioned. This suggests that Cu–Zn disorder plays a role in the inhomogeneous broadening of ER spectra of CZTSSe TFSCs, however, it is not the dominant contribution to inhomogeneous broadening in ER spectra.

The findings underline that Cu–Zn disorder is directly connected to the optical band gap of the CZTSSe layer. In the following, it will be shown that the change in the band gap of the absorber layer ΔE_g is a measure for the change in the long-range order parameter ΔS and the critical temperature T_C of the order–disorder transition of the investigated CZTSSe solar cell absorbers will be determined.

7.3.2 Determination of the Critical Temperature of the Order–Disorder Transition

A peculiarity of the order–disorder kinetics in the Vineyard model is the existence of a critical temperature T_C above which the Cu–Zn sites are randomly occupied which has been shown experimentally for CZTS by Scragg *et al.* [171]. The results of the previous subsection suggest a direct correlation between the long-range order parameter S and the absorber band gap E_g . Therefore, further post-annealing experiments were performed in order to determine whether E_g follows the behavior of S regarding the occurrence of a critical temperature. The experiments consisted of an annealing procedure with a fixed dwell time at a given temperature T_A followed by a rapid cool-down. The experiments were conducted for two samples using different annealing durations. Figure 7.6(a) shows the schematic principle of the experiments. The long-range order parameter at the annealing temperature is frozen-out by the rapid cool-down and hence different values $S(T_A)$ can be probed by the experiments by successively increasing T_A . Figure 7.6(b) shows the resulting band gap values for this experiment. It is evident that the change in band gap energy ΔE_g follows the change in the long-range order parameter ΔS . This confirms the findings of Rey *et al.* for CZTSe layers on glass and more importantly shows, that such post-annealing procedures can be applied to entire solar cells to precisely adjust the absorber band gap.

The critical temperature of the transition can be determined at the kink of Fig. 7.6(b) as

$$T_C = 195 \pm 5^\circ\text{C}.$$

The uncertainty of the determined values is given by the density of data points which were recorded. The observed band gap shifts turned out to be reversible. To show this explicitly, a sample was annealed alternatingly at a temperature $T_1 = 210^\circ\text{C} > T_C$ and $T_2 = 130^\circ\text{C} < T_C$ for 4 h each followed by a rapid cool-down.

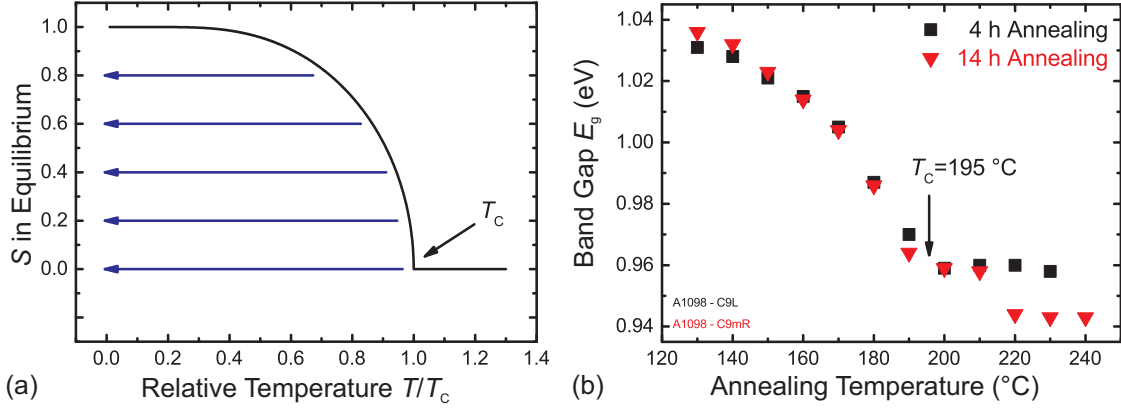


Figure 7.6: (a) Schematic principle of the determination of the critical temperature T_C . The sample is annealed for a fixed period of time at a given temperature T_A followed by a rapid cool-down to freeze the respective state of order $S(T_A)$. The critical temperature T_C is marked by the kink of the equilibrium curve $S(T)$. (b) Dependence of the absorber band gap after annealing at different temperatures T_A followed by a rapid cool-down. It is evident, that the change in the band gap ΔE_g follows the change ΔS . A critical temperature of 195°C can be determined. Above 220°C an additional irreversible band gap decrease occurs for longer annealing durations. Taken from [151] and formatted.

The result of this experiment is shown in Fig. 7.7 and clearly shows the reversibility of the ordering and disordering process with respect to the band gap E_g . This reversibility is a central argument why the band gap changes are actually order–disorder related and not caused by diffusion of elements in, e.g., the buffer–absorber region of the devices.

However, for longer dwell times (14 h) at increased temperatures ($T_A \geq 220^\circ\text{C}$) an additional decrease of the band gap of 0.02 eV can be found in Fig. 7.6(b). This additional shift turned out to be irreversible. The sample was annealed once more together with other control samples employing a slow cool-down procedure to reestablish the maximum band gap value. The sample showed a maximum band gap value of 1.04 eV which was 0.02 eV below the average band gap value of the control samples which were annealed simultaneously. This irreversible change could be attributed to elemental diffusion at the buffer–absorber interface, e.g., Cd diffusion which could cause a lowering of the band gap through the formation of $\text{Cu}_2(\text{Zn,Cd})\text{Sn}(\text{S,Se})_4$ [58].

The determined critical temperature of $T_C = 195 \pm 5^\circ\text{C}$ lies closer to the value for CZTSe ($T_C = 200 \pm 20^\circ\text{C}$, [174]) than to the value for CZTS ($T_C = 260 \pm 10^\circ\text{C}$, [171]). This is probably due to the low sulfur content within the investigated samples (sulfur content $y \approx 0.08$). It should be noted that the observed maximum band gap

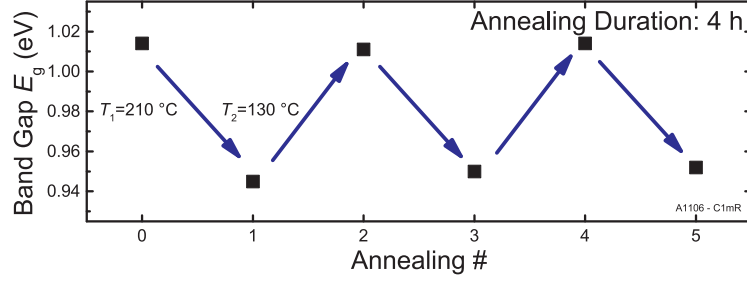


Figure 7.7: Evolution of the band gap value for a sample which was annealed alternately at $T_1 > T_C$ and $T_2 < T_C$ for 4 h followed by a rapid cool-down. The measured band gap changes are reversible. Annealing #0 refers to the as-prepared state of the sample. Taken from [151] and formatted.

value does not correspond to the maximum achievable long-range order parameter S_{\max} according to the Vineyard model. Considering the determined transition temperature, room temperature can be estimated to be approximately $0.64T_C$. At this temperature the equilibrium order parameter $S(RT)$ is not equal to the maximum achievable order parameter. This suggests that the band gap of an ideal kesterite crystal structure is even larger than the values reported in literature. In contrast to that, Cu–Zn disorder is maximized for samples which underwent an annealing above the critical temperature followed by a rapid cool-down. For those samples the condition $S = 0$ actually holds and can be observed at room temperature due to the small ordering rate at this temperature.

For lower annealing temperatures deviations of the band gap values become visible for different annealing periods in Fig. 7.6(b). These deviations suggest that the timescale at which the system establishes thermal equilibrium is in the order of hours. This temporal evolution will be investigated in the following.

7.3.3 Temporal Evolution of the Band Gap During Post-Annealing Experiments

In order to study the dynamics of the Cu–Zn reordering process, a sample was put into a state of maximum Cu–Zn disorder first. Afterwards it was repeatedly annealed for two hours at a temperature of $T_2 = 130^\circ\text{C}$ terminated by a rapid cool-down followed by a measurement of the band gap by ER. The same experiment was repeated but with an annealing temperature of $T_3 = 170^\circ\text{C}$. The Vineyard model predicts an ordering rate at which the system establishes the thermal equilibrium value which, amongst other factors, depends on the annealing temperature T_A . As discussed in

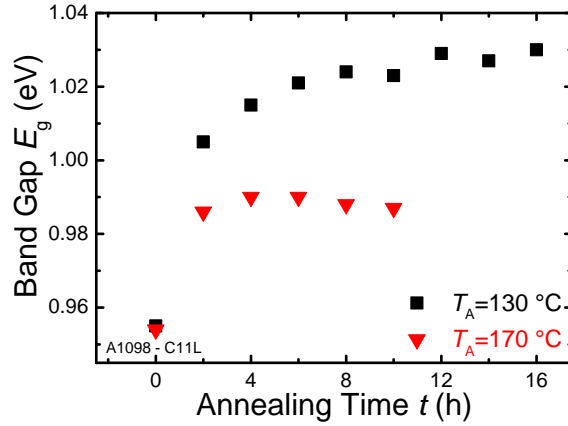


Figure 7.8: Temporal evolution of the band gap for two different annealing temperatures starting from a Cu–Zn disordered state. Both the final value and the timescale of the ordering process depend on the annealing temperature T_A . Typical timescales of the ordering process are in the order of hours. Taken from [151] and formatted.

subsection 7.2.1, the final value of S and thus E_g depend on the annealing temperature T_A . Figure 7.8 shows the resulting temporal evolution of the band gap in these experiments. As expected from the Vineyard model, both the timescale and the equilibrium value of E_g depend on the annealing temperature T_A . It is obvious that the ordering process is taking place on a timescale in the order of hours for the two annealing temperatures which were used in the experiments. For even lower annealing temperatures T_A the timescale of the ordering process increased rapidly. This explains the measured band gap value of solar cells in their as-prepared state which is lower than the maximum value of E_g observed for a slow cool-down. At room temperature the timescale of the ordering is too large so that effectively no increase in the band gap is observed after the fabrication of a solar cell even after days and weeks.

The observed timescale suggests that order–disorder-related phenomena can and should be taken into account in the fabrication procedure of CZTSSe layers, in particular the chalcogenization step – given they actually influence the performance of CZTSSe solar cells. The impact of order–disorder-related band gap changes on solar cell performance will be the subject of the next section.

7.4 Impact of Cu–Zn Disorder on Solar Cell Performance

In the previous sections the order–disorder transition was investigated in terms of the resulting band gap shifts and the correlations with the predictions of the stochastic Vineyard model were shown.

With the knowledge gained in this work, in particular in the previous sections an improved post-annealing procedure could be developed. The purpose of this procedure was to yield similar band gap increases while minimizing diffusion processes due to increased sample temperatures. While the ordering procedure in the previous sections comprised an initial disordering of the sample this step turned out to be redundant and is likely to favor unnecessary diffusion processes at the interfaces of the TFSC. Therefore, the samples were annealed at a temperature of only $T_A = 150^\circ\text{C}$ for 2 h followed by a slow cool-down of 2 K/h instead of 3 K/h – due to the smaller thermal difference. Fig. 7.9(a) schematically shows the annealing procedures which were used in the following taking into account the results of the previous sections. It is assumed that the Cu–Zn disorder in the as-prepared state is distinct from the equilibrium value of $S(RT)$. Considering the measured band gap values in the previous sections this is a realistic assumption. The disordering procedure which was used for these experiments was already described in subsection 7.2.3.

To study the influence of Cu–Zn disorder on solar cell performance, a series of 6 solar cells was post-annealed using the two described annealing procedures to increase and decrease Cu–Zn disorder alternately. It should be noted that the as-prepared band gap values were slightly larger than those of other CZTSSe solar cells in this work which is due to a slightly higher sulfur content y . In the following, the results presented are average values of the device parameters and their respective standard deviation.

Figure 7.9(b) shows the evolution of the open-circuit voltage after alternating thermal treatments which increase (ordered state) and decrease (disordered state) the band gap. For comparison the evolution of the corresponding band gap (average value) is shown as well. It is clearly evident that the change in the open-circuit voltage ΔV_{OC} follows the change in the band gap ΔE_g . For the last annealing step the difference between V_{OC} and E_g increases. This change went along with a significant decrease in the device efficiency due to a drop in short-circuit current which was certainly due to device degradation during the annealing process.

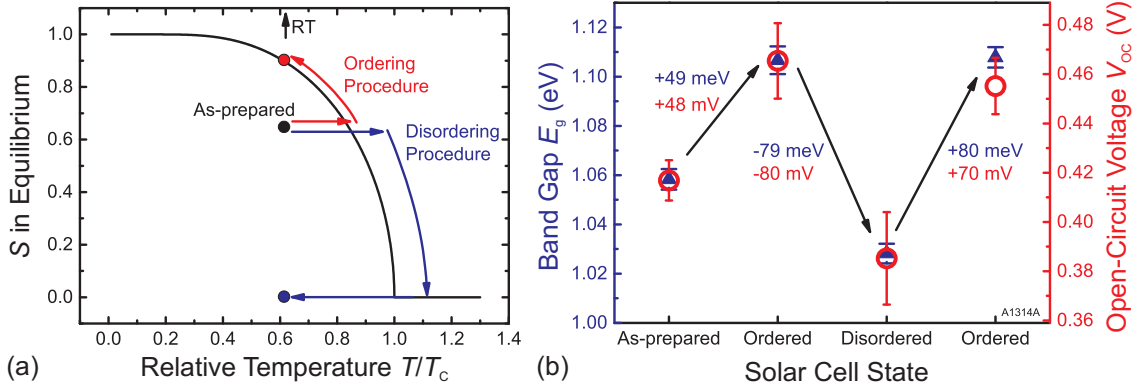


Figure 7.9: (a) Schematic of the post-annealing procedures which were used. The disordering procedure still consists of an annealing at 210 °C for 2 h followed by a rapid cool-down (blue) to room temperature. The improved ordering procedure (red) consists of an annealing at 150 °C for 2 h followed by a slow cool-down (2 K/h) to room temperature. (b) Evolution of the average open-circuit voltage V_{OC} (red) after the individual annealing procedures. ΔV_{OC} follows the change in the band gap (blue) ΔE_g thus excluding the order–disorder transition as a main performance limitation of CZTSSe solar cells. Error bars represent the standard deviation of the averaged values of E_g and V_{OC} . Taken from [176] and formatted.

It should be noted that the detected changes in the band gap of the CZTSSe absorber are reversible, even after multiple thermal treatments. However, this statement does not hold for all device parameters and device degradation was observed in the course of this work.

Table 7.2 summarizes the average device parameters after the individual annealing steps. The parameters after the last ordering procedure are omitted since the devices were not functional anymore due to a very low short-circuit current. From the as-prepared state to the first ordered state of the device a relative increase of the power conversion efficiency of about 22% is evident. However, this is not due to a reduction of the V_{OC} deficit. By comparison with Fig. 7.9(b) the band gap of the absorber is increased from 1.06 eV to 1.11 eV which is closer to the optimum band gap value according to the Shockley–Queisser limit [13]. Furthermore, an additional increase in the fill-factor suggests that a post-annealing procedure can have a beneficial impact on the series and parallel resistance of the devices.

However, the results summarized in Tab. 7.2 and Fig. 7.9(b) clearly show that the V_{OC} deficit $E_g/e - V_{OC}$ is invariant under a change in Cu–Zn disorder within the absorber layer. This is a central result of this chapter which sheds light on the role

Table 7.2: Summarized average device parameters and standard deviation for a series of 6 solar cells after different post-annealing procedures. Increases in efficiency for the ordered state are due to an increase in V_{OC} but also the fill factor (FF). Taken from [176] and formatted.

| Solar Cell State | η (%) | V_{OC} (mV) | I_{SC} (mA) | FF (%) |
|------------------|---------------|----------------------|----------------------|------------|
| As-prepared | 4.4 ± 1.2 | 417 ± 8 | 24 ± 3 | 43 ± 7 |
| Ordered | 5.4 ± 1.5 | 465 ± 15 | 23 ± 3 | 50 ± 7 |
| Disordered | 4.9 ± 1.0 | 385 ± 19 | 26 ± 2 | 49 ± 5 |

of the Cu–Zn disorder transition as a performance-limiting factor in CZTSSe solar cells. In contrast to the suggestions by Gershon *et al.* [182], Cu–Zn disorder is not at all a physical circumstance which is responsible for the large V_{OC} deficit. Instead, it should rather be seen as a means to tune the band gap of the absorber layer after or during fabrication.

7.5 Assessment of the Order–Disorder Transition in $\text{Cu}_2\text{ZnSn}(\text{S,Se})_4$

The results of this chapter have shed light onto the nature of abundant defects in $\text{Cu}_2\text{ZnSn}(\text{S,Se})_4$. Due to their abundance, $[\text{Cu}_{\text{Zn}} + \text{Zn}_{\text{Cu}}]$ antisite defect pairs cannot be considered as defect levels which are isolated from the band edges. Instead, the crystal structure of the material $\text{Cu}_2\text{ZnSn}(\text{S,Se})_4$ should be seen as an effective crystal structure as shown in Fig. 7.10. In the Cu–Zn planes at $z = 1/4$ and $z = 3/4$ (grey) two sorts of atoms are placed, however, they should rather be seen as two sorts of “effective” atoms which are a superposition of the electronic properties of Cu and Zn. Depending on the long-range order parameter S the admixture of both elements changes. Whereas the completely ordered ($S = 1$) state corresponds to the kesterite structure as described in subsection 2.1.1, a decrease in the long-range order parameter eventually leads to a purely random distribution of Cu and Zn atoms in the respective lattice planes and thus to a single type of effective atom. It should be noted that in this extreme case the crystal symmetry also changes [175]. Furthermore, it was discussed that the $S = 1$ state is not accessible in the experiment and instead, one should speak of a value of S_{max} .

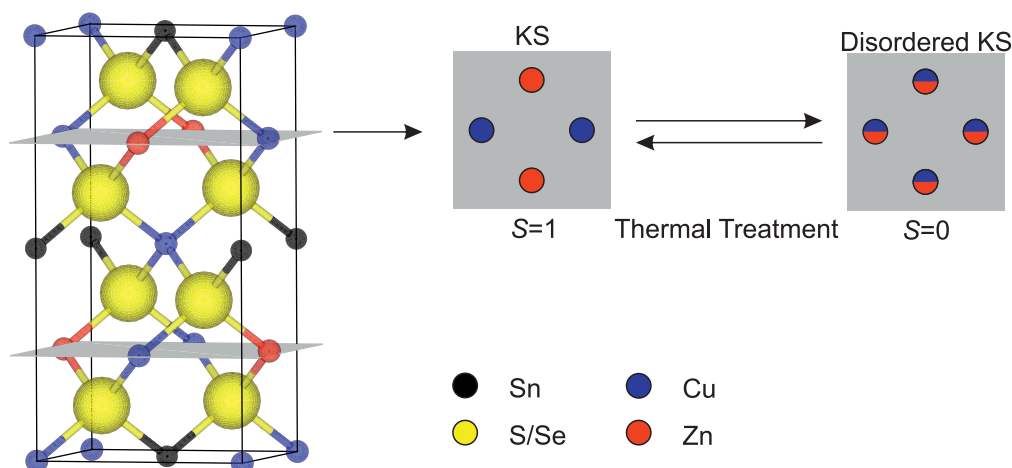


Figure 7.10: Effective crystal structure of CZTSSe depending on the long-range order parameter S . The kesterite (KS) structure corresponds to the Cu–Zn ordered state ($S = 1$) whereas a random distribution of Cu and Zn atoms ($S = 0$) corresponds to the disordered kesterite structure. The two effective crystal structures exhibit different band gaps. Thermal treatments allow to make a continuous transition between the two materials with different band gaps.

Thermal treatments of CZTSSe can be used to make a continuous transition between the two extremes of the crystal structure of $\text{Cu}_2\text{ZnSn}(\text{S},\text{Se})_4$ and thus the band gap. Since the activation energy of the order–disorder transition is rather low, its critical temperature is definitely exceeded during fabrication. Therefore, Cu–Zn disorder may certainly be one reason which accounts for the large scatter of reported band gap values of kesterite in literature, apart from different compositions and measurement methods [14]. The results of this chapter have shown that the band gap of $\text{Cu}_2\text{ZnSn}(\text{S},\text{Se})_4$ does not only depend on composition and fabrication but also on the thermal history of the sample.

Finally, one important practical aspect of the order–disorder transition should be mentioned. For CIGS the band gap is adjusted by varying the gallium content x of the absorber layer which can be conveniently implemented in a coevaporation process. In the case of CZTSSe the most common way to adjust the band gap is a variation of the chalcogenide ratio y as discussed in subsection 2.1.2. Since most application-relevant fabrication processes still employ a separate annealing step in a chalcogen atmosphere the adjustment of the band gap is technically more challenging if one is to keep all other composition parameters identical. However, the results of this chapter have shown that the order–disorder transition takes place on a timescale which can actually be taken into account during the chalcogenization step. This represents a very simple way to adjust the band gap precisely to a desired value.

7.6 Summary

In this chapter it has been shown that a thermally-induced cationic reordering in the Cu–Zn planes of the kesterite unit cell influences the band gap of the material. These reversible band gap shifts were detected by means of ER measurements and agree qualitatively with the predictions of the stochastic Vineyard model. In contrast to other reports in literature [171,174,175], entire CZTSSe solar cells were investigated and it could be shown that the effect of reversible band gap shifts is also present in finished devices. It could therefore be shown, that the change in the band gap of the absorber layer ΔE_g directly follows the change in the long-range order parameter ΔS .

The Vineyard model predicts a critical temperature which could be determined as $T_C = 195^\circ\text{C}$ for the investigated samples. Furthermore, it has been shown that the cation reordering takes place on a timescale in the order of hours. This shows that order–disorder related phenomena can be taken into account in chalcogenization processes since both T_C and the timescale are in a relevant order of magnitude.

Additionally, it has been shown that Cu–Zn disorder is not responsible for the large V_{OC} deficit of CZTSSe solar cells. From a comparative study of the band gap shift and solar cell performance it is evident that ΔV_{OC} is given by $\Delta E_g/e$. However, the order–disorder transition still represents an additional degree of freedom to tune the band gap of the absorber layer besides varying the composition of the absorber layer. Despite the invariant V_{OC} deficit order–disorder-related band gap changes still represent a means to increase the open-circuit voltage. The results have shown that a gain in open-circuit voltage is not necessarily accompanied by an compensating decrease in short-circuit current. As it was shown in this chapter, the power conversion efficiency of the CZTSSe devices could still be increased significantly although the Cu–Zn disorder is not main performance-limiting factor.

Future studies could suggest an optimum chemical composition of CZTSSe in terms of the possibility of a single-phase material. However, this composition may exhibit a band gap outside of the optimum band gap range according to the Shockley–Queisser limit [13]. In this case, a thermal treatment could be used to adjust the band gap to an improved or optimum value.

Chapter 8

Conclusions and Outlook

Conclusions of This Work

Due to the prospects of a sustainable and environmentally friendly electricity supply thin-film photovoltaics will certainly remain a vivid field of research in the near future. However, in order to commercialize technologies such as CIGS and CZTSSe further, several issues still need to be dealt with first. In the case of CZTSSe these issues are still quite fundamental and the elimination of the lack in power-conversion efficiency remains the most important factor deciding the fate of this technology.

In this work optical characterization techniques were used to gain insights into the fundamental physical properties of thin-film solar cells based on CIGS but mainly CZTSSe absorbers. A central aspect was the application of electroreflectance spectroscopy which turned out to be a very challenging task due to the nature of the investigated samples. By means of one-dimensional optical simulations it could be shown that measured electroreflectance spectra deviate from theoretically expected lineshapes due to three peculiar circumstances. First, a large built-in electric field is present in TFSCs and is increased by the modulating electric field which can lead to distortions which cannot be captured by standard evaluation techniques. Second, strong contrasts in the refractive indices of the individual functional layers as well as their thicknesses cause thin-film interferences which are not only visible in the reflection spectrum R but also the modulated reflectance spectrum $\Delta R/R$. It was shown that an increase in the degrees of freedom in order to capture the measured lineshape accurately can lead to artifacts which will in turn be mistaken for real optical transitions in the material. Third, the role of inhomogeneous broadening was investigated and it was shown that the lineshape of an ER spectrum is distorted in consequence. However, it was confirmed that standard evaluation techniques such

as Aspnes' third derivative functional form can be used to obtain a correct value of the average band gap in the case of a Gaussian distribution of band gaps.

In contrast to ER measurements in specular reflection, the detrimental effect of thin-film interferences could be significantly suppressed in ER spectra which are recorded using diffusely reflected light. The diffuse reflection is caused by surface roughness and interface roughness between the individual functional layers and such ER spectra can therefore be evaluated unambiguously. The underlying principle was shown by means of two-dimensional optical simulations. The broad applicability of ER using diffusely reflected light for the investigation of TFSCs has been demonstrated experimentally throughout this work.

In the case of CZTSSe, both the radiative excitation and recombination transitions were investigated using complementary optical spectroscopy techniques. In particular, power- and temperature-dependent photoluminescence spectroscopy confirmed that CZTSSe solar cells exhibit strong potential fluctuations. However, no evidence of electrostatic potential fluctuations as proposed by Gokmen *et al.* could be provided [78]. Instead, the results of this work rather suggest actual fluctuations in the band gap as it is evident by the large inhomogeneous broadening of the ER spectra and the pronounced tail of the corresponding photoluminescence excitation spectra. Furthermore, the latter were used to identify individual contributions to photoluminescence spectra. It could be shown that low-energy contributions to the PL signal are defect-related and very likely to be of a spatially indirect nature whereas high-energy contributions to the PL spectra actually involve band or band-tail states.

Finally, the role of Cu–Zn disorder as an efficiency-limiting factor in CZTSSe solar cells was investigated. It was shown that the absorber band gap of CZTSSe solar cells strongly depends on the degree of Cu–Zn disorder and can therefore be controlled using appropriate post-annealing procedures. The circumstance that the thermal treatments can be performed on finished solar cells allows for a subsequent adjustment of the absorber band gap after solar cell fabrication. However, the main performance limitation – the large V_{OC} deficit of CZTSSe solar cells remains untouched by Cu–Zn disorder. Still, significant increases in power-conversion efficiency of the corresponding solar cells could be achieved due to the possibility of a band gap adjustment over 0.12 eV to improve the overlap of the absorption spectrum of the CZTSSe layer and the solar spectrum.

The experimental technique of electroreflectance ran like a golden thread through this entire work and it will certainly not be the last time it is applied to TFSCs.

Future Work

As discussed several times within this work, the main performance limitation of kesterite solar cells is an insufficient open-circuit voltage. In order to find the central physical cause for this, radiative recombination processes can yield valuable insights into the material itself. A central aspect of future work has to be the identification of the radiative recombination channels in CZTSSe. The results of this work suggest the involvement of defect-related transitions, however, a discrete point defect or defect pair could not be assigned. A first step towards the solution of this problem would be a series with varying $[\text{Cu}]/([\text{Zn}]+[\text{Sn}])$ -ratios which additionally underwent different post-annealing treatments. These samples would differ in the concentrations of copper vacancies and $[\text{Cu}_{\text{Zn}}+\text{Zn}_{\text{Cu}}]$ antisite defects and a detailed photoluminescence study could show whether those defects are involved in the radiative recombination.

Additionally to the identification of the defects which are involved in radiative recombination the reason for band edge fluctuations has to be identified. Fluctuations in the degree of Cu–Zn disorder can account for band gap variations as shown in chapter 7. However, this is only one factor and with kesterite being a quaternary semiconductor with a very narrow single phase region, composition fluctuations can also lead to band gap fluctuations or the formation of secondary phases which exhibit similar band gaps as CZTSSe. ER can provide valuable insights in the dependence of the band gap of CZTSSe for varying chemical compositions of the material.

Furthermore, the above-named post-annealing treatments represent an additional degree of freedom in the fabrication of kesterite solar cells. Possibly, sample compositions with a formerly insufficient band gap value can now be made suitable in terms of the absorber band gap by an adjustment of the Cu–Zn disorder in the absorber layer. However, this requires detailed studies of the other consequences of Cu–Zn disorder. Since solar cell functionality not only requires a sufficient photon absorption but also carrier transport, it is of high importance to investigate the effects of the order–disorder transition on, e.g., carrier mobility and lifetime.

A topic which was not discussed in this work is the use of alternative buffer materials. So far, the entire layer sequence of a CZTSSe solar cells originates from a CIGS solar cell the absorber layer of which is replaced by a CZTSSe layer. However, it is not *a priori* clear whether the choice of CdS is the best and whether there is a favorable spike-like arrangement of the CB edges. The selection of different buffer and window layer materials can be supported by electroreflectance measurements since the modulation of the built-in electric field does not happen exclusively in the absorber layer but also in the buffer and window layer.

Especially buffer and window layers made of alloy semiconductors such as (Cd,Zn)S or Zn(O,S) can be well-characterized in terms of band gap and therefore alloy composition by using electroreflectance.

Still, recent improvements in the device efficiency emphasize the reduction of the band tailing as a key factor in future developments of kesterite solar cells [103,105]. Therefore, this should be the first criterion of optimization in the near future. Due to its working principle, electroreflectance is the ideal technique to detect optically active states of the absorber. Therefore, a comparison to spectrally-resolved transport measurements such as quantum efficiency can yield a suitable criterion for solar cell optimization.

Appendix A

Optical and Electronic Components of the Setups

As already mentioned in chapter 3 the optical components of the ER, PL and PLE setup are summarized in Tab. A.1.

In the case of the PL setup the choice of lenses was to ensure an optimum illumination of the detection monochromator (*Jobin-Yvon HR 640*) grating. In the case of the ER setup the lenses were chosen to yield a demagnifying imaging condition to focus as much light as possible onto the photodiode. Furthermore, the electrical components of the setups are summarized in Tab. A.2. The choice of these components was due to availability and experience from an earlier modulation spectroscopy setup as described in the PhD thesis of Andreas Grau. There are a few comments on measurement details and alignment tricks:

- Generally, the alignment was performed in order to yield exact imaging conditions in the ER setup. This means that the actual image of the monochromator exit slit is visible on the sample.
- Furthermore, typically used slitwidths of the 0.32 m focal length monochromator (*Jobin-Yvon Triax 320*) were 2–3 mm with a 600 l/mm grating. The slitwidth was verified not to be a resolution-limiting factor in the measurement.

In order to measure ER, the solar cell was mounted on the sample holder shown in Fig. A.1. A two-axis translation stage was used to precisely position the solar cell in the measurement spot. The back contact was connected to the holder using silver conductive paint. The solar cell itself was fixed using *Fixogum*. To contact the

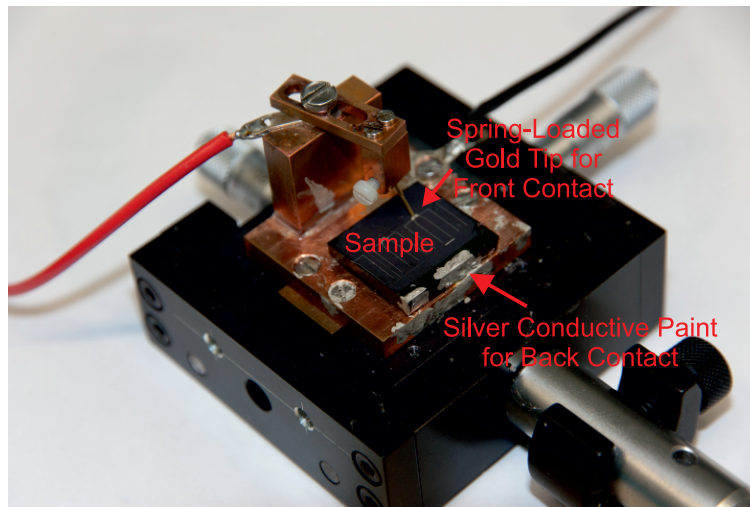


Figure A.1: Used sample holder for thin-film solar cells. The sample back contact is electrically connected to the holder using silver conductive paint. The front contact is connected using a spring-loaded gold tip. The tower and bridge connected to the gold tip are electrically isolated from the sample holder using a plastic plate.

metal grid or the window layer of the solar cell, a spring-loaded gold tip was used. Via cable connections the AC voltage in reverse bias was applied.

Table A.1: Optical components of the setups as denoted in chapter 3

| Component | Focal Length (mm) | Diameter (mm) | Comment |
|------------------|-------------------|---------------|-------------------|
| l L ₁ | 300 | 88.9 | Glass |
| L ₂ | 300 | 31.5 | Achromatic |
| L ₃ | 100 | 50.8 | Glass |
| L ₄ | 60 | 50.8 | Glass |
| L ₅ | 150 | 25.4 | Achromatic |
| L ₆ | 100 | 50.8 | Achromatic |
| L ₇ | 80 | 50.8 | Achromatic |
| L ₈ | 100 | 50.8 | Achromatic |
| L ₉ | 150 | 50.8 | Achromatic |
| L ₁₀ | 150 | 25.4 | Quartz |
| L ₁₁ | 75 | 25.4 | Glass |
| F ₁ | – | – | RG715/RG780/RG830 |
| F ₂ | – | – | RG715/RG780/RG830 |

Table A.2: Summary of the employed auxiliary components in the optical setups.

| Part | Manufacturer | Type | Comment |
|----------------------------|--------------------------------|------------------------|--|
| InGaAs Photodiode | Electro-Optical Systems Inc. | IGA-030-TE2-H | TE-cooled, used for ER/ER-T |
| Extended InGaAs Photodiode | Electro-Optical Systems Inc. | IGA(1.9)-030-TE2-H | TE-cooled, used for ER |
| InGaAs Photodiode | Electro-Optical Systems Inc. | DSS-IGA(1.9)-020L | LN ₂ -cooled, used for PL/PLE |
| Si/InAs Photodiode | Electro-Optical Systems Inc. | | TE-cooled, used for ER-T on CZTS |
| InGaAs Photodiode | Thorlabs | PDA255 | Intensity correction in PLE |
| Lock-In Amplifier | Princeton Applied Research | EG& G 5209 | Used in ER/PL/PLE/ER-T |
| Digital Multimeter | Keithley | Multimeter 2000 | Multimeter used in ER/ER-T/PLE |
| Chopper | Stanford Research Systems Inc. | Optical Chopper SR-540 | Optical Chopper, used for PL/PLE |
| Function Generator | Tektronix | AFG 3102 | Square-wave voltage |
| Function Generator | Agilent | 33220 A | Square-wave voltage |

Appendix B

Correction of PL and PLE Spectra

B.1 Correction of Photoluminescence Spectra

Since the measured PL spectra were very broad the measurement signals had to be corrected for the spectral responsivity of the InGaAs photodiode $R_{\text{IGA}}(\hbar\omega)$. Therefore, the quantum efficiency of the device Q_{IGA} was calculated using

$$Q_{\text{IGA}}(\hbar\omega) = \frac{1}{\hbar\omega R_{\text{IGA}}(\hbar\omega)}. \quad (\text{B.1})$$

The responsivity of the InGaAs diode was determined from the diode datasheet of the manufacturer. Based on this the correction function $K_{\text{IGA}}(\hbar\omega)$ is given by

$$K_{\text{IGA}}(\hbar\omega) = \frac{1}{Q_{\text{IGA}}(\hbar\omega)} \quad (\text{B.2})$$

and the measured PL signal $I_{\text{PL,meas}}(\hbar\omega)$ was multiplied by the correction function:

$$I_{\text{PL,corr}}(\hbar\omega) = I_{\text{PL,meas}}(\hbar\omega)K_{\text{IGA}}(\hbar\omega). \quad (\text{B.3})$$

An example PL spectrum with the corresponding corrected PL spectrum is shown in Fig. B.1(a).

B.2 Correction of Photoluminescence Excitation Spectra

The correction of measured PLE spectra was slightly more complicated since the measured signal had to be corrected for both the responsivity of the InGaAs pho-

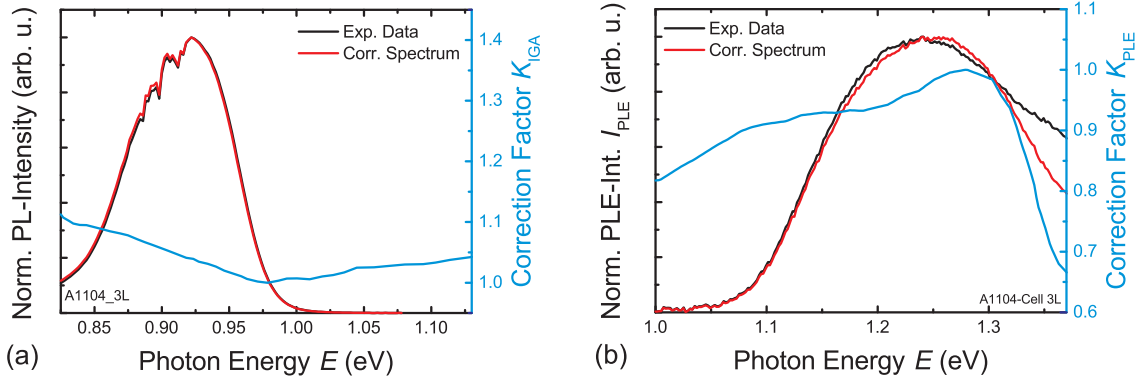


Figure B.1: (a) Example PL spectrum as-recorded (black) and corrected (red) for the spectral responsivity of the photodiode using the correction function K_{PL} (blue). (b) Example PLE spectrum as-recorded (black) and corrected (red) taking into account the spectral responsivity of both the detection photodiode and the reference diode by multiplication with a correction factor K_{PLE} (blue).

photodiode R_{IGA} but also for the incident excitation intensity $I_{exc,meas}(\hbar\omega)$ which was measured using a second InGaAs photodiode (*Thorlabs PDA255*) which a second responsivity R_{PDA} corresponds to. First the excitation intensity was corrected using the relation

$$I_{exc,corr}(\hbar\omega_{exc}) = \frac{1}{R_{PDA}\hbar\omega_{exc}} \times I_{exc,meas}(\hbar\omega_{exc}) = K_{PDA}(\hbar\omega_{exc})I_{exc,meas}(\hbar\omega_{exc}). \quad (\text{B.4})$$

The detected PLE signal is a function of both the excitation ($\hbar\omega_{exc}$) and detection energy ($\hbar\omega_{det}$). The measured PLE signal was therefore corrected for the incident excitation energy as well as response of the photodiode at the detection energy. Furthermore, it was corrected for the PL signal at the detection energy. Therefore, the correction function for the PLE signal $K_{PLE}(\hbar\omega_{exc}, \hbar\omega_{det})$ is given by

$$K_{PLE}(\hbar\omega_{exc}, \hbar\omega_{det}) = \frac{K_{IGA}(\hbar\omega_{det})}{I_{PL,corr}(\hbar\omega_{det})I_{exc,corr}}. \quad (\text{B.5})$$

An example PLE spectrum with the corresponding corrected PLE spectrum is shown in Fig. B.1(b).

Appendix C

Samples Investigated In This Work

In the following, a few remarks will be given on the samples which were investigated in this work. It should be noted that all samples were entire and functional solar cells. First, the investigated CIGS samples will be summarized and described:

- **9358041-Cell 6:**

Graded band gap CIGS sample fabricated at ZSW. GGI gradient starting at $x = 0.24$ at the front to $x = 0.33$ at the back side. $[\text{Cu}]/([\text{Ga}]+[\text{In}])=0.82$ as determined by SNMS measurement. Layer sequence: Mo-SLG/CIGS/CdS/i-ZnO/ZnO:Al. Measurement of ER in specular reflection and with square-wave voltage 0 V to -1.8 V.

- **GGI-Series:**

Series of 4 CIGS solar cells with varying GGI. Apart from the Ga-content x , no further composition details are known for the samples. Samples were used to demonstrate diffuse ER.

- GGI=0: pure CuInSe_2 solar cell
- GGI=0.3: CIGS solar cell with $x = 0.3$
- GGI=0.6: CIGS solar cell with $x = 0.6$, measurement with square-wave voltage 0 V to -2 V
- GGI=1.0: pure CuGaSe_2 solar cell

Finally, the investigated CZTSSe samples:

- **Stripe A1098 (ZSW):**

- Cell-1mR: Standard CZTSSe sample. Thermal post-treatment to check for reversibility of order–disorder related band gap shifts. Underwent alternating post-annealing at $T = 130^\circ\text{C}$ ($2\times$) and 210°C ($3\times$) for 4h followed by a rapid cool-down.
- Cell-7L: Standard CZTSSe sample. Thermal post-treatment to determine maximum band gap tuning range of order–disorder related band gap shifts. Sample was annealed at $T = 210^\circ\text{C}$ for 4h, followed by a slow cool-down to room temperature at a rate of 3K/h. Afterwards it was annealed at $T = 210^\circ\text{C}$, followed by a rapid cool-down.
- Cell-9mR: Standard CZTSSe sample. Thermal post-treatment to determine the critical temperature T_C of the order–disorder transition. Repeated annealing for 14h at successively increasing temperatures (starting from 130°C up to 240°C in 10°C steps) followed by rapid cool-down.
- Cell-9L: Standard CZTSSe sample. Thermal post-treatment to determine the critical temperature T_C of the order–disorder transition. Repeated annealing for 4h at successively increasing temperatures (starting from 130°C up to 230°C in 10°C steps) followed by rapid cool-down.
- Cell-11L: Standard CZTSSe sample. Thermal post-treatment to study temporal evolution of the ordering process. Sample was initially disordered performing annealing at $T = 210^\circ\text{C}$ for 2h followed by a rapid cool-down. Then annealing at $T = 130^\circ\text{C}$ for 2h terminated by rapid cool-down ($8\times$). Afterwards, sample disordered again as already described. Then annealing at $T = 170^\circ\text{C}$ for 2h followed by rapid-cool down ($5\times$).

- **Stripe A1104:**

- Cell-1R: Standard CZTSSe sample. No thermal treatment. Evaporation of 100nm In/50nm Au contact for wire bonding contact. Measurement of ER-T.
- Cell-3L: Standard CZTSSe sample. Thermal post-treatment to increase the absorber band gap to yield a PL spectrum at higher energies to allow for excitation power-dependent measurements over more orders of magnitude. Sample underwent improved annealing procedure: 150°C for 2h followed by a slow cool-down (2K/h).

- Cell-5L: Standard CZTSSe sample. Thermal post-treatment to increase the absorber band gap to improve/shift spectral position of the PL/PLE signal to higher energies. Sample underwent improved annealing procedure: 150 °C for 2 h followed by a slow cool-down (2 K/h).
 - **Stripe A1314:**
Sample series of 6 CZTSSe solar cells (Cell 1–6R) to investigate the effect of post-annealing treatments on device performance. Samples underwent the improved ordering procedure (150 °C for 2 h, cool-down at 2 K/h) and disordering procedure (210 °C for 2 h, rapid cool-down) alternatingly in the sequence: Ordering–Disordering–Ordering.
 - **Sample Series AR407a–c:**
Series of 3 CZTSe solar cells with the absorber layer prepared in the same run of a coevaporation process (Uni Lux). Standard layer architecture: Mo-SLG/CZTSe/CdS/i-ZnO/ZnO:Al, the with different thickness depending on the sample. Used for measurements to demonstrate diffuse electroreflectance.
 - AR407a $d_{\text{ZnO:Al}} = 180 \text{ nm}$
 - AR407b $d_{\text{ZnO:Al}} = 280 \text{ nm}$
 - AR407c $d_{\text{ZnO:Al}} = 380 \text{ nm}$
 - **CZTS Sample JS-1:**
CZTS sample prepared at the university of Uppsala. Sample based on standard architecture Mo-SLG/CZTS/CdS/i-ZnO/ZnO:Al. Used for ER-T measurement.
-

List of Publications

Regular Articles

1. **Fabrication of Polycrystalline $\text{Cu}_2\text{ZnSnSe}_4$ Layers with Strongly Preferential Grain Orientation via Selenization of $\text{Sn/Cu/ZnSe(001)}/\text{GaAs(001)}$ Structures,**
C. Krämmer, J. Sachs, M. Lang, L. Pfaffmann, C. Gao, D. Gerthsen, H. Kalt, M. Powalla, and M. Hetterich, *Appl. Phys. Lett.* **104**, 071913 (2014)
2. **Fast Electron Spin Resonance Controlled Manipulation of Spin Injection into Quantum Dots,**
A. Merz, J. Siller, R. Schittny, C. Krämmer, H. Kalt, and M. Hetterich, *Appl. Phys. Lett.* **104**, 252401 (2014)
3. **$\text{Cu}_2\text{ZnSn(S,Se)}_4$ Solar Cells Based on Chemical Bath Deposited Precursors,**
C. Gao, T. Schnabel, T. Abzieher, C. Krämmer, M. Powalla, H. Kalt, and M. Hetterich, *Thin Solid Films* **562**, pp. 621-624 (2014)
4. **Assessment of Crystal Quality and Unit Cell Orientation in Epitaxial $\text{Cu}_2\text{ZnSnSe}_4$ Layers Using Polarized Raman Scattering,**
C. Krämmer, M. Lang, A. Redinger, J. Sachs, C. Gao, H. Kalt, S. Siebentritt, and M. Hetterich, *Opt. Exp.* **22** (23), pp. 28240-28246 (2014)
5. **Reversible Order-Disorder Related Band Gap Changes in $\text{Cu}_2\text{ZnSn(S,Se)}_4$ via Post-Annealing of Solar Cells Measured by Electroreflectance,**
C. Krämmer, C. Huber, C. Zimmermann, M. Lang, T. Schnabel, T. Abzieher, E. Ahlswede, H. Kalt, and M. Hetterich, *Appl. Phys. Lett.* **105**, 262104 (2014)

6. **Epitaxial $\text{Cu}_2\text{ZnSnSe}_4$ Layers by Annealing of Sn/Cu/ZnSe(001) Precursors on GaAs(001),**
C. Krämmer, J. Sachs, L. Pfaffmann, T. Musiol, M. Lang, C. Gao, D. Gerthsen, H. Kalt, M. Powalla, and M. Hetterich, *Thin Solid Films* **582**, pp. 158-161 (2015)
7. **Electroreflectance of Thin-Film Solar Cells: Simulation and Experiment,**
C. Huber, C. Krämmer, D. Sperber, A. Magin, H. Kalt, and M. Hetterich, *Phys. Rev. B*, *accepted* (2015)

Contributions to International Conferences and Workshops

1. **Fabrication of $\text{Cu}_2\text{ZnSnSe}_4$ Layers with Preferential Grain Orientation via Selenization of Sn/Cu/ZnSe(001)/GaAs(001) Structures,**
C. Krämmer, J. Sachs, M. Lang, C. Gao, T. Musiol, D. Sperber, M. Powalla, Heinz Kalt, and M. Hetterich, *4th European Kesterite Workshop, Berlin, Germany (2014)*, Poster Presentation
2. **$\text{Cu}_2\text{ZnSnSe}_4$ Thin Films and Solar Cells Based on Co-Evaporated Precursors,**
C. Gao, T. Schnabel, C. Krämmer, M. Lang, J. Sachs, E. Ahlswede, M. Powalla, H. Kalt, and M. Hetterich, *4th European Kesterite Workshop, Berlin, Germany (2014)*, Poster Presentation
3. **Epitaxial $\text{Cu}_2\text{ZnSnSe}_4$ Layers by Annealing of Sn/Cu/ZnSe(001) Precursors on GaAs(001),**
C. Krämmer, J. Sachs, L. Pfaffmann, T. Musiol, M. Lang, C. Gao, D. Gerthsen, Heinz Kalt, M. Powalla, and M. Hetterich, *E-MRS Spring Meeting, Lille, France (2014)*, Poster Presentation
4. **Electroreflectance Spectroscopy on $\text{Cu}(\text{In,Ga})\text{Se}_2$ Solar Cells with Different Buffer Layers,**
O. Kiowski, W. Witte, A. Bauer, D. Sperber, C. Krämmer, M. Hetterich, and M. Powalla, *E-MRS Spring Meeting, Lille, France (2014)*, Poster Presentation

-
5. **Preparation of $\text{Cu}_2\text{ZnSn}(\text{S,Se})_4$ Solar Cells Using a Chemical Bath Deposition Route,**
C. Gao, T. Schnabel, T. Abzieher, M. Lang, C. Krämmer, E. Ahlswede, M. Powalla, H. Kalt, and M. Hetterich, *E-MRS Spring Meeting, Lille, France (2014)*, Poster Presentation
 6. **Preparation of $\text{Cu}_2\text{ZnSnSe}_4$ Solar Cells Using a Co-Evaporation Route,**
C. Gao, T. Schnabel, T. Abzieher, M. Lang, C. Krämmer, M. Powalla, H. Kalt, and M. Hetterich, *E-MRS Spring Meeting, Lille, France (2014)*, Poster Presentation
 7. **Raman Investigation of Epitaxial $\text{Cu}_2\text{ZnSnSe}_4$ Layers from Annealed $\text{Sn/Cu/ZnSe}(001)$ Precursors on $\text{GaAs}(001)$,**
C. Krämmer, M. Lang, J. Sachs, L. Pfaffmann, C. Gao, D. Gerthsen, Heinz Kalt, M. Powalla, and M. Hetterich, *IEEE Photovoltaic Specialists Conference, Denver, Colorado, US (2014)*, Poster Presentation and Proceedings Article
 8. **An Electroreflectance Study of the Order-Disorder Transition in $\text{Cu}_2\text{ZnSn}(\text{S,Se})_4$ Solar Cells,**
C. Krämmer, C. Huber, C. Zimmermann, M. Lang, T. Schnabel, T. Abzieher, Heinz Kalt, and M. Hetterich, *5th European Kesterite Workshop, Tallinn, Estonia (2014)*, Oral Presentation
 9. **Order-Disorder Related Band Gap Changes in $\text{Cu}_2\text{ZnSn}(\text{S,Se})_4$: Impact on Solar Cell Performance,**
C. Krämmer, C. Huber, T. Schnabel, C. Zimmermann, M. Lang, E. Ahlswede, Heinz Kalt, and M. Hetterich, *IEEE Photovoltaic Specialists Conference, New Orleans, Louisiana, US (2015)*, Poster Presentation and Proceedings Article
 10. **The Influence of the Degree of Cu–Zn Disorder on the Radiative Recombination Transitions in $\text{Cu}_2\text{ZnSn}(\text{S,Se})_4$ Solar Cells,**
M. Lang, C. Zimmermann, C. Krämmer, C. Huber, T. Schnabel, T. Abzieher, E. Ahlswede, H. Kalt, and M. Hetterich, *IEEE Photovoltaic Specialists Conference, New Orleans, Louisiana, US (2015)*, Poster Presentation and Proceedings Article

Contributions to DPG Spring Meetings

1. **Optical Investigation of Kesterite and CIGS Absorber Layers**,
D. Sperber, C. Krämmer, C. Gao., M. Löw, T. Schnabel, E. Ahlswede, M. Powalla, H. Kalt, and M. Hetterich, *DPG spring meeting, Regensburg (2013)*
2. **A Low-Cost Solution Method to Fabricate $\text{Cu}_2\text{ZnSn}(\text{S},\text{Se})_4$ Solar Cells**,
C. Gao, T. Schnabel, T. Abzieher, C. Krämmer, E. Ahlswede, M. Powalla, H. Kalt, and M. Hetterich, *DPG spring meeting, Dresden (2014)*
3. **Raman Investigation of $\text{Cu}_2\text{ZnSnSe}_4$ Layers with and without Preferential Grain Orientation**,
M. Lang, C. Krämmer, J. Sachs, C. Gao, S. Schuster, M. Powalla, H. Kalt, and M. Hetterich, *DPG spring meeting, Dresden (2014)*
4. **Growth and Characterization of Polycrystalline $\text{Cu}_2\text{ZnSnSe}_4$ Layers with a Preferential Grain Orientation**,
C. Krämmer, J. Sachs, M. Lang, C. Gao, S. Schuster, M. Powalla, H. Kalt, and M. Hetterich, *DPG spring meeting, Dresden (2014)*
5. **$\text{Cu}_2\text{ZnSnSe}_4$ Layers and Solar Cells from Selenized Coevaporated Precursors**,
T. Musiol, C. Gao, T. Schnabel, M. Lang, C. Krämmer, E. Ahlswede, M. Powalla, H. Kalt, and M. Hetterich, *DPG spring meeting, Dresden (2014)*
6. **Polycrystalline $\text{Cu}_2\text{ZnSnSe}_4$ Layers on GaAs(001) with a Preferential Grain Orientation**,
J. Sachs, C. Krämmer, M. Lang, C. Gao, M. Powalla, H. Kalt, and M. Hetterich, *DPG spring meeting, Dresden (2014)*
7. **Simulation of Interference-Related Lineshape Distortions in Electroreflectance Spectra of $\text{Cu}(\text{In},\text{Ga})\text{Se}_2$ Thin-Film Solar Cells**,
C. Huber, C. Krämmer, D. Sperber, H. Kalt, and M. Hetterich, *DPG spring meeting, Berlin (2015)*
8. **Photoluminescence Investigation of the Order–Disorder Effect in $\text{Cu}_2\text{ZnSn}(\text{S},\text{Se})_4$ Solar Cells**,
C. Zimmermann, M. Lang, C. Krämmer, C. Huber, T. Schnabel, T. Abzieher, A. Schulz, H. Kalt, and M. Hetterich, *DPG spring meeting, Berlin (2015)*

-
9. **Reversible Band Gap Changes in $\text{Cu}_2\text{ZnSn}(\text{S,Se})_4$ Solar Cells Induced by Post-Annealing,**
C. Krämmer, C. Huber, C. Zimmermann, M. Lang, T. Schnabel, T. Abzieher, E. Ahlswede, H. Kalt, and M. Hetterich, *DPG spring meeting, Berlin (2015)*
 10. **Investigation of Order–Disorder Related Band Gap Changes in $\text{Cu}_2\text{ZnSn}(\text{S,Se})_4$ Solar Cells Using Electreflectance,**
C. Krämmer, C. Huber, C. Zimmermann, M. Lang, A. Opolka, T. Schnabel, T. Abzieher, E. Ahlswede, H. Kalt, and M. Hetterich, *DPG spring meeting, Berlin (2015)*
 11. **Solution-Based Fabrication of Kesterite $\text{Cu}_2\text{ZnSnSe}_4$ Absorber Layers and Solar Cells,**
M. Neuwirth, H. Zhou, C. Gao, M. Lang, C. Zimmermann, C. Krämmer, C. Huber, A. Schiele, T. Schnabel, T. Abzieher, E. Ahlswede, M. Powalla, H. Kalt, and M. Hetterich, *DPG spring meeting, Berlin (2015)*
 12. **Two-Step Fabrication Process for $\text{Cu}_2\text{ZnSnSe}_4$ Layers and Solar Cells on GaAs and Molybdenum-Coated Glass Substrates,**
A. Schiele, C. Gao, M. Lang, C. Krämmer, T. Schnabel, T. Abzieher, E. Ahlswede, H. Kalt, and M. Hetterich, *DPG spring meeting, Berlin (2015)*
 13. **Effect of Post-Annealing on $\text{Cu}_2\text{ZnSn}(\text{S,Se})_4$ Solar Cells Studied by Photoluminescence Spectroscopy,**
C. Zimmermann, C. Krämmer, C. Huber, M. Lang, T. Schnabel, T. Abzieher, E. Ahlswede, H. Kalt, and M. Hetterich, *DPG spring meeting, Berlin (2015)*

Bibliography

- [1] Bundesamt für Strahlenschutz, “Die Katastrophe im Kernkraftwerk Fukushima nach dem Seebeben vom 11. März 2011,” (2011). <http://nbn-resolving.de/urn:nbn:de:0221-201203027611>, accessed 25.05.2015.
- [2] International Energy Agency, “Key World Energy Statistics 2014,” (2014). <https://www.iea.org/publications/freepublications/publication/KeyWorld2014.pdf>, accessed 25.05.2015.
- [3] D. Yue, F. You, and S. B. Darling, “Domestic and Overseas Manufacturing Scenarios of Silicon-Based Photovoltaics: Life Cycle Energy and Environmental Comparative Analysis,” *Sol. Energy* **105**, 669 – 678 (2014).
- [4] P. Torcellini, S. Pless, M. Deru, and D. Crawley, “Zero Energy Buildings: a Critical Look at the Definition,” National Renewable Energy Laboratory and Department of Energy, US (2006).
- [5] S. Pizzini, “Towards Solar Grade Silicon: Challenges and Benefits for Low Cost Photovoltaics,” *Sol. Energ. Mat. Sol. C.* **94**, 1528 – 1533 (2010).
- [6] L. E. Chaar, L. lamont, and N. E. Zein, “Review of Photovoltaic Technologies,” *Renew. Sust. Energ. Rev.* **15**, 2165 – 2175 (2011).
- [7] P. Jackson, D. Hariskos, R. Wuerz, O. Kiowski, A. Bauer, T. M. Friedlmeier, and M. Powalla, “Properties of Cu(In,Ga)Se₂ Solar Cells with New Record Efficiencies up to 21.7%,” *Phys. Status Solidi Rapid Res. Lett.* **9**, 28–31 (2015).
- [8] H. Katagiri, K. Jimbo, W. S. Maw, K. Oishi, M. Yamazaki, H. Araki, and A. Takeuchi, “Development of CZTS-Based Thin Film Solar Cells,” *Thin Solid Films* **517**, 2455 – 2460 (2009). *Thin Film Chalogenide Photovoltaic Materials (E-MRS, Symposium L)*.
- [9] Edison Investment Research, “Indium and gallium overview,” (2011). <http://www.edisoninvestmentresearch.com/sectorreports/IndiumGalliumOverview071011.pdf>, accessed 24.05.2015.

BIBLIOGRAPHY

- [10] C. Candelise, M. Winkler, and R. Gross, “Implications for CdTe and CIGS Technologies Production Costs of Indium and Tellurium Scarcity,” *Prog. Photovoltaics* **20**, 816–831 (2012).
- [11] S. Siebentritt and S. Schorr, “Kesterites—a Challenging Material for Solar Cells,” *Prog. Photovoltaics* **20**, 512–519 (2012).
- [12] W. Wang, M. T. Winkler, O. Gunawan, T. Gokmen, T. K. Todorov, Y. Zhu, and D. B. Mitzi, “Device Characteristics of CZTSSe Thin-Film Solar Cells with 12.6% Efficiency,” *Adv. Energ. Mater* **4**, 1301465 (2014).
- [13] W. Shockley and H. J. Queisser, “Detailed Balance Limit of Efficiency of p-n Junction Solar Cells,” *J. Appl. Phys.* **32**, 510 (1961).
- [14] S. Ahn, S. Jung, J. Gwak, A. Cho, K. Shin, K. Yoon, D. Park, H. Cheong, and J. H. Yun, “Determination of Band Gap Energy E_g of $\text{Cu}_2\text{ZnSnSe}_4$ Thin Films: On the Discrepancies of Reported Band Gap Values,” *Appl. Phys. Lett.* **97**, 021905 (2010).
- [15] D. Aspnes, “Third-Derivative Modulations Spectroscopy with Low-Field Electroreflectance,” *Surf. Sci.* **37**, 418–442 (1973).
- [16] C. M. Herzinger, B. Johs, W. A. McGahan, J. A. Woollam, and W. Paulson, “Ellipsometric Determination of Optical Constants for Silicon and Thermally Grown Silicon Dioxide via a Multi-Sample, Multi-Wavelength, Multi-Angle Investigation,” *J. Appl. Phys.* **83**, 3323 (1998).
- [17] D. E. Aspnes and A. A. Studna, “Dielectric Functions and Optical Parameters of Si, Ge, GaP, GaAs, GaSb, InP, InAs, and InSb from 1.5 to 6.0 eV,” *Phys. Rev. B* **27**, 985–1009 (1983).
- [18] J. M. Woodall and H. J. Hovel, “An Isothermal Etchback-Regrowth Method for High-Efficiency $\text{Ga}_{1-x}\text{Al}_x\text{As-GaAs}$ Solar Cells,” *Appl. Phys. Lett.* **30**, 492–493 (1977).
- [19] Fraunhofer ISE, “Solarzelle mit 46% Wirkungsgrad – Neuer Weltrekord,” (2014). <http://www.ise.fraunhofer.de/de/presse-und-medien/pdfs-zu-presseinfos/-nivc-2014/presseinformation-solarzelle-mit-46-prozent-wirkungsgrad.pdf>, accessed 25.05.2015.
- [20] G. L. Hansen, J. L. Schmit, and T. N. Casselman, “Energy Gap Versus Alloy Composition and Temperature in $\text{Hg}_{1-x}\text{Cd}_x\text{Te}$,” *J. Appl. Phys.* **53**, 7099–7101 (1982).

- [21] First Solar, “First Solar Builds the Highest Efficiency Thin Film PV Cell on Record,” (2014). <http://investor.firstsolar.com/releasedetail.cfm?releaseid=864426>, accessed 25.05.2015.
- [22] V. Fthenakis, “Sustainability of Photovoltaics: The Case for Thin-Film Solar Cells,” *Renew. Sust. Energ. Rev.* **13**, 2746 – 2750 (2009).
- [23] Bundesverband Solarwirtschaft e.V., “Cadmium-Tellurid (CdTe) Photovoltaiktechnologie,” (2009). http://www.solarwirtschaft.de/fileadmin/content_files/Hintergrund_CdTe_0309.pdf, accessed 25.05.2015.
- [24] V. M. Fthenakis, M. Fuhrmann, J. Heiser, A. Lanzirotti, J. Fitts, and W. Wang, “Emissions and Encapsulation of Cadmium in CdTe PV Modules During Fires,” *Prog. Photovoltaics* **13**, 713–723 (2005).
- [25] B. O’regan and M. Grätzel, “A Low-Cost, High-Efficiency Solar Cell based on Dye-Sensitized Colloidal TiO₂ Films,” *Nature* **353**, 737–740 (1991).
- [26] D. Wöhrle and D. Meissner, “Organic Solar Cells,” *Adv. Mater.* **3**, 129–138 (1991).
- [27] M. A. Green, A. Ho-Baillie, and H. J. Snaith, “The Emergence of Perovskite Solar Cells,” *Nature Photon.* **8**, 506–514 (2014).
- [28] S. Minoura, K. Kodera, T. Maekawa, K. Miyazaki, S. Niki, and H. Fujiwara, “Dielectric Function of Cu(In,Ga)Se₂-Based Polycrystalline Materials,” *J. Appl. Phys.* **113**, 063505 (2013).
- [29] K. Momma and F. Izumi, “*VESTA* for Three-Dimensional Visualization of Crystal, Volumetric and Morphology Data,” *Journal of Applied Crystallography* **44**, 1272–1276 (2011).
- [30] J. L. Shay and B. Tell, “Energy Band Structure of I–III–VI₂ Semiconductors,” *Surf. Sci.* **37**, 748–762 (1973).
- [31] C. Goodman, “The Prediction of Semiconducting Properties in Inorganic Compounds,” *J. Phys. Chem. Solids* **6**, 305–314 (1958).
- [32] S. Hall, J. Szymanski, and J. Stewart, “Kesterite, Cu₂(Zn,Fe)SnS₄ and Stannite Cu₂(Fe,Zn)SnS₄, Structurally Similar But Distinct Minerals,” *Can. Mineralogist* **16**, 131–137 (1978).
- [33] C. Krämmer, J. Sachs, M. Lang, L. Pfaffmann, C. Gao, D. Gerthsen, H. Kalt, M. Powalla, and M. Hetterich, “Fabrication of Polycrystalline

BIBLIOGRAPHY

- Cu₂ZnSnSe₄ Layers with Strongly Preferential Grain Orientation via Selenization of Sn/Cu/ZnSe(001)/GaAs(001) Structures,” *Appl. Phys. Lett.* **104**, 071913 (2014).
- [34] C. Krämmer, J. Sachs, L. Pfaffmann, T. Musiol, M. Lang, C. Gao, D. Gerthsen, H. Kalt, M. Powalla, and M. Hetterich, “Epitaxial Cu₂ZnSnSe₄ Layers by Annealing of Sn/Cu/ZnSe(001) Precursors on GaAs(001),” *Thin Solid Films* **582**, 158 – 161 (2015). E-MRS 2014 Spring Meeting, Symposium A, Thin-Film Chalcogenide Photovoltaic Materials.
- [35] A. Walsh, S. Chen, S.-H. Wei, and X.-G. Gong, “Kesterite Thin-Film Solar Cells: Advances in Materials Modelling of Cu₂ZnSnS₄,” *Adv. Energ. Mater.* **2**, 400–409 (2012).
- [36] J. Parkes, R. D. Tomlinson, and M. J. Hampshire, “Crystal Data for CuInSe₂,” *J. Appl. Crystallography* **6**, 414–416 (1973).
- [37] S. C. Abrahams, “Piezoelectric Nonlinear Optic CuGaSe₂ and CdGeAs₂: Crystal structure, Chalcopyrite Microhardness, and Sublattice Distortion,” *J. Chem. Physics* **61**, 1140 (1974).
- [38] M. Guc, S. Levchenko, V. Izquierdo-Roca, X. Fontané, E. Arushanov, and A. Pérez-Rodríguez, “Polarized Raman Scattering Analysis of Cu₂ZnSnSe₄ and Cu₂ZnGeSe₄ Single Crystals,” *J. Appl. Phys.* **114**, 193514 (2013).
- [39] J. Paier, R. Asahi, A. Nagoya, and G. Kresse, “Cu₂ZnSnS₄ as a Potential Photovoltaic Material: A Hybrid Hartree-Fock Density Functional Theory Study,” *Phys. Rev. B* **79**, 1–8 (2009).
- [40] S. Chen, X. G. Gong, A. Walsh, and S.-H. Wei, “Crystal and Electronic Band Structure of Cu₂ZnSnX₄ (X=S and Se) Photovoltaic Absorbers: First-Principles Insights,” *Appl. Phys. Lett.* **94**, 041903 (2009).
- [41] S. Schorr, “The Crystal Structure of Kesterite Type Compounds: A Neutron and X-ray Diffraction Study,” *Sol. Energy Mater. Sol. C.* **95**, 1482–1488 (2011).
- [42] J. Jaffe and A. Zunger, “Electronic Structure of the Ternary Chalcopyrite Semiconductors CuAlS₂, CuGaS₂, CuInS₂, CuAlSe₂, CuGaSe₂, and CuInSe₂,” *Phys. Rev. B* **28**, 5822–5847 (1983).
- [43] C. Persson and A. Zunger, “Compositionally Induced Valence-Band Offset at the Grain Boundary of Polycrystalline Chalcopyrites Creates a Hole Barrier,” *Appl. Phys. Lett.* **87**, 1–3 (2005).

- [44] M. Alonso, K. Wakita, J. Pascual, M. Garriga, and N. Yamamoto, “Optical Functions and Electronic Structure of CuInSe_2 , CuGaSe_2 , CuInS_2 , and CuGaS_2 ,” *Phys. Rev. B* **63**, 075203 (2001).
- [45] C. Persson, “Electronic and Optical Properties of $\text{Cu}_2\text{ZnSnS}_4$ and $\text{Cu}_2\text{ZnSnSe}_4$,” *J. Appl. Phys.* **107** (2010).
- [46] N. Mortazavi Amiri and A. Postnikov, “Electronic Structure and Lattice Dynamics in Kesterite-Type $\text{Cu}_2\text{ZnSnSe}_4$ From First-Principles Calculations,” *Phys. Rev. B* **82**, 1–8 (2010).
- [47] S. Chen, A. Walsh, X.-G. Gong, and S.-H. Wei, “Classification of Lattice Defects in the Kesterite $\text{Cu}_2\text{ZnSnS}_4$ and $\text{Cu}_2\text{ZnSnSe}_4$ Earth-Abundant Solar Cell Absorbers,” *Adv. Mater.* **25**, 1522–1539 (2013).
- [48] J. H. Werner, J. Mattheis, and U. Rau, “Efficiency Limitations of Polycrystalline Thin Film Solar Cells: Case of $\text{Cu}(\text{In,Ga})\text{Se}_2$,” *Thin Solid Films* **480-481**, 399–409 (2005).
- [49] T. Dullweber, G. Anna, U. Rau, and H. Schock, “A New Approach to High-Efficiency Solar Cells by Band Gap Grading in $\text{Cu}(\text{In,Ga})\text{Se}_2$ Chalcopyrite Semiconductors,” *Sol. Energy Mater. Sol. C.* **67**, 145–150 (2001).
- [50] M. Gloeckler and J. Sites, “Band-Gap Grading in $\text{Cu}(\text{In,Ga})\text{Se}_2$ Solar Cells,” *J. Phys. Chem. Solids* **66**, 1891–1894 (2005).
- [51] S. Nishiwaki, S. Siebentritt, P. Walk, and M. Ch. Lux-Steiner, “A Stacked Chalcopyrite Thin-Film Tandem Solar Cell with 1.2 V Open-Circuit Voltage,” *Prog. Photovoltaics* **11**, 243–248 (2003).
- [52] M. Alonso, M. Garriga, C. Durante Rincón, E. Hernández, and M. León, “Optical Functions of Chalcopyrite $\text{CuGa}_x\text{In}_{1-x}\text{Se}_2$ Alloys,” *Appl. Phys. A Mater.* **74**, 659–664 (2002).
- [53] P. D. Paulson, R. W. Birkmire, and W. N. Shafarman, “Optical Characterization of $\text{CuIn}_{1-x}\text{Ga}_x\text{Se}_2$ Alloy Thin Films by Spectroscopic Ellipsometry,” *J. Appl. Phys.* **94**, 879 (2003).
- [54] C. S. Schnohr, H. Kämmer, C. Stephan, S. Schorr, T. Steinbach, and J. Rensberg, “Atomic-Scale Structure and Band-Gap Bowing in $\text{Cu}(\text{In,Ga})\text{Se}_2$,” *Phys. Rev. B* **85**, 245204 (2012).
- [55] M. Bär, W. Bohne, J. Röhrich, E. Strub, S. Lindner, M. C. Lux-Steiner, C.-H. Fischer, T. P. Niesen, and F. Karg, “Determination of the Band Gap

BIBLIOGRAPHY

- Depth Profile of the Pternary $\text{Cu}(\text{In}_{(1-x)}\text{Ga}_x)(\text{S}_y\text{Se}_{(1-y)})_2$ Chalcopyrite from its Composition Gradient,” J. Appl. Phys. **96**, 3857 (2004).
- [56] S. Chichibu, T. Mizutani, K. Murakami, T. Shioda, T. Kurafuji, H. Nakanishi, S. Niki, P. J. Fons, and a. Yamada, “Band Gap Energies of Bulk, Thin-Film, and Epitaxial Layers of CuInSe_2 and CuGaSe_2 ,” J. Appl. Phys. **83**, 3678 (1998).
- [57] S. H. Han, A. M. Hermann, F. S. Hasoon, H. a. Al-Thani, and D. H. Levi, “Effect of Cu Deficiency on the Optical Properties and Electronic Structure of CuInSe_2 and $\text{CuIn}_{0.8}\text{Ga}_{0.2}\text{Se}_2$ Determined by Spectroscopic Ellipsometry,” Appl. Phys. Lett. **85**, 576–578 (2004).
- [58] M. Altosaar, J. Raudoja, K. Timmo, M. Danilson, M. Grossberg, J. Krustok, and E. Mellikov, “ $\text{Cu}_2\text{Zn}_{1-x}\text{Cd}_x\text{Sn}(\text{Se}_{1-y}\text{S}_y)_4$ Solid Solutions as Absorber Materials for Solar Cells,” Phys. Status Solidi A **205**, 167–170 (2008).
- [59] C. J. Hages, N. J. Carter, R. Agrawal, and T. Unold, “Generalized Current-Voltage Analysis and Efficiency Limitations in Non-Ideal Solar Cells: Case of $\text{Cu}_2\text{ZnSn}(\text{S}_x\text{Se}_{1-x})_4$ and $\text{Cu}_2\text{Zn}(\text{Sn}_y\text{Ge}_{1-y})(\text{S}_x\text{Se}_{1-x})_4$,” J. Appl. Phys. **115**, 234504 (2014).
- [60] S. Levchenko, D. Dumcenco, Y. Wang, Y. Huang, C. Ho, E. Arushanov, V. Tezlevan, and K. Tiong, “Influence of Anionic Substitution on the Electrolyte Electroreflectance Study of Band Edge Transitions in Single Crystal $\text{Cu}_2\text{ZnSn}(\text{S}_x\text{Se}_{1-x})_4$ Solid Solutions,” Opt. Mater. **34**, 1362–1365 (2012).
- [61] R. Scheer and H.-W. Schock, *Chalcogenide Photovoltaics* (Wiley-VCH, 2012).
- [62] C. Domain, S. Laribi, S. Taunier, and J. F. Guillemoles, “Ab-Initio Calculation of Intrinsic Point Defects in CuInSe_2 ,” J. Phys. Chem. Solids **64**, 1657–1663 (2003).
- [63] J. Pohl and K. Albe, “Intrinsic Point Defects in CuInSe_2 and CuGaSe_2 as Seen via Screened-Exchange Hybrid Density Functional Theory,” Phys. Rev. B **87**, 245203 (2013).
- [64] C. Rincón, J. González, and G. Sánchez Pérez, “Luminescence and Impurity States in CuInSe_2 ,” J. Appl. Phys. **54**, 6634 (1983).
- [65] C. Rincón, C. Bellabarba, J. González, and G. Sánchez Pérez, “Optical Properties and Characterization of CuInSe_2 ,” Sol. Cells **16**, 335–349 (1986).

- [66] P. Migliorato, J. L. Shay, H. M. Kasper, and S. Wagner, "Analysis of the Electrical and Luminescent Properties of CuInSe_2 ," *J. Appl. Phys.* **46**, 1777 (1975).
- [67] G. Massé, K. Djessas, and F. Guastavino, "Study of $\text{CuGa}_x\text{In}_{1-x}\text{Se}_2$ and $\text{CuGa}_x\text{In}_{1-x}\text{Te}_2$ Compounds," *J. Phys. Chem. Solids* **52**, 999–1004 (1991).
- [68] A. Redinger, D. M. Berg, P. J. Dale, R. Djemour, G. Levent, T. Eisenbarth, N. Valle, S. Siebentritt, and A. Thin-film, "Route Towards High Efficiency Single Phase $\text{Cu}_2\text{ZnSn}(\text{S},\text{Se})_4$ Thin Film Solar Cells: Model Experiments and Literature Review," *IEEE J. Photovolt.* **1**, 200–206 (2011).
- [69] W. Ki and H. W. Hillhouse, "Earth-Abundant Element Photovoltaics Directly from Soluble Precursors with High Yield Using a Non-Toxic Solvent," *Adv. Energ. Mater.* **1**, 732–735 (2011).
- [70] A. Redinger, M. Mousel, R. Djemour, L. Gütay, N. Valle, and S. Siebentritt, " $\text{Cu}_2\text{ZnSnSe}_4$ Thin Film Solar Cells Produced via Co-Evaporation and Annealing Including a SnSe_2 Capping Layer," *Prog. Photovoltaics* **22**, 51–57 (2014).
- [71] I. Repins, C. Beall, N. Vora, C. DeHart, D. Kuciauskas, P. Dippo, B. To, J. Mann, W.-C. Hsu, A. Goodrich, and R. Noufi, "Co-Evaporated $\text{Cu}_2\text{ZnSnSe}_4$ Films and Devices," *Sol. Energ. Mat. Sol. C.* **101**, 154–159 (2012).
- [72] I. V. Dudchak and L. V. Piskach, "Phase Equilibria in the Cu_2SnSe_3 - SnSe_2 - ZnSe System," *J. Alloy Compd.* **351**, 145–150 (2003).
- [73] T. Schwarz, O. Cojocaru-Mirédin, P. Choi, M. Mousel, A. Redinger, S. Siebentritt, and D. Raabe, "Atom Probe Study of $\text{Cu}_2\text{ZnSnSe}_4$ Thin-Films Prepared by Co-Evaporation and Post-Deposition Annealing," *Appl. Phys. Lett.* **102**, 042101 (2013).
- [74] J. Timo Wätjen, J. Engman, M. Edoff, and C. Platzer-Björkman, "Direct Evidence of Current Blocking by ZnSe in $\text{Cu}_2\text{ZnSnSe}_4$ Solar Cells," *Appl. Phys. Lett.* **100**, 2013–2016 (2012).
- [75] S. Siebentritt, "Why Are Kesterite Solar Cells Not 20% Efficient?" *Thin Solid Films* **535**, 10–13 (2013).
- [76] S. Y. Chen, A. Walsh, J. H. Yang, X. G. Gong, L. Sun, P. X. Yang, J. H. Chu, and S. H. Wei, "Compositional Dependence of Structural and Electronic properties of $\text{Cu}_2\text{ZnSn}(\text{S},\text{Se})_4$ Alloys for Thin Film Solar Cells," *Phys. Rev. B* **83**, 1–5 (2011).

BIBLIOGRAPHY

- [77] D. Huang and C. Persson, “Band Gap Change Induced by Defect Complexes in $\text{Cu}_2\text{ZnSnS}_4$,” *Thin Solid Films* **535**, 265–269 (2013).
- [78] T. Gokmen, O. Gunawan, T. K. Todorov, and D. B. Mitzi, “Band Tailing and Efficiency Limitation in Kesterite Solar Cells,” *Appl. Phys. Lett.* **103**, 103506 (2013).
- [79] J. P. Teixeira, R. A. Sousa, M. G. Sousa, A. F. da Cunha, P. A. Fernandes, P. M. P. Salomé, J. C. González, and J. P. Leitão, “Comparison of Fluctuating Potentials and Donor-Acceptor Pair Transitions in a Cu-Poor $\text{Cu}_2\text{ZnSnS}_4$ Based Solar Cell,” *Appl. Phys. Lett.* **105**, 163901 (2014).
- [80] J. P. Teixeira, R. A. Sousa, M. G. Sousa, A. F. da Cunha, P. A. Fernandes, P. M. P. Salomé, and J. P. Leitão, “Radiative Transitions in Highly Doped and Compensated Chalcopyrites and Kesterites: The Case of $\text{Cu}_2\text{ZnSnS}_4$,” *Phys. Rev. B* **90**, 235202 (2014).
- [81] U. Rau and J. H. Werner, “Radiative efficiency limits of solar cells with lateral band-gap fluctuations,” *Appl. Phys. Lett.* **84**, 3735–3737 (2004).
- [82] L. Kronik, D. Cahen, and H. W. Schock, “Effects of Sodium on Polycrystalline $\text{Cu}(\text{In,Ga})\text{Se}_2$ and Its Solar Cell Performance,” *Adv. Mater.* **10**, 31–36 (1998).
- [83] C. M. Sutter-Fella, J. A. Stückelberger, H. Hagendorfer, F. La Mattina, L. Kranz, S. Nishiwaki, A. R. Uhl, Y. E. Romanyuk, and A. N. Tiwari, “Sodium Assisted Sintering of Chalcogenides and Its Application to Solution Processed $\text{Cu}_2\text{ZnSn}(\text{S,Se})_4$ Thin Film Solar Cells,” *Chem. Mater.* **26**, 1420–1425 (2014).
- [84] A. Chirilă, P. Reinhard, F. Pianezzi, P. Bloesch, A. R. Uhl, C. Fella, L. Kranz, D. Keller, C. Gretener, H. Hagendorfer, D. Jaeger, R. Erni, S. Nishiwaki, S. Buecheler, and A. N. Tiwari, “Potassium-Induced Surface Modification of $\text{Cu}(\text{In,Ga})\text{Se}_2$ Thin Films for High-Efficiency Solar Cells.” *Nat. Mater.* **12**, 1107–1111 (2013).
- [85] J. J. Scragg, J. T. Wätjen, M. Edoff, T. Ericson, T. Kubart, and C. Platzer-Björkman, “A Detrimental Reaction at the Molybdenum Back Contact in $\text{Cu}_2\text{ZnSn}(\text{S,Se})_4$ Thin-Film Solar Cells,” *J. Am. Chem. Soc.* **134**, 19330–19333 (2012).
- [86] B. Shin, Y. Zhu, N. a. Bojarczuk, S. J. Chey, and S. Guha, “High Efficiency $\text{Cu}_2\text{ZnSnSe}_4$ Solar Cells With a TiN Diffusion Barrier on the Molybdenum Bottom Contact,” *Conference Record of the IEEE Photovoltaic Specialists Conference* **053903**, 671–673 (2012).

- [87] D. Abou-Ras, G. Kostorz, A. Romeo, D. Rudmann, and A. N. Tiwari, "Structural and Chemical Investigations of CBD- and PVD-CdS Buffer Layers and Interfaces in Cu(In,Ga)Se₂-Based Thin Film Solar Cells," *Thin Solid Films* **480-481**, 118–123 (2005).
- [88] C. Heske, D. Eich, R. Fink, E. Umbach, T. van Buuren, C. Bostedt, L. Terminello, S. Kakar, M. Grush, T. Callcott, F. Himpsel, D. Ederer, R. Perera, W. Riedl, and F. Karg, "Observation of Intermixing at the Buried CdS/Cu(In,Ga)Se₂ Thin Film Solar Cell Heterojunction," *Appl. Phys. Lett.* **74**, 1451–1453 (1999).
- [89] D. Hariskos, S. Spiering, and M. Powalla, "Buffer Layers in Cu(In,Ga)Se₂ Solar Cells and Modules," *Thin Solid Films* **480-481**, 99–109 (2005).
- [90] N. Naghavi, S. Spiering, M. Powalla, B. Cavana, and D. Lincot, "High-Efficiency Copper Indium Gallium Diselenide (CIGS) Solar Cells with Indium Sulfide Buffer Layers Deposited by Atomic Layer Chemical Vapor Deposition (ALCVD)," *Prog. Photovoltaics* **11**, 437–443 (2003).
- [91] C. Platzer-Björkman, T. Törndahl, D. Abou-Ras, J. Malmström, J. Kessler, and L. Stolt, "Zn(O,S) Buffer Layers by Atomic Layer Deposition in Cu(In,Ga)Se₂ Based Thin Film Solar Cells: Band Alignment and Sulfur Gradient," *J. Appl. Phys.* **100**, 044506 (2006).
- [92] M. Reinhard, C. Simon, J. Kuhn, L. Bürkert, M. Cemernjak, B. Dimmler, U. Lemmer, and A. Colsmann, "Cadmium-Free Copper Indium Gallium Diselenide Hybrid Solar Cells Comprising a 2-(4-biphenyl)-5-(4-tert-butylphenyl)-1,3,4-oxadiazole Buffer Layer," *Appl. Phys. Lett.* **102**, 063304 (2013).
- [93] L. Weinhardt, M. Bär, S. Pookpanratana, M. Morkel, T. P. Niesen, F. Karg, K. Ramanathan, M. a. Contreras, R. Noufi, E. Umbach, and C. Heske, "Sulfur Gradient-Driven Se Diffusion at the CdS/CuIn(S,Se)₂ Solar Cell Interface," *Appl. Phys. Lett.* **96**, 182102 (2010).
- [94] O. Cojocaru-Mirédin, P. Choi, R. Wuerz, and D. Raabe, "Exploring the p-n Junction Region in Cu(In,Ga)Se₂ Thin-Film Solar Cells at the Nanometer-Scale," *Appl. Phys. Lett.* **101**, 181603 (2012).
- [95] M. Morkel, L. Weinhardt, B. Lohmüller, C. Heske, E. Umbach, W. Riedl, S. Zweigart, and F. Karg, "Flat Conduction-Band Alignment at the CdS/CuInSe₂ Thin-Film Solar-Cell Heterojunction," *Appl. Phys. Lett.* **79**, 4482 (2001).

BIBLIOGRAPHY

- [96] O. Cojocaru-Mirédin, P. Choi, R. Wuerz, and D. Raabe, “Atomic-Scale Characterization of the CdS/CuInSe₂ Interface in Thin-Film Solar Cells,” *Appl. Phys. Lett.* **98**, 103504 (2011).
- [97] R. Haight, A. Barkhouse, O. Gunawan, B. Shin, M. Copel, M. Hopstaken, and D. B. Mitzi, “Band Alignment at the Cu₂ZnSn(S_xSe_{1-x})₄/CdS Interface,” *Appl. Phys. Lett.* **98**, 253502 (2011).
- [98] M. Bär, B. a. Schubert, B. Marsen, R. G. Wilks, S. Pookpanratana, M. Blum, S. Krause, T. Unold, W. Yang, L. Weinhardt, C. Heske, and H. W. Schock, “Cliff-Like Conduction Band Offset and KCN-Induced Recombination Barrier Enhancement at the CdS/Cu₂ZnSnS₄ Thin-Film Solar Cell Heterojunction,” *Appl. Phys. Lett.* **99**, 97–100 (2011).
- [99] T. K. Todorov, J. Tang, S. Bag, O. Gunawan, T. Gokmen, Y. Zhu, and D. B. Mitzi, “Beyond 11% Efficiency: Characteristics of State-of-the-Art Cu₂ZnSn(S,Se)₄ Solar Cells,” *Adv. Energ. Mater* **3**, 34–38 (2013).
- [100] C. Kind, C. Feldmann, A. Quintilla, and E. Ahlswede, “Citrate-Capped Cu₁₁In₉ Nanoparticles and Its Use for Thin-Film Manufacturing of CIS Solar Cells,” *Chem. Mater.* **23**, 5269–5274 (2011).
- [101] M. Kaelin, D. Rudmann, F. Kurdesau, T. Meyer, H. Zogg, and A. Tiwari, “CIS and CIGS Layers From Selenized Nanoparticle Precursors,” *Thin Solid Films* **431–432**, 58–62 (2003). Proceedings of Symposium B, Thin Film Chalcogenide Photovoltaic Materials, E-MRS Spring Meeting.
- [102] T. Schnabel, M. Löw, and E. Ahlswede, “Vacuum-Free Preparation of 7.5% Efficient Cu₂ZnSn(S,Se)₄ Solar Cells Based on Metal Salt Precursors,” *Sol. Energ. Mat. Sol. C.* **117**, 324–328 (2013).
- [103] A. Collord, H. Xin, and H. Hillhouse, “Combinatorial Exploration of the Effects of Intrinsic and Extrinsic Defects in Cu₂ZnSn(S,Se)₄,” *IEEE J. Photovolt.* **5**, 288–298 (2015).
- [104] A. Redinger, J. Sendler, R. Djemour, T. P. Weiss, G. Rey, P. J. Dale, and S. Siebentritt, “Different Bandgaps in Cu₂ZnSnSe₄; A High Temperature Co-evaporation Study,” *IEEE J. Photovolt.* (2014).
- [105] Y. S. Lee, T. Gershon, O. Gunawan, T. K. Todorov, T. Gokmen, Y. Virgus, and S. Guha, “Cu₂ZnSnSe₄ Thin-Film Solar Cells by Thermal Co-evaporation with 11.6% Efficiency and Improved Minority Carrier Diffusion Length,” *Adv. Energ. Mater* **5** (2015).

- [106] Q. Guo, G. M. Ford, W.-C. Yang, B. C. Walker, E. A. Stach, H. W. Hillhouse, and R. Agrawal, "Fabrication of 7.2% Efficient CZTSSe Solar Cells Using CZTS Nanocrystals," *J. Am. Chem. Soc.* **132**, 17384–17386 (2010).
- [107] G. Brammertz, M. Buffière, S. Oueslati, H. ElAnzeery, K. Ben Messaoud, S. Sahayaraj, C. Köble, M. Meuris, and J. Poortmans, "Characterization of Defects in 9.7% Efficient $\text{Cu}_2\text{ZnSnSe}_4$ -CdS-ZnO Solar Cells," *Appl. Phys. Lett.* **103**, 163904 (2013).
- [108] G. Zoppi, I. Forbes, R. W. Miles, P. J. Dale, J. J. Scragg, and L. M. Peter, " $\text{Cu}_2\text{ZnSnSe}_4$ Thin Film Solar Cells Produced by Selenisation of Magnetron Sputtered Precursors," *Prog. Photovoltaics* **17**, 315–319 (2009).
- [109] L. Grenet, S. Bernardi, D. Kohen, C. Lepoittevin, S. Noël, N. Karst, A. Brioude, S. Perraud, and H. Mariette, " $\text{Cu}_2\text{ZnSn}(\text{S}_{1-x}\text{Se}_x)_4$ Based Solar Cell Produced by Selenization of Vacuum Deposited Precursors," *Sol. Energ. Mat. Sol. C.* **101**, 11–14 (2012).
- [110] C. Gao, T. Schnabel, T. Abzieher, C. Krämmer, M. Powalla, H. Kalt, and M. Hetterich, " $\text{Cu}_2\text{ZnSn}(\text{S},\text{Se})_4$ Solar Cells Based on Chemical Bath Deposited Precursors," *Thin Solid Films* **562**, 621 – 624 (2014).
- [111] H. Helmers, C. Karcher, and A. W. Bett, "Bandgap Determination Based on Electrical Quantum Efficiency," *Appl. Phys. Lett.* **103**, 032108 (2013).
- [112] C. Huber, "Electroreflectance Spectroscopy of $\text{Cu}(\text{In},\text{Ga})\text{Se}_2$ and $\text{Cu}_2\text{ZnSn}(\text{S},\text{Se})_4$ in Thin-Film Solar Cells: Experiment and Simulation," Master's thesis, Karlsruhe Institute of Technology (2015).
- [113] C. Zimmermann, "Optical Spectroscopy on $\text{Cu}_2\text{ZnSn}(\text{S},\text{Se})_4$ Thin-Film Solar Cells," Master's thesis, Karlsruhe Institute of Technology (2015).
- [114] D. Sperber, "Optische Charakterisierung von CIGS- und Kesteritsolarzellen mittels Elektro- und Photoreflektanzmessungen," Master's thesis, Karlsruhe Institute of Technology (2013).
- [115] M. Lang, "Raman Spectroscopy of $\text{Cu}_2\text{ZnSnSe}_4$ Absorber Layers for Photovoltaics," Master's thesis, Karlsruhe Institute of Technology (2014).
- [116] E. Hecht, *Optik* (Oldenbourg, 2005).
- [117] C. F. Klingshirn, *Semiconductor Optics* (Springer Science & Business Media, 2012).

BIBLIOGRAPHY

- [118] B. O. Seraphin and N. Bottka, “Franz–Keldysh Effect of the Refractive Index in Semiconductors,” *Phys. Rev.* **139** (1965).
- [119] B. Seraphin and N. Bottka, “Band-Structure Analysis from Electro-Reflectance Studies,” *Phys. Rev. B* **145**, 628–636 (1966).
- [120] D. Aspnes, *Modulation Spectroscopy/Electric Field Effects on the Dielectric Function of Semiconductors*, vol. 2: Optical Properties of Semiconductors of *Handbook on Semiconductors* (North–Holland, 1980).
- [121] F. H. Pollak and H. Shen, “Modulation Spectroscopy of Semiconductors: Bulk/Thin Film, Microstructures, Surfaces/Interfaces and Devices,” *Mater. Sci. Eng. R-Rep.* **10**, 275–374 (1993).
- [122] D. E. Aspnes, P. Handler, and R. Island, “Interband Dielectric Properties of Solids in an Electric Field,” *Phys. Rev.* **166**, 921–933 (1968).
- [123] M. Abramowitz and I. A. Stegun, *Handbook of Mathematical Functions: with Formulas, Graphs, and Mathematical Tables*, 55 (Courier Corporation, 1964).
- [124] A. Batchelor, R. A., Brown, A. C., Hamnett, “Theoretical and Experimental Results for p-Type GaAs Electrolyte Electroreflectance,” *Phys. Rev. B* **41**, 1401–1412 (1990).
- [125] J. M. A. Gilman, A. Hamnett, and R. A. Batchelor, “Franz–Keldysh and Band-Filling Effects in the Electroreflectance of Highly Doped p-Type GaAs,” *Phys. Rev. B* **46**, 13363–13370 (1992).
- [126] D. Aspnes, “Band Nonparabolicities, Broadening, and Internal Field Distributions: The Spectroscopy of Franz–Keldysh Oscillations,” *Phys. Rev. B* **10**, 4428–4238 (1974).
- [127] T. J. C. Hosea, “Estimating Critical-Point Parameters from Kramers-Kronig Transformations of Modulated Reflectance Spectra,” *Phys. Status Solidi B* **182**, 43–47 (1994).
- [128] D. Johnson, “A Fourier Series Method for Numerical Kramers-Kronig Analysis,” *J. Phys. A Math. Gen.* **8**, 490 (1975).
- [129] U. Rau, D. Abou-Ras, and T. Kirchartz, eds., *Advanced Characterization Techniques for Thin Film Solar Cells* (John Wiley & Sons, 2011).
- [130] M. J. Romero, H. Du, G. Teeter, Y. Yan, and M. M. Al-Jassim, “Comparative Study of the Luminescence and Intrinsic Point Defects in the Kesterite $\text{Cu}_2\text{ZnSnS}_4$ and Chalcopyrite $\text{Cu}(\text{In,Ga})\text{Se}_2$ Thin Films Used in Photovoltaic Applications,” *Phys. Rev. B* **84**, 1–5 (2011).

- [131] P. Y. Yu and M. Cardona, *Fundamentals of Semiconductors* (Springer, 1999).
- [132] C. Huber, C. Krämmer, D. Sperber, A. Magin, H. Kalt, and M. Hetterich, “Electroreflectance of Thin-Film Solar Cells – Simulation and Experiment,” *Phys. Rev. B*, *accepted* (2015).
- [133] M. C. Tropicovsky, A. S. Sabau, A. R. Lupini, and Z. Zhang, “Transfer-Matrix Formalism for the Calculation of Optical Response in Multilayer Systems: From Coherent to Incoherent Interference,” *Opt. Express* **18**, 24715–24721 (2010).
- [134] J.A. Woollam Co., Inc., “WVASE32 - Refractive Index Materials Database,” (2010).
- [135] D. W. Lynch and W. Hunter, “Comments on the Optical Constants of Metals and an Introduction to the Data for Several Metals ,” in “Handbook of Optical Constants of Solids,” , E. D. Palik, ed. (Academic Press, Burlington, 1997), pp. 306 – 313.
- [136] D. J. Hall, T. J. C. Hosea, and D. Lancefield, “Airy Function Analysis of Franz–Keldysh Oscillations in the Photoreflectance Spectra of $\text{In}_{1-x}\text{Ga}_x\text{As}_y\text{P}_{1-y}$ Layers,” *J. Appl. Phys.* **82**, 3092–3099 (1997).
- [137] D. Bhattacharyya, R. Pal, S. Chaudhuri, and A. Pal, “Effective Electron Mass in Compound Semiconductor Films,” *Vacuum* **44**, 803 – 804 (1993).
- [138] M. Burgelman, P. Nollet, and S. Degraeve, “Modelling Polycrystalline Semiconductor Solar Cells,” *Thin Solid Films* **361–362**, 527 – 532 (2000).
- [139] D. Aspnes and A. Frova, “Influence of Spatially Dependent Perturbations on Modulated Reflectance and Absorption of Solids,” *Solid State Commun.* **88**, 1061–1065 (1993).
- [140] O. Gunawan, T. Gokmen, C. W. Warren, J. D. Cohen, T. K. Todorov, D. A. R. Barkhouse, S. Bag, J. Tang, B. Shin, and D. B. Mitzi, “Electronic Properties of the $\text{Cu}_2\text{ZnSn}(\text{Se},\text{S})_4$ Absorber Layer in Solar Cells as Revealed by Admittance Spectroscopy and Related Methods,” *Appl. Phys. Lett.* **100**, 253905 (2012).
- [141] P. Li, R. Anderson, and R. Plovnick, “Dielectric Constant of CuInSe_2 by Capacitance Measurements,” *J. Phys. Chem. Solids* **40**, 333 – 334 (1979).
- [142] A. Kindyak, V. Kindyak, and Y. Rud, “The Valence Band Structure in Chalcopyrite $\text{Cu}(\text{In},\text{Ga})\text{Se}_2$ Films,” *Semicond.* **31**, 882–885 (1997).

BIBLIOGRAPHY

- [143] S. Theodoropoulou, D. Papadimitriou, A. G. Mamalis, D. E. Manolagos, R. Klenk, and M.-C. Lux-Steiner, “Band-Gap Energies and Strain Effects in $\text{CuIn}_{1-x}\text{Ga}_x\text{S}_2$ Based Solar Cells,” *Semicond. Sci. Tech.* **22**, 933–940 (2007).
- [144] O. Kiowski, W. Witte, M. Hetterich, and M. Powalla, “Critical Points in the Band Structure of Absorber and Buffer Layers of $\text{CuIn}_{1-x}\text{Ga}_x\text{Se}_2$ Solar Cells by Electroreflectance Spectroscopy,” *IEEE J. Photovolt.* **4**, 285–290 (2014).
- [145] C. Krämmer, C. Huber, A. Redinger, D. Sperber, G. Rey, S. Siebentritt, H. Kalt, and M. Hetterich, “Diffuse Electroreflectance of Thin-Film Solar Cells: Suppression of Interference-Related Linshape Distortions,” *Appl. Phys. Lett.*, *manuscript in preparation* (2015).
- [146] T. Schnabel, T. Abzieher, T. M. Friedlmeier, and E. Ahlswede, “Solution-Based Preparation of $\text{Cu}_2\text{ZnSn}(\text{S},\text{Se})_4$ for Solar Cells—Comparison of SnSe_2 and Elemental Se as Chalcogen Source,” *IEEE J. Photovolt.* **5**, 670–675 (2015).
- [147] S. Adachi, “Model Dielectric Constants of GaP, GaAs, GaSb, InP, InAs, and InSb,” *Phys. Rev. B* **35**, 7454–7463 (1987).
- [148] J. T. Heath, J. D. Cohen, and W. N. Shafarman, “Bulk and Metastable Defects in $\text{CuIn}_{1-x}\text{Ga}_x\text{Se}_2$ Thin Films Using Drive-Level Capacitance Profiling,” *J. Appl. Phys.* **95**, 1000–1010 (2004).
- [149] J. Mattheis, U. Rau, and J. H. Werner, “Light Absorption and Emission in Semiconductors with Band Gap Fluctuations—A study on $\text{Cu}(\text{In},\text{Ga})\text{Se}_2$ Thin Films,” *J. Appl. Phys.* **101**, 113519 (2007).
- [150] T. Gokmen, O. Gunawan, and D. B. Mitzi, “Semi-Empirical Device Model for $\text{Cu}_2\text{ZnSn}(\text{S},\text{Se})_4$ Solar Cells,” *Appl. Phys. Lett.* **105**, 033903 (2014).
- [151] C. Krämmer, C. Huber, C. Zimmermann, M. Lang, T. Schnabel, T. Abzieher, E. Ahlswede, H. Kalt, and M. Hetterich, “Reversible Order-Disorder Related Band Gap Changes in $\text{Cu}_2\text{ZnSn}(\text{S},\text{Se})_4$ via Post-Annealing of Solar Cells Measured by Electroreflectance,” *Appl. Phys. Lett.* **105**, 262104 (2014).
- [152] C. Zimmermann, C. Krämmer, M. Lang, C. Huber, H. Kalt, and M. Hetterich, “State-Filling versus Screening of Electrostatic Potential Fluctuations in $\text{Cu}_2\text{ZnSn}(\text{S},\text{Se})_4$ Solar Cells,” *Appl. Phys. Lett.*, *manuscript in preparation* (2015).
- [153] J. Tauc, “Optical Properties and Electronic Structure of Amorphous Ge and Si,” *Mater. Res. Bull.* **3**, 37 – 46 (1968).

- [154] V. P. Dobrego and I. S. Shlimak, “The Influence of Local Potential Fluctuations on the Low-Temperature Radiative Recombination of Compensated Germanium,” *Phys. Status Solidi B* **33**, 805–809 (1969).
- [155] P. W. Yu, “Excitation-Dependent Emission in Mg-, Be-, Cd-, and Zn-Implanted GaAs,” *J. Appl. Phys.* **48**, 5043–5051 (1977).
- [156] P. W. Yu, C. E. Stutz, M. O. Manasreh, R. Kaspi, and M. A. Capano, “Moving Photoluminescence Bands in $\text{GaAs}_{1-x}\text{Sb}_x$ Layers Grown by Molecular Beam Epitaxy on InP Substrates,” *J. Appl. Phys.* **76**, 504–508 (1994).
- [157] E. O. Kane, “Band Tails in Semiconductors,” *Solid State Electron.* **28**, 3 – 10 (1985).
- [158] T. Gershon, B. Shin, N. Bojarczuk, T. Gokmen, S. Lu, and S. Guha, “Photoluminescence Characterization of a High-Efficiency $\text{Cu}_2\text{ZnSnS}_4$ Device,” *J. Appl. Phys.* **114**, 154905 (2013).
- [159] J. Shay, B. Tell, H. Kasper, and L. Schiavone, “Electronic Structure of AgInSe_2 and CuInSe_2 ,” *Phys. Rev. B* **7**, 4485–4490 (1973).
- [160] C. Rincón, E. Hernández, S. Wasim, and I. Molina, “Temperature Dependence of the Fundamental Absorption Edge in p-Type CuInSe_2 ,” *J. Phys. Chem. Solids* **59**, 1015 – 1019 (1998).
- [161] T. M. Hsu and J. H. Lin, “Anomalous Temperature-Dependent Band Gaps in CuInS_2 Studied by Surface-Barrier Electroreflectance,” *Phys. Rev. B* **37**, 4106–4110 (1988).
- [162] P. W. Yu, W. Anderson, and Y. Park, “Anomalous Temperature Dependence of the Energy Gap of AgGaS_2 ,” *Solid State Commun.* **13**, 1883 – 1887 (1973).
- [163] L. Artus and Y. Bertrand, “Anomalous Temperature Dependence of Fundamental Gap of AgGaS_2 and AgGaSe_2 Chalcopyrite Compounds,” *Solid State Commun.* **61**, 733 – 736 (1987).
- [164] J. J. Scragg, T. Kubart, J. T. Wätjen, T. Ericson, M. K. Linnarsson, and C. Platzer-Björkman, “Effects of Back Contact Instability on $\text{Cu}_2\text{ZnSnS}_4$ Devices and Processes,” *Chem. Mater.* **25**, 3162–3171 (2013).
- [165] P. K. Sarswat and M. L. Free, “A Study of Energy Band Gap Versus Temperature for $\text{Cu}_2\text{ZnSnS}_4$ Thin Films,” *Physica B* **407**, 108–111 (2012).

BIBLIOGRAPHY

- [166] J. Krustok, H. Collan, M. Yakushev, and K. Hjelt, “The Role of Spatial Potential Fluctuations in the Shape of the PL Bands of Multinary Semiconductor Compounds,” *Phys. Scripta* **1999**, 179–182 (1999).
- [167] T. Schmidt, K. Lischka, and W. Zulehner, “Excitation-Power Dependence of the Near-Band-Edge Photoluminescence of Semiconductors,” *Phys. Rev. B* **45**, 8989–8994 (1992).
- [168] F. Urbach, “The Long-Wavelength Edge of Photographic Sensitivity and of the Electronic Absorption of Solids,” *Phys. Rev.* **92**, 1324–1324 (1953).
- [169] B. Shklovskii and A. Efros, “Springer series in solid-state sciences,” in “Electronic Properties of Doped Semiconductors,” (Springer-Verlag Berlin, 1984), p. 45.
- [170] I. Dirnstorfer, M. Wagner, D. Hofmann, M. Lampert, F. Karg, and B. Meyer, “CuIn(Ga)Se₂ Solar Cells: Characterization of the Absorber Material,” in “Conference Series-Institute of Physics,” , vol. 152 (IOP PUBLISHING LTD, 1998), vol. 152, pp. 233–236.
- [171] J. J. S. Scragg, L. Choubrac, A. Lafond, T. Ericson, and C. Platzer-Björkman, “A Low-Temperature Order–Disorder Transition in Cu₂ZnSnS₄ Thin Films,” *Appl. Phys. Lett.* **104**, 041911 (2014).
- [172] T. Washio, H. Nozaki, T. Fukano, T. Motohiro, K. Jimbo, and H. Katagiri, “Analysis of Lattice Site Occupancy in Kesterite Structure of Cu₂ZnSnS₄ Films Using Synchrotron Radiation X-Ray Diffraction,” *J. Appl. Phys.* **110**, 074511 (2011).
- [173] T. Toyama, T. Konishi, Y. Seo, R. Tsuji, K. Terai, and Y. Nakashima, “Annealing-Induced Optical-Bandgap Widening of Cu₂ZnSnS₄ Thin Films with Observation of Simultaneous Increase in Local-Structure Ordering,” *Jpn. J. Appl. Phys.* **54**, 015503 (2015).
- [174] G. Rey, A. Redinger, J. Sandler, T. P. Weiss, M. Thevenin, M. Guennou, B. El Adib, and S. Siebentritt, “The Band Gap of Cu₂ZnSnSe₄: Effect of Order–Disorder,” *Appl. Phys. Lett.* **105**, 112106 (2014).
- [175] M. Paris, L. Choubrac, A. Lafond, C. Guillot-Deudon, and S. Jobic, “Solid-State NMR and Raman Spectroscopy to Address the Local Structure of Defects and the Tricky Issue of the Cu/Zn Disorder in Cu-Poor, Zn-Rich CZTS Materials,” *Inorg. Chem.* **53**, 8646–8653 (2014). PMID: 25069473.

- [176] C. Krämmer, C. Huber, T. Schnabel, C. Zimmermann, M. Lang, E. Ahlswede, H. Kalt, and M. Hetterich, “Order–Disorder Related Band Gap Changes in $\text{Cu}_2\text{ZnSn}(\text{S},\text{Se})_4$: Impact on Solar Cell Performance,” in “Photovoltaic Specialist Conference (PVSC), 2015 IEEE 42th,” (IEEE, 2015).
- [177] A. Redinger, M. Mousel, M. H. Wolter, N. Valle, and S. Siebentritt, “Influence of S/Se Ratio on Series Resistance and on Dominant Recombination Pathway in $\text{Cu}_2\text{ZnSn}(\text{S},\text{Se})_4$ Thin Film Solar Cells,” *Thin Solid Films* **535**, 291–295 (2013).
- [178] D. A. R. Barkhouse, O. Gunawan, T. Gokmen, T. K. Todorov, and D. B. Mitzi, “Device Characteristics of a 10.1% Hydrazine-Processed $\text{Cu}_2\text{ZnSn}(\text{Se},\text{S})_4$ Solar Cell,” *Prog. Photovoltaics* **20**, 6–11 (2012).
- [179] G. H. Vineyard, “Theory of Order-Disorder Kinetics,” *Phys. Rev.* **102**, 981–992 (1956).
- [180] B. E. Warren, *X-ray Diffraction*, Dover books on physics (Dover, New York, 1990).
- [181] H. Katagiri, K. Jimbo, M. Tahara, H. Araki, and K. Oishi, “The Influence of the Composition Ratio on CZTS-Based Thin Film Solar Cells,” in “MRS Proceedings,” , vol. 1165 (Cambridge Univ Press, 2009), vol. 1165, pp. 1165–M04.
- [182] T. Gershon, T. Gokmen, O. Gunawan, R. Haight, S. Guha, and B. Shin, “Understanding the Relationship Between $\text{Cu}_2\text{ZnSn}(\text{S},\text{Se})_4$ Material Properties and Device Performance,” *MRS Communications* **4**, 159–170 (2014).
- [183] T. Musiol, “Investigations Into the Selenisation Process of Precursors for CZT(S,Se) Thin-Film Solar Cells,” Master’s thesis, Karlsruhe Institute of Technology (2015).

Closing Words

Finally, I would like to thank all the people who have supported me in the pursuit of this work:

- Prof. Dr. Heinz Kalt and Priv-Doz. Dr. Michael Hetterich for giving me the possibility to work on this interesting topic, their support throughout this work, many valuable discussions – and for giving me the freedom to form this project the way I wanted to.
- My friends and colleagues Andreas Merz, Tobias Siegle, and Mario Lang, whom I have always enjoyed working with and with whom I shared a great time in our group. It was a privilege to work with you, you are the best!
- All my bachelor, master and diploma students who participated actively in all aspects of thin-film photovoltaics research and who made our group a place at which I always enjoyed working.
- Of all my students, I would like to highlight Christian Huber and Christian Zimmermann with whom I had the pleasure to work together very closely and also spend time outside university. As a team, we achieved extraordinary results and shared valuable discussions which led to a giant leap forward of the kesterite project.
- All members of our workgroup for the friendly atmosphere.
- Alexander Hepting for instantaneous, competent, and uncomplicated help in all concerns of an optical lab.
- The electronics and mechanics workshop for their competent support in the conception and realization of the optical lab and the individual setups.
- Our secretaries for help and support in all kinds of administrative concerns.

- Dr. Thomas Schnabel, Tobias Abzieher, Manuel Löw, and Dr. Erik Ahlswede for a reliable supply of samples but more importantly – a friendly atmosphere in our cooperation.
- Prof. Dr. Susanne Siebentritt and Dr. Alex Redinger for an uncomplicated collaboration even without a common project and for fruitful discussions on kesterites.
- Dr. Jonathan Scragg for providing the CZTS sample and a very nice discussion about band edge fluctuations.
- All people who read this thesis and helped to eliminate all kinds of errors...
- My family and my parents who have been supporting me for all my life. Without you, this would not have been possible.
- My grandfather who taught me the patience which was necessary for this work.
- My wife Sarah for her belief in me, her everlasting support and love. I love you.